PHYSICA MACEDONICA

Institute of Physics
Faculty of Natural Sciences and Mathematics
Sts. Cyril and Methodius University,
Skopje, Macedonia

PHYSICA MACEDONICA

A JOURNAL OF EXPERIMENTAL AND THEORETICAL PHYSICS

NOVEL STATES IN QUANTUM MATTER

G. Zwicknagl

*Institut f. Mathematische Physik, Technische Universität Braunschweig,
Mendelssohnstr. 3, 38106 Braunschweig, Germany*

Abstract. Understanding the collective electronic properties of emergent materials remains a great challenge to condensed-matter theory. The quantum mechanical ground states are determined by subtle compromises between varoius interactions. The resulting high sensitivity with respect to external fields will allow for new functionalities and novel technical applications. The present paper discusses typical emergent phenomena including the formation of heavy fermions in Kondo lattices, quantum phase transitions and quantum criticality as well as orbital-selective localization transitions.

PACS: 71.10.-w, 71.27.+a, 75.30.Mb, 73.43.Nq

1. INTRODUCTION

Quantum materials are a topic at the forefront of research in condensed matter physics. Important examples are transition metal oxides, metals containing lanthanide or actinide atoms and organic conductors. At low temperatures, these materials exhibit novel phenomena like metal-to-insulator transitions, heavy fermions, unconventional superconductivity and unusual magnetism. As the properties of quantum materials are highly sensitive with respect to changes in external parameters like pressure, magnetic and electric fields they are important candidates for technological applications. The electronic properties of these materials, however, are very difficult to predict despite complete knowledge of the underlying interactions.

The electronic structure problem for a solid is one of many interacting fermions (electrons) moving in a lattice. The properties of these systems are generally determined by the interplay of two types of influences as schematically summarized in Fig. 1. First, there is a tendency towards delocalization which is a consequence of the fact that wave functions at neighboring lattice sites overlap. It favors the formation of a conventional band spectrum and one-electron Bloch states in which the itinerant electrons are distributed throughout the entire crystal. On the other hand, the electrons interact via the Coulomb interaction which leads to localization. The Coulomb repulsion necessarily restricts the hopping of an electron from one site to another. The reason is that a second electron feels a strong repulsion at a given atomic site when another electron is already present. As a consequence, the hopping probability will depend on whether the final site is occupied or empty and therefore introduce correlations.

A strong Coulomb interaction between two electrons at the same lattice site would favor the formation of local magnetic moments which can be observed in the magnetic susceptibility. Interacting electrons in a lattice experience both trends and the relative importance of both determines the electronic properties of a given material (for textbooks see e.g.[1, 2]).

The general theoretical problem has proved too difficult for an exact analysis. Approximate solutions can be found only in limiting cases.
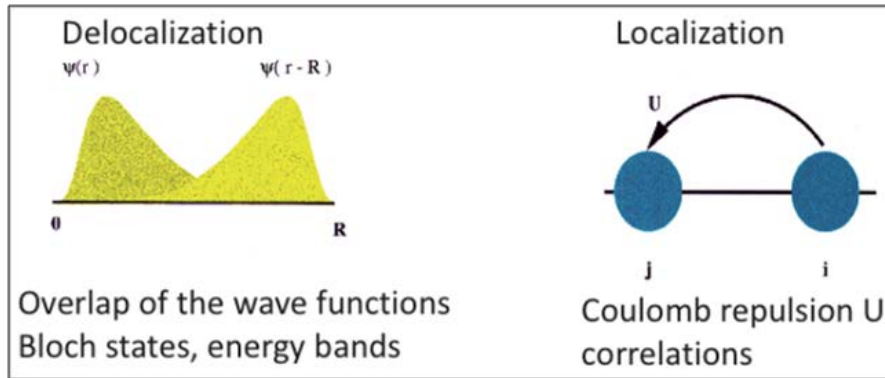

Fig. 1: Electrons in a crystal experience both a trend towards delocalization through the formation of extended Bloch states and a trend towards localization resulting from the local Coulomb repulsion.

2. HISTORIC REVIEW

The traditional electron theory of metals which is based on the Sommerfeld-Bethe model [3] emphasizes the aspect of delocalization. Starting from the picture of free electrons the model successfully describes a great variety of metallic properties. The ground state of the non-interacting spin1/2 fermions is obtained by successively filling the single-particle states with the lowest energies in accordance with the Pauli principle. The characteristic feature is the Fermi surface in momentum space separating occupied and empty states. The chemical potantial defines the characteristic energy, the Fermi energy E_F which is of the order of 10 eV in metals. The low-energy excitations are particle-hole excitations where electrons are promoted across the Fermi surface. For low temperatures the model predicts a linear variation with temperature of the electronic contribution to the specific heat $C \approx \gamma T + \dots$ with a proportionality factor γ of order $1 mJ/moleK^2$ and a temperature independent magnetic susceptibility reflecting the non-magnetic character of the ground state. The success of this theory which completely neglects electron-electron interactions is at first glance rather surprising since one knows that the Coulomb interaction between the electrons must produce correlations.

The "free" electron picture was justified by Landau in his famous theory of Fermi liquids [4] which provides a highly useful conceptual framework for describing interacting fermi systems. The fundamental conceptual basis is the notion of "adiabatic continuity" which should prevail if the interaction is gradually turned on [5]. As states of simular symmetry do not cross during this adiabatic process there should result a one-to-one

correspondence between the well-known free fermion states and their unknown complex counterparts in the interacting system. In particular, the character of the ground states are the same, i. e., filled Fermi seas. The low-energy excitations can be described to good approximation in terms of a single-particle spectrum. This important fact is a direct consequence of the Pauli principle. The single-particle excitations or "quasi-particles" are characterized by momentum and spin and obey Fermi statistics. They can be visualized as composite objects consisting of the bare particle (electron) and some kind of polarization cloud which results from the Coulomb correlations. The many-body effects modify the energy dispersion relation and the interactions of the quasi-particles. The one-to-one correspondence implies in general that the interactions do not change the volume enclosed by the Fermi surface. This statement is commonly referred to as Luttinger's theorem [6]. Today, Landau's Fermi liquid theory is the "standard model" for the modern electron theory of metals.

Density Functional Theory (DFT) introduced by Hohenberg, Kohn and Sham [7, 8] provides an efficient and rather accurate method to explicitly construct effective potentials required for material specific calculations. The fundamental quantity of the theory is the (inhomogeneous) electron density in the ground state which is to be determined selfconsistently. Working with densities which depend on a single spatial variable instead of the full many-body wave function of an N particle system results in a tremendous simplification which makes electronic structure calculations possible for rather complex materials. The theory allows for parameter-free calculations of the ground state properties [9]. The method yields ficticious energy eigenvalues which are usually very good approximations to the physical energy levels. For a review see [10].

The quasiparticles successfully describe the low-energy excitations of metals in their normal state. David Bohm and David Pines [11] realized that in interactions can lead to collective oscillations of the electron gas, the plasmons.

The break-down of the Landau Fermi liquid theory at the transition from the normal into the superfluid or superconducting state can be described by introducing the concept of broken symmetry[12]. According to this ansatz, phase transitions occur via symmetry reduction which is described in terms of an order parameter. The latter characterizes the appearance of long-range correlations - the pair-correlations in superconductors. Similar examples are the formation of a Charge Density Wave (CDW) or a Spin Density Wave (SDW).

The framework described above consistently and successfuly describes the behavior of "ordinary" metals. In the spirit of Landau, the starting point is the picture of non-interacting electrons moving in effective potentials which also account for electron-electron interaction effects. The DFT provides a highly sophisticated scheme for explicitly constructing the effective potentials. The electron states provide the basis for understanding the collective dynamics which affects the response to external perturbations and phase transitions where long-range correlations are accounted for by symmetry-breaking.

3. STRONG LOCAL CORRELATIONS

The framework as described in the preceding section was seriously challenged by an unexpected series of discoveries starting from 1976. Important examples are the Heavy Fermion (HF) superconductivity in lanthanide and actinide compounds, the Fractional Quantum Hall Effect (FQHE), superconductivity in cuprates, colossal magnetoresistence, Quantum Criticality (see e. g. [1] and references therein). The materials have in common that their low-energy properties are determined by strong interactions among the electrons. The interactions, however, cannot be accounted for by effective potentials as in DFT nor by considering collective excitations or by symmetry breaking. The consequences of electron interactions which cannot be captured by the standard framework are termed "correlation effects". Electron correlations lead to novel, often highly complex ground states and anomalies in numerous observables.

Electron correlations are strongly evident in the cuprate superconductors which may have transition temperatures ranging up to 100K. The superconducting systems are obtained by doping a small number of electrons or holes into a parent compound whose insulating state is a direct consequence of electron correlations. The key is the number of valence electrons in the unit cell. The independent electron picture for the ground state has the following implication for periodic crystals: For N electrons, we have to fill the N/2 lowest lying band states with two electrons. We immediately see that with an odd number of (valence) electrons in the unit cell, there must be a partially filled band. As a consequence, band theory predicts materials with an odd number of (valence) electrons per unit cell to be metallic.
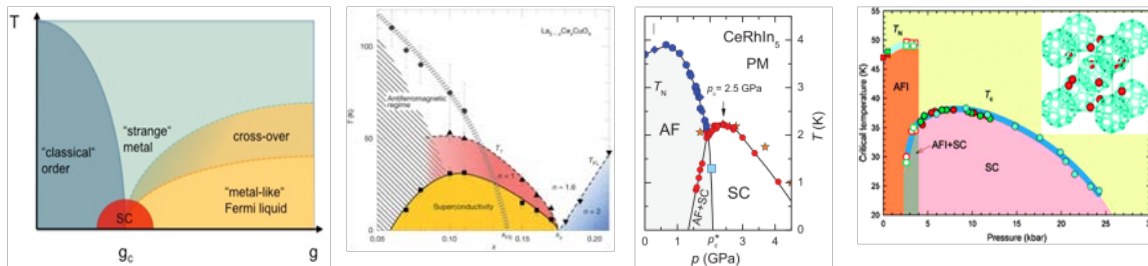

Fig. 2: Generic phase diagram of materials with strongly correlated electrons From left to right: Schematic phase diagram denoting the various low-temperature phases. Experimental phase diagrams of the cuprate superconductor $La_{2-x}Ce_xCuO_4$, the heavy fermion system $CeRhIn_5$, and the doped fulleride Cs_3C_{60} (from [35]).

This very general rule derived from independent electron band theory fails e. g. in the undoped parent material La_2CuO_4 of the cuprate superconductor $La_{2-x}Sr_xCuO_4$. Although there is an odd number of electrons in the unit cell containing two La-, four O- and one Cu-atom in $3d^9 4s^2$ configuration the material is an insulator. The counting argument refers to the chemical unit cell. Breaking translational symmetry by a (magnetic) superstructure can lead to a (magnetic) supercell with an even number of electrons. This, however, can be ruled out for the antiferromagnet La_2CuO_4 which remains an insulator also in the translational invariant state above the Néel temperature. We therefore conclude that the insulating ground state of La_2CuO_4 is a consequence of the strong electron-electron interactions. The correlation-driven metal-to-

insulator transition is called Mott transition, materials like La_2CuO_4 are called Mott insulators[13, 14].

The failure of independent electron theory in the case of Mott insulators highlights the necessity to incorporate electron correlations into electronic structure calculations. This can be achieved technically by the LDA+U method where the Coulomb repulsion U is introduced in an ad-hoc fashion. A more sophisticated treatment of strong local correlations is provided by the Dynamical Mean Field Theory (DMFT) [15, 16].

The Mott insulating state, however, has an extremely high degeneracy resulting from the spins of the localized electrons. This degeneracy is usually lifted by forming "classical" long-range magnetic order. Reducing the distance between the lattice sites by application of pressure leads to an increase in the energy due to delocalization. Many Mott systems can hence be driven through a an insulator-to-metal transition to a metallic phase by changes in a non-thermal parameter like pressure, composition etc. Fig. 2 displays the generic phase diagram which schematically describes the behavior of a wide variety of strongly correlated fermion systems including transition metal oxides, organic conductors, and heavy fermion materials.

4. HEAVY FERMIONS IN KONDO LATTICES

In emergent materials, the correlation effects, i. e., the deviations from the anticipated behavior of independent electrons result from partially filled inner d- or f-shells. From a theorist's point of view, these materials lie at the intersection of a large number of long-standing problems in the physics of metals. We immediately face the fundamental question which picture provides the better starting point for theoretical models, a delocalized description in terms of energy bands or a localized representation which properly accounts for the atomic properties. This question turns out to be ill-posed in the case of lanthanide-based heavy fermion compounds where the character of the 4f electrons seems to change with temperature, pressure and magnetic field. Some of the best known examples are the Ce-based compounds $CeCu_2Si_2$, $CeRu_2Si_2$, $CeTIn_5$ with T=Co, Rh, Ir as well as the Yb-systems $YbRh_2Si_2$ and $YbIr_2Si_2$. For recent reviews see e. g. [17–19] and references therein.

The 4f electrons are rather well localized, the corresponding charges are more or less confined within spheres of the ionic radii. As a consequence, the f states are expected to preserve their atomic character. The strong Coulomb interaction at each atomic site is rather strong and can lead to a variety of magnetic effects. The novel phenomena we encounter in these systems is the appearance of a new energy scale $k_B T^* \approx 1 meV$ which result from the strong correlations within the f-shells. As a consequence of the strong correlations, it is not possible to describe the influence of the f-states in terms of a unique simple model. In the high-temperature regime, the degrees of freedom associated with the partially filled f-shells are conveniently modelled by local magnetic moments which weakly interact with the conduction electrons. The f-electrons can be considered as part of the ion cores in viewing the band structures of heavy fermion compounds. The number of quasiparticles which determines the volume enclosed by the Fermi surface is given by the number of conduction electrons and, concomittantly, equals the nominal

chemical valence. The Fermi surface is "small". At low temperatures, the local spin-degrees of freedom at the f-sites are strongly coupled to the conduction electrons forming (local) singlets with them. The specific heat varies approximately linearly with temperature (that is, $C \approx \gamma T + \dots$), and the magnetic susceptibilty, χ, approaches a Pauli-like form, becoming almost independent of temperature. The values of the coefficients are of the order of $1J/moleK^2$ and consequently several order of magnitude larger than those of ordinary metals which are of the order of $1mJ/moleK^2$. Due to the large Sommerfeld coefficient of the electronic specific heat which can be written in terms of an effective mass m^* of the quasiparticles these materials have been termed heavy fermion compounds. The magnetic susceptibility χ, is enhanced by a factor of comparable magnitude. These findings suggest that Heavy Fermions compounds form Fermi liquids at sufficiently low temperatures. Many well-known relations derived for independent electrons are satisfied provided the huge effective mass of the quasiparticles is properly accounted for. This is achieved by replacing the Fermi energy E_F which is typically of order 10 eV in a conventional metal by the characteristic temperature T^* which is of order 1meV. The central assumption is that the low-energy excitations reflected in the low-temperature properties are long-lived fermionic quasiparticles with predominantly f-character. The f-degrees of freedom are modelled by itinerant "heavy" quasiparticles which form narrow bands in the vicinity of the Fermi surface. The number of quasiparticles which determines the volume of the Fermi surface includes the f-states, the Fermi surface is "large". Comparing the high and the low temperature regime we see that the f-degrees of freedom seem to change their character which is a consequence of the strong correlations[20]. The latter lead to a clear deviation from Luttinger's theorem according to which the volume enclosed by the Fermi surface should not change.

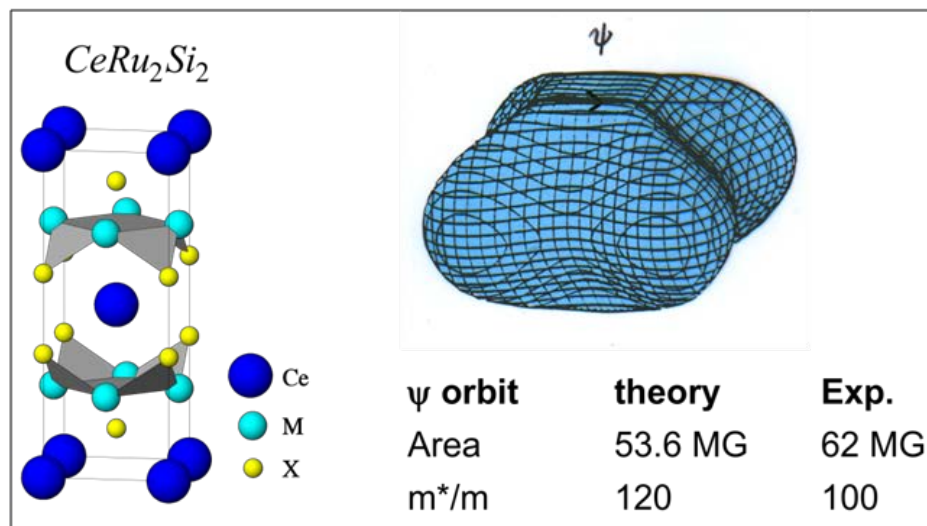**Fig. 3:** Heavy quasiparticles in CeRu$_2$Si$_2$: Comparison of theory [21] and experiment [22]. The heavy quasiparticles explain the high specific heat ar low temperatures, i. e., they exhaust the low-energy excitations.

The hypothesis has been convincingly corroborated by experiment[21] as can be seen from Fig. 3. The theoretically predicted quasiparticle dispersions both for the high temperature

state with localized f-states with a "small" Fermi surface as well as for the itinerant f-derived heavy quasiparticles with their "large" Fermi surface were confirmed by deHaas-vanAlphen [22]and Angle Resolved Photo Electron Spectroscopy(ARPES)[23]. The calculations adopted the Renormalized Band (RB) method which is a concept for a theoretical description of the Fermi liquid state. It merges ab-initio-band structure calculations and phenomenological considerations in the spirit of Landau [24] . The central idea is to account for the correlations by introducing a small number of phenomenological parameters which are determined by fitting to appropriate experiments. For heavy fermion systems it is sufficient to adjust a single parameter - the averaged effective mass of the quasiparticles – to obtain a detailed description of the energy dispersion for a dilute gas of quasiparticles.
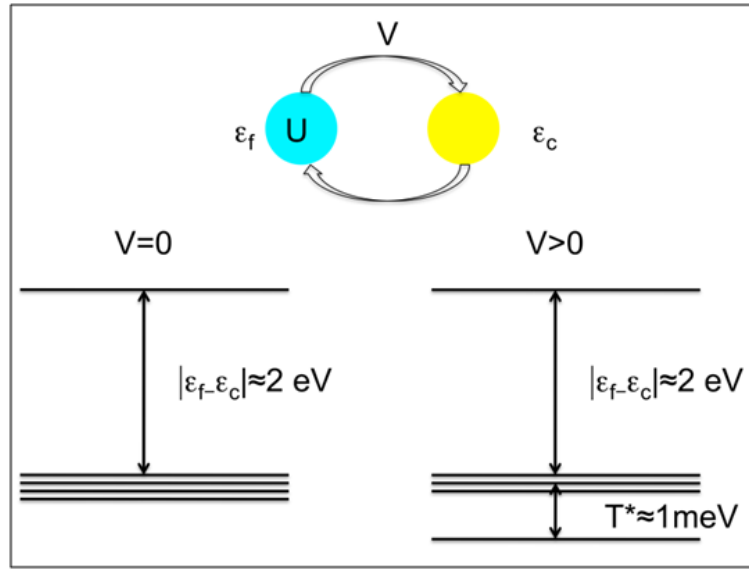

Fig. 4: Simple Molecular Model and eigenvalues of the corresponding two-electron problem for $\left(\varepsilon_f < \varepsilon_c\right(<< \left(V\right($ in the limit of strong Coulomb repulsion $U \to \infty$. Due to the strong Coulomb repulsion among the f-electrons, the energetically most favorable states are obtained by occupying one f-state and one ligand state. This results in a fourfold degenerate ground state for vanishing hybridization. The spin degeneracy is lifted by hybridization with the doubly occulpied ligand orbital. The low-energy singlet state is lowered relative to the triplet state by a small amount of energy $k_B T^*$.

The similarities in the behavior of Ce- and Yb-based heavy-fermion systems to that of dilute magnetic alloys have led to the assumption that these systems are "Kondo lattices" where the observed anomalous behavior can be explained in terms of periodically repeated resonant Kondo scattering[25]. The Kondo effect leads to a characteristic minimum in the variation with temperature of the electrical resistance of dilute magnetic alloys whose position does not depend on the impurity concentration. The unexpected rise of resistance at low temperatures highlights the condensed-matter analogue of quark confinement. Like the quarks, the local momemnts in a metallic host are asymptotically free at high temperatures/energies while at low temperatures/energies, they form compound quasiparticles with the conduction electrons, they become confined. The Kondo lattice model provides a microscopic explanation for the formation of a singlet groundstate and the existence of heavy quasiparticles[26]. In addition, it

explains why there is no magnetic pairbreaking associated with the presence of the f-electrons. The Kondo picture for the Ce- and Yb-based heavy-fermion compounds is supported by photoelectron and tunneling spectroscopy [23, 27].

The characteristic temperature T^* which is much smaller than typical electronic energies associated with single-particle excitations in ordinary metals as well as the non-magnetic ground state each result from many-body effects which are absent in a homogeneous electron gas. The essential physics of heavy fermion systems is already contained in the Molecular Model [28, 29] displayed in Fig. 4 where the weakly correlated conduction states of the metal are replaced by a two-fold degenerate extended ligand state such as an s-orbital. The Coulomb repulsion in this extended orbital is rather weak and can be neglected. The strong correlations are introduced by localized f-states with orbital energy $\varepsilon_f < \varepsilon_c$ which strongly repel one another. We consider only the spin degeneracy neglecting the orbital degrees of freedom. These two subsystems are coupled through a weak hybridization V. For our qualitative considerations we shall assume $U \rightarrow \infty$ and consider only states where the f-orbital is empty (f^0-configuration) and where it is singly occupied (f^1-configuration).

Let us consider the two-electron states of the model displayed in Figure 3. In the absence of hybridization (V = 0) the ground state with $E = \varepsilon_f$ is fourfold degenerate which is a direct consequence of the fact that the strong Coulomb repulsion among the f-electrons makes the f^2- configuration energetically unfavorable. The degeneracy is lifted by the weak hybridization between the ligand and the f-states. To leading order in the small ratio $V^2 / (\varepsilon_f ($ the singlet state is lowered in energy by an amount $k_B = 2V^2 / (\varepsilon_f ($ which, in turn, characterizes the low-energy excitations. For the parameter range considered here the f-valence n_f is close to unity, $n_f = 1 - V^2 / (\varepsilon_f (^2$

5. INSTABILITIES OF THE HEAVY FERMI LIQUID

Going back to the generic phase diagram Fig. 2, a natural question is to ask how does the magnetically ordered ground state at small values of the tuning parameter emerge from the Fermi liquid state realized at large values at T=0? The consequences of such zero temperature phase transitions represent a major unsolved challenge to our understanding of correlated matter. Although a Quantum Critical Point (QCP) strictly exists only at T=0, it can have observable consequences at elevated temperatures through quantum critical fluctuations. A prominent example is the quasi-linear variation with temperature close to quantum criticality where we encounter "strange metals". Considering the transition, there are two possible scenarios (a) a symmetrybroken state carrying a SDW can form out of the Fermi liquid state or, alternatively, (b) the Fermi liquid state can collapse at the same critical value gc where also the magnetic order disappears (see e. g. [30, 31])

It could be demonstrated the the transition to the A phase in CeCu$_2$Si$_2$ occurs through a SDW transition as explained in Fig. 5. At low magnetic fields, there is a QCP of type (b) in YbRh$_2$Si$_2$.
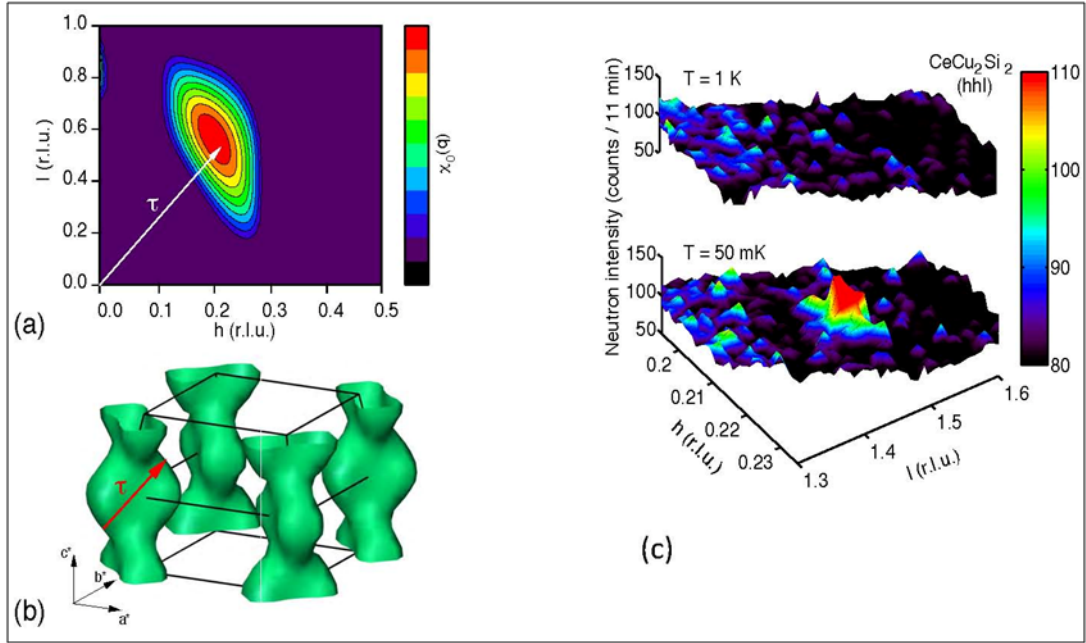
Fig. 5: Left panel: Nesting on Fermi surface of heavy quasiparticles leads to a peak in the static suceptibility at finite wave vector Q as shown by the intensity map (value increasing from dark to bright) in the reciprocal (h,h,l)- plane as calculated for the Renormalized Bands at T = 100 mK. The experimental Q at 50 mK from the right panel shows perfect agreement with the calculated maximum position. Neutron diffraction intensity in $CeCu_2Si_2$ at temperature above and below the A- phase transition temperature T_A.

6. 3=2+1: DUAL NATURE OF 5F ELECTRONS

The strongly correlated 5f electrons in actinide compounds may undergo a partial, i. e., orbital-5f moments coexist with itinerant 5f band electrons. The 5f-electrons have "dual" nature[32]. Initially, the dual character has been conjectured for UPd_2Al_3 where the variation with temperature of the magnetic susceptibility points to the existence of CEF-split localized 5f states in a heavy fermion system with 5f-derived itinerant quasiparticles. Concerning the low-energy excitations it has been shown that the dual model allows for a quantitative description of the renormalized quasiparticles - the heavy fermions - in UPd_2Al_3 and UPt_3. The results for UPd_2Al_3 are summarized in Fig. 6. There is clear evidence that the presence of localized 5f states is even responsible for the attractive interaction leading to superconductivity. For a recent review of experimental facts see [17].

Before turning to a discussion of the dual model, its results and their implications we should like to add a few comments. In referring to the dual model one has to keep in mind that the latter provides an effective Hamiltonian designed exclusively for the low-energy dynamics. As such it seems appropriate for typical excitation energies below ~10 meV. In general, effective low-energy models are derived form the underlying microscopic Hamiltonians - to

borrow the language of Wilson's renormalization group - by integrating out processes at higher energies.selective localization .

The dual model conjectures that the complicated excitations of the strongly correlated 5f electron system can be approximately decomposed in the low-energy regime into coherent dispersive quasiparticle bands and incoherent local excitations. Model calculations based on Exact Diagonalization (ED) for small clusters as well as mean-field studies for infinite periodic lattices show that intra-atomic correlations as described by Hund's rules may strongly enhance anisotropies in the effective band widths and thus lead to an orbital-selective Mott transition in 5f-systems[33].

The correlation-induced orbital-selective Mott transition leads to a novel state of matter where localized atomic-like 5f electrons coexist with itinerant 5f band electrons.
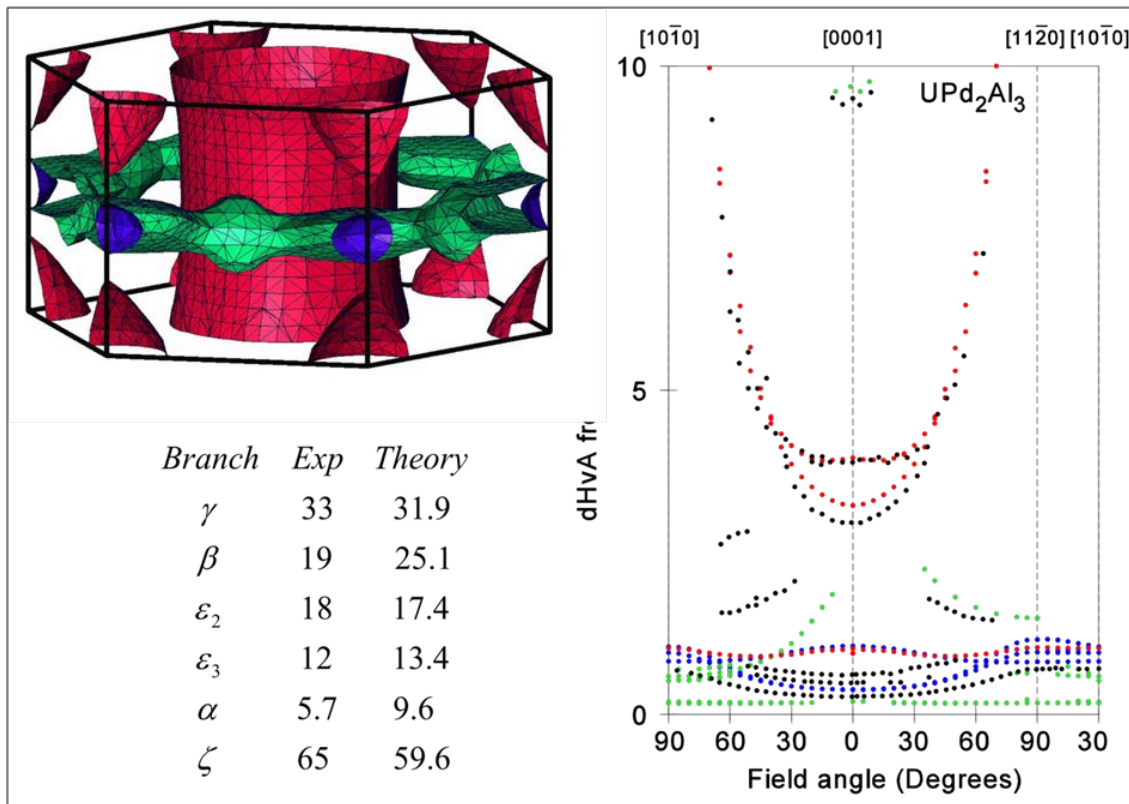

Branch	Exp	Theory
γ	33	31.9
β	19	25.1
ε_2	18	17.4
ε_3	12	13.4
α	5.7	9.6
ζ	65	59.6

Fig. 6: Heavy quasiparticles in the heavy fermion compound UPd_2Al_3. The Fermi surface predicted by the Dual Model correctly reproduces the deHaas-vanAlphen data and provides a parameter-free explanation of the heavy masses (see [33,34]).

7. SUMMARY AND OUTLOOK

A remarkable variety of collective electronic phenomena have been discovered in quantum materials with strongly interacting electrons. Their high sensitivity with respect to changes in external parameters like pressure, electric and magnetic fields is considered as a resource which might eventually provide new functionalities. A comprehensive microscopic

understanding of the novel states with their intriguingly complex behavior remains a major challenge for theoretical condensed-matter physics.

REFERENCES

[1] Peter Fulde, Correlated Electrons in Quantum Matter. World Scientific Publishing Company, Incorporated, 2012

[2] P. Fazekas, Lecture Notes on Electron Correlations and Magnetism, volume 5 of Series in Modern Condensed Matter Physics. World Scientific, Singapore, 1999

[3] A. Sommerfeld and H. Bethe, Elektronentheorie der Metalle. In A. Smekal, editor, Handbuch der Physik, Vol 24/2. Springer, Berlin, 1933

[4] L. D. Landau, JETP, **32**,59, 1957

[5] P. W. Anderson, Basic Notions of Condensed Matter Physics, Addison-Wesley, 1984

[6] J. M. Luttinger, Phys. Rev. **119**,1153, 1960

[7] P. Hohenberg and W. Kohn, Phys. Rev. **136**, B864, 1964

[8]W. Kohn and L. Sham, Phys. Rev. **140**, A1133, 1965

[9]W. Kohn, Nobel Lecture, Rev. Mod. Phys. **71**,1253–1266, 1999

[10] Helmut Eschrig, The Fundamentals of Density Functional Theory, Dresden, 2003

[11] D. Bohm and D. Pines, Phys. Rev. **92**,609, 1953

[12] L. D. Landau, Phys. Z. Soviet, **11**,26,545, 1937

[13] N.F. Mott, Proc R. Soc. London, **A62**,236, 1949

[14] N. F. Mott, Metal-Insulator Transitions,Taylor and Francis, London, 1990

[15] G. Kotliar, S. Y. Savrasov, K. Haule, V. S. Oudovenko, O. Parcollet, and C. A. Marianetti, Rev. Mod. Phys. **78**, 865–951, 2006

[16] D. Vollhardt, In E. Pavarini, E. Koch, D.Vollhardt, and A. Lichtenstein, editors, Hands-on LDA+DMFT. Forschungszentrum Jülich, 2011

[17] P. Thalmeier and G. Zwicknagl, Handbook on the Physics and Chemistry of Rare Earth, volume **34**, p. 135–287. Elsevier B. V., 2005

[18] P.Thalmeier, G. Zwicknagl, O. Stockert, G. Sparn, and F. Steglich, Frontiers in Superconducting Materials, p. 109–182. Springer, 2005

[19] F. Steglich, J. Arndt, O Stockert, S Friedemann, M Brando, C Klingner, C Krellner, C Geibel, S Wirth, S Kirchner, and Q Si, J. Phys. Condens. Matter **24**,294201, 2012

[20] Peter Fulde, Uwe Pulst, and Gertrud Zwicknagl, In H. Fuji, T. Fujita, and G. Oomi, editors, Transport and Thermal Properties of f-electron Systems, New York, 1993. Plenum Publishing Corporation

[21] G. Zwicknagl, Physica Scripta T **49**,34, 1993

[22] H. Aoki, S. Uji, A. K. Albessard, and Y. Onuki, Phys. Rev. Lett. **71**,2110, 1993

[23] J. D. Denlinger, G.-H. Gweon, J. W. Allen, C. G. Olson, M. B. Maple, , J. L. Sarrao, P. E. Armstrong, Z. Fisk, and H. Yamagami, J. Electron Spectrosc. Relat. Phenom. **117 & 118**,347, 2001

[24] G. Zwicknagl, Adv. Phys. **41**,203, 1992

[25] Jun Kondo, Progress of Theoretical Physics **32**(1),37–49, 1964

[26] A. C. Hewson. The Kondo Problem to Heavy Fermions. Cambridge University Press, 1993

[27] S. Ernst, S. Kirchner, C. Krellner, C. Geibel, G. Zwicknagl, F. Steglich, and S.Wirth, Nature **474**, 362 (2011)

[28] Peter Fulde, Joachim Keller, and Gertrud Zwicknagl, In F. Seitz, D. Turnbull, and H. Ehrenreich, editors, Solid State Physics, vol. **41**, p. 1. Academic Press, New York, 1988

[29] Erich Runge and Gertrud Zwicknagl, Ann. Phys. **5**,333, 1996

[30] Hilbert v. Löhneysen, Achim Rosch, Matthias Vojta, and Peter Wölfle, Rev. Mod. Phys. **79**,1015–1075, 2007

[31] P. Gegenwart, Q. Si, and F. Steglich, Nature Phys. **4**,186, 2008

[32] G. Zwicknagl and P. Fulde, J. Phys. Condens. Matter **15**,S1911–S1916, 2003

[33] P. Fulde, P. Thalmeier, and G. Zwicknagl, Solid State Physics, volume 60, chapter Strongly correlated electrons, page 1. Academic Press, 2006

[34] G. Zwicknagl and A. N. Yaresko and P. Fulde, Phys. Rev. B**68**,052508, 2004

[35] G. Knebel et al., Phys. Stat. Sol. B**247**, 557–562 (2010) ; K. Jin et al., Nature **476**, 73 (2011); Y. Takabayashi et al., Science **323**, 1585 (2009)

C-V ANALYSIS AT VARIABLE FREQUENCY OF MOS STRUCTURES WITH DIFFERENT GATES, CONTAINING Hf-DOPED TA$_2$O$_5$

L. Stojanovska-Georgievska[1], N. Novkovski[2] and E. Atanassova[3]

[1]*Institute of mathematics and physics, Faculty of electrical engineering and information technologies, Rugjer Boskovic bb, 1000 Skopje, Macedonia*

[2]*Institute of physics, Faculty of natural sciences and mathematics, Gazibaba bb, 1000 Skopje, Macedonia*

[3]*Institute of solid state physics, BAS, Tzarigadsko Chaussee blvd. 72, 1784 Sofia, Bulgaria*

Abstract. The quality of the interface between the insulating layer and the Si substrate in contemporary submicron MOS technology is a critical issue for device functioning. It is characterized through the electrically active defect centers, known as interface states. Their response to the frequency is discussed here, by analyzing capacitance-voltage and conductance-voltage curves. The *C-V* method is preferred in many cases, since it offers easy measurement, and it is applied to extract information about interface traps and fixed oxide charge, at different frequencies. This technique, related with frequency dependent *G-V* measurements, can be very useful in characterizing charge trapped in the dielectric and at the interface with Si. By extracting the value of frequency dependent flatband voltage, we have obtained the fixed oxide charges at flatband condition. A comparison between the results obtained by two different methods is made. The samples that are studied are metal-insulator-semiconductor (MIS) structures that include high-*k* dielectric as insulating layer (Hf doped Ta$_2$O$_5$), with thickness of 8 nm, with different metal used as gate electrode. Here the influence of the top electrode on the generation and behavior of the traps in the oxide layer is discussed. The results show that the value of metal work function of the gate material is an issue that should be considered very carefully, especially in the case of high work function metal gates, when generation of extra positive charge than in the case of other metals is observed.

PACS: 68.55.-a; 61.43.Dq

1. INTRODUCTION

The introduction of high-*k* materials as a replacement of SiO$_2$ in various microelectronic applications requires profound knowledge of the properties of high-*k* dielectric materials, especially the properties related with certain applications, for which high-*k* candidates have proved themselves as most suitable dielectrics. Among them Ta and Hf oxides meet the requirements for application in dynamic random access memories (DRAM's) and MOSFET's, respectively [1,2]. Pure Ta$_2$O$_5$, with its high storage ability (i.e. high permittivity in combination

with high breakdown field) and low leakage current is studied in detail. The main drawbacks of Ta_2O_5, identified as its thermodynamic instability on contact with Si, which leads to the formation of lower-*k* interfacial layer and its relatively small bandgap (4–4.5 eV), which defines small barrier heights for carrier injection, hence increased leakage current, are tailored by doping of Ta_2O_5 with a proper element or by mixing it with another oxide. It is shown [3] that this approach indeed could extend the potential of pure Ta_2O_5 as a high-*k* material, because the process of mixing HfO_2 and Ta_2O_5 modifies the dominant conducting mechanisms and changes the traps parameters as compared with pure Ta_2O_5 stacks with the same high-*k* dielectric thickness.

The aspect of the influence of top metal electrode on electric parameters of the devices with high-*k* material [4–6], especially on the evolution of degradation mechanisms and generation and behavior of bulk and interfacial traps, uncovers a lot of unsolved problems that require further studying. This especially refers to the metals with higher value of work function when used as gate electrodes on doped high-*k* structures.

2. EXPERIMENTAL

Chemically cleaned p-type (100) Si wafers with resistivity of 15 Ωcm were used as substrates. Tantalum oxide was deposited by reactive sputtering of a Ta target in an Ar + 10% O_2 atmosphere obtaining Ta_2O_5 layer approximately 7.5 nm thick; the working gas pressure was 0.33 Pa and rf power density was 3.6 W/cm^2. The Si substrate was heated at 200 °C during deposition. The Hf-doped Ta_2O_5 layers were obtained by deposition of Hf layer ~ 0.7 nm thick on the top of previously deposited Ta_2O_5 layer. Hf was deposited by sputtering of a Hf target in an Ar atmosphere. The samples were subjected to a post-deposition annealing at 400°C in N_2 for 30 min in order to mix the two layers and to ensure the diffusion of Hf into the matrix of Ta_2O_5, resulting in an 8 nm thick final layer. Top electrodes of MOS structures were formed by sputtering of TiN, Mo, Pt and Ta in an Ar atmosphere. Fabrication sequence ended with post metallization annealing in forming gas at 450 °C for 1 h.

The samples were studied by means of *C-V* measurements, at different frequencies 50 kHz, 100 kHz, 200 kHz, 500 kHz and 1 MHz, which means that the structures are tested both under low and high frequency conditions. From these measurements frequency dependence of the value of flatband voltage and fixed oxide charges is observed. For determining these values, also, the *G-V* method was used. The results obtained by these two different methods are compared.

3. RESULTS AND DISCUSION

When a MOS structure is in the depletion region, applying small ac signal causes oscillations of the Fermi level around the mean position governed by the dc bias. In these conditions the presence of interfacial states and their response to the measurement, changes the value of measured capacitance. It can be seen from the Fig. 1 that at low frequencies, the values

of capacitance of all studied structures that contain different metal gates, are higher than at high frequencies. The higher values of capacitance at low frequencies are due to excess capacitance resulting from the interface states in equilibrium with the Si-substrate that can follow the ac signal. This observation has been attributed to the capacitive response of interface states to the measurement in the case of silicon dioxide insulating layers [7] and also was observed in the case of Ta_2O_5 thin films [8]. At high frequencies the charges at the interface states cannot follow an ac signal, making no (or negligibly small) contribution of interface capacitance to the total capacitance. In the case of stacked high-*k*/ SiO_2 dielectric layers, the contribution of the border traps to the capacitance, also, has to be taken into account [9]. Since we study Ta_2O_5:Hf/SiO_2 dielectrics, it is expected that the contribution of the border traps in the Ta_2O_5:Hf layer, will be significant, which is confirmed by the measurement.
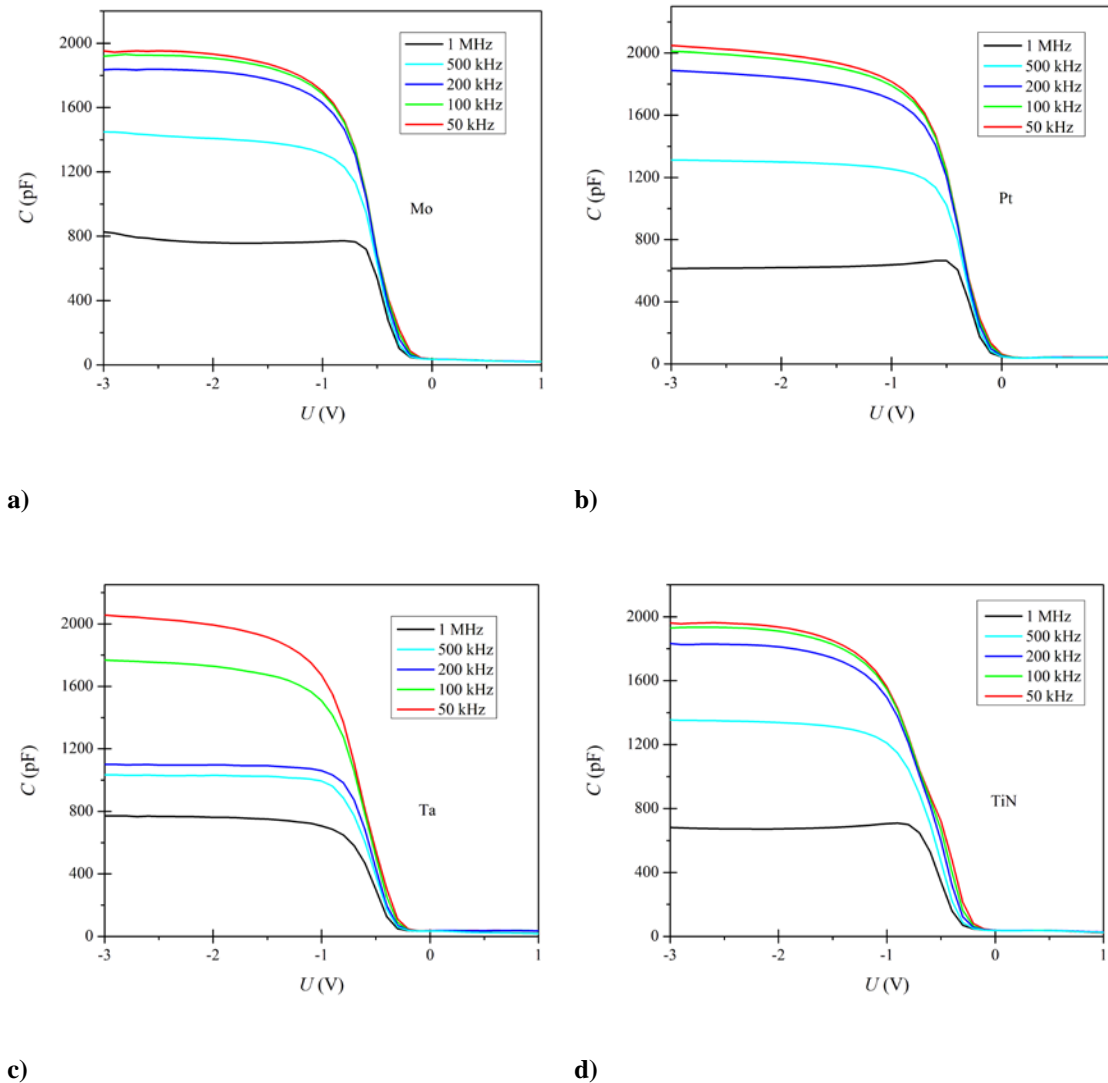

a)   b)

c)   d)

Fig. 1: Frequency dispersion of *C-V* curves of Ta_2O_5:Hf/SiO_2/Si structure, with a) Mo; b) Pt; c) Ta and d) TiN as top electrode. The capacitance alteration is measured in both directions, i.e. this represents the hysteresis of *C-V* curves.

For all samples from the obtained *C-V* curves, lowest values of capacitance in accumulation at the highest frequencies (1 MHz) were obtained (Fig.1). This observation is the same as in the case of pure Ta_2O_5, Hf doped Ta_2O_5 with Al gate and also it is observed here, in the case of Hf doped Ta_2O_5 samples with different gate electrodes (Mo, Pt, Ta and TiN). The observed hysteresis was negligible, leading to very low slow states density of the order of 10^{10} cm^{-2}.

From *C-V* curves and using the method of extraction of the values of capacitance in accumulation [10], we have obtained the values of flatband voltage and fixed oxide charges, using the standard capacitance method [11,12]. Flatband voltage is the voltage corresponding to the value of flatband capacitance (C_{FB}), calculated according to the equation (1):

$$C_{FB} = \frac{\dfrac{C_{acc}\varepsilon_s A}{\lambda}}{C_{acc} + \dfrac{\varepsilon_s A}{\lambda}}, \tag{1}$$

where C_{acc} is the capacitance in accumulation, ε_s is the permittivity of the substrate material (Si), A is the gate area and λ is the extrinsic Debye length, as calculated by:

$$\lambda = \sqrt{\frac{\varepsilon_s kT}{q^2 N_a}}, \tag{2}$$

where kT is the thermal energy at room temperature, q is the electron charge and N_a is the acceptor concentration in silicon. If the value of N_a is not given by the manufacturer of the substrate, it can be calculated by plotting the voltage dependence of $1/C^2$ [11, 12], given by the following expression

$$\frac{\partial\left(1/C^2\right)}{\partial U} = \frac{2}{q\varepsilon_0\varepsilon_s N_a A^2}. \tag{3}$$

The acceptor concentration is calculated from the slope of this plot, as presented at Fig. 2. Once the value of C_{FB} is known, the value of V_{FB} can be obtained from the *C-V* curve data, by interpolating between the closest gate-to-substrate voltage values.

Fixed oxide charges Q_{ox} for samples with different metal gates were determined, using the equation

$$V_{FB} - W_{MS} = -\frac{Q_{ox}}{C_{acc}}, \tag{4}$$

where V_{FB} is the flatband voltage, W_{MS} is the metal-semiconductor work function, and C_{acc} is the oxide capacitance. The values of metal work functions for Mo, TiN, Pt and Ta taken from literature are as follows, 4.2 eV, 4.7 eV, 5.6 eV and 4.25 eV, respectively. The obtained surface densities of the fixed charges, for samples with various gates, calculated using flatband voltage values obtained by *C-V* curves, are presented in Table 1.
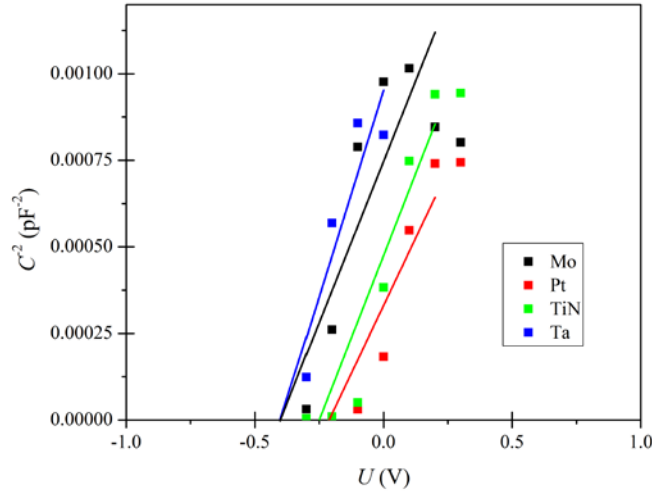
Fig. 2: Extraction of the acceptor concentration N_a of the substrate from *C-V* curves of Ta$_2$O$_5$:Hf/SiO$_2$/Si structure, with Mo, Pt, Ta and TiN as top electrode.

The presence of the interface states is evident also by their influence on the measured conductance at different frequencies (Fig. 3). Here, same as in the case of frequency dependence of *C-V* curves, there isn't any dependence of the metal used as a gate, because the frequency dependence of capacitance, as well as of conductance is due to the interfacial charges, present at the interface of the insulating layer (in this case doped Ta$_2$O$_5$ and intermediate SiO$_2$) and the Si substrate. The quality of this interface is the same for all samples, since they belong to the same manufacturing sequence, and only differ in the deposited top metal gate. G/ω-*V* curves give a pick, which is positioned at the flatband voltage. Such behavior of the G/ω peaks is attributed to particular distribution of surface states between Si/oxide interface [13]. Using this fact, we will extract the values of flatband voltage also from G/ω-*V* curves, in order to make a comparison between these two methods. These values are also presented in Table 1.

From the values presented in Table 1, it can be seen that both methods give very similar values of flatband voltage. These values show tendency to increase with the rise of the measuring frequency. This shift of flatband voltage toward higher values is due to the response of interfacial states at the interface oxide/Si substrate, that at lower frequencies contribute in the overall capacitance of the structure, which is not the case at higher frequencies. Here the influence of the gate electrode becomes obvious, since it is also included in the definition of the value of flatband voltage by equation (4). Flatband voltage for samples with Mo, Ta and TiN gate (which have similar values metal work function) are close to each other, while in the case of Pt (gate with highest work function) different values of flatband voltage are obtained.

Also it can be seen that the calculated values of oxide charges for Mo, Ta and TiN are similar, while for Pt gate it is substantially higher, i.e. in these samples an extra positive charge exists. This observation is related with the nature of the interface at the contact between the oxide and the gate. In the case of high work function metal, the position of metal Fermi level favors the transition of electrons from the oxide layer into metal conduction band, thus leaving uncompensated positive charge in the interfacial region. The presence of this extra positive

charge is registered in our calculations, too, whose values as presented in Table 1 are almost one order of magnitude higher than in the case of other gates, which are not labeled as high work function metals.
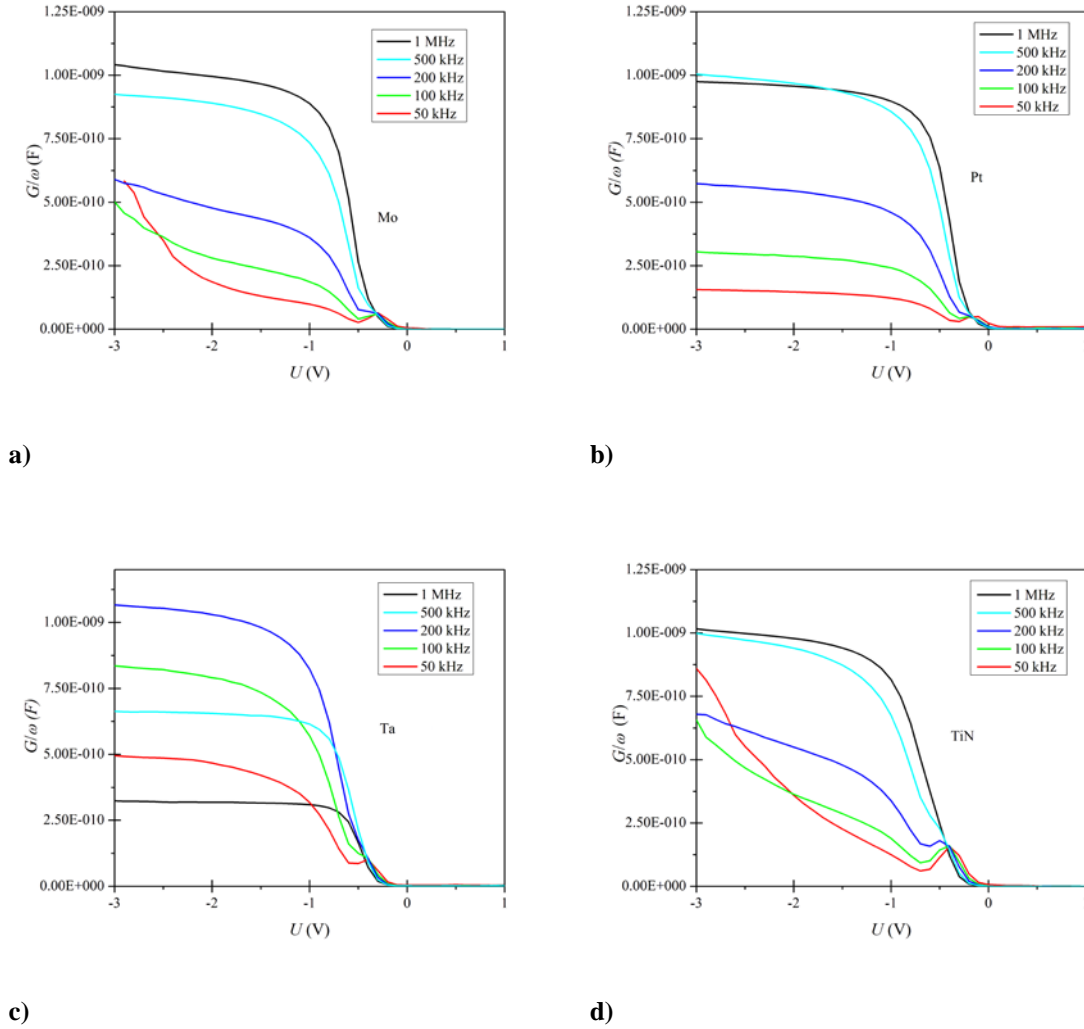

a)

b)

c)

d)

Fig. 3: Frequency dispersion of G/ω-V curves of Ta_2O_5:Hf/SiO_2/Si structure, with a) Mo; b) Pt; c) Ta and d) TiN as top electrode. The pick position corresponds to the value of flatband voltage

Table 1 Extracted values of flatband voltage and fixed oxide charges from two different methods, from *C-V* curves and from the peack position of *G/ω-V* curves

f (kHz)	C_{acc}(pF)	C_{fb}(pF) (C-U)	U_{fb} (V) (C-U)	Q_{ox} (C/cm^2)·10^{11}	U_{fb} (V) (G-U)	C_{acc}(pF)	C_{fb}(pF) (C-U)	U_{fb} (V) (C-U)	Q_{ox} (C/cm^2)·10^{11}	U_{fb} (V) (G-U)
			TiN					**Ta**		
50	1960	286	**0.32**	5.88	**0.38**	2050	288	**0.4**	10.3	**0.4**
100	1929	286	**0.35**	7.23	**0.42**	1760	282	**0.41**	9.24	**0.44**
200	1826	283	**0.38**	8.22	**0.49**	1100	257	**0.43**	6.33	**0.49**
500	1353	269	**0.42**	7.44	**0.52**	1030	253	**0.44**	6.18	**0.5**

1000	680	225	**0.43**	3.91	**0.57**	770	234	**0.47**	5.2	**0.53**
	Mo					**Pt**				
50	1950	286	**0.33**	6.34	**0.28**	2040	288	**0.19**	45.9	**0.12**
100	1920	286	**0.34**	6.72	**0.3**	2000	287	**0.2**	45.5	**0.15**
200	1840	284	**0.36**	7.36	**0.32**	1890	285	**0.21**	43.5	**0.18**
500	1450	272	**0.37**	6.16	**0.45**	1310	267	**0.21**	30.1	**0.24**
1000	827	239	**0.38**	3.72	**0.48**	620	218	**0.22**	14.4	**0.27**

The extracted values of flatband voltage by two methods and their frequency dependence are shown on Fig. 4. Fig. 5 presents frequency dependence of calculated oxide charges, for samples with different gates. It can easily be seen that only in the case of Pt gate, frequency dispersion is observed.
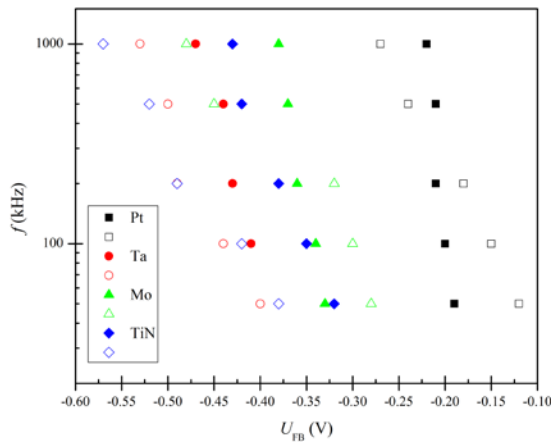

Fig. 4: Frequency dispersion of extracted values of flatband voltage for samples with different gates. Solid symbols are presenting the values obtained from *C-V* curve and open ones are for the values obtained by *G-V* curves.
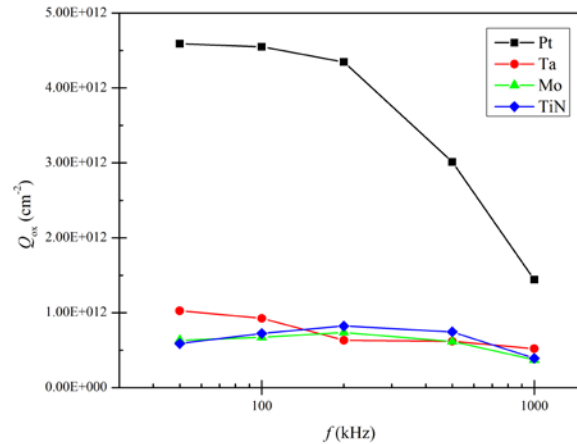

Fig. 5: Frequency dispersion of calculated surface density of fixed oxide charges, for samples with different gates.

4. CONCLUSION

In this paper we have characterized samples that contain Hf doped Ta_2O_5, alternative dielectric, marked as high-*k* material. Here we analyze the quality of the interfaces of this multilayered structure, the interface between oxide/Si substrate and metal/oxide interface. The presence of interfacial electrically active states is confirmed by their response to the measuring frequency, and therefore their influence to the flatband voltage. These values are calculated using both *C-V* and *G/ω-V* measurements, which converges toward similar values. The influence of the metal gate is strongest in the case of high work function metal, which leads to the creation of extra positive charges. These positive states are responsible for other phenomena, like charge trapping observed in the case of high work function metal gate, which is out of the scope of this paper.

Acknowledgement

REFERENCES

[1] E. Atanassova, and A. Paskaleva, "Challenges of Ta_2O_5 as high-*k* dielectric for nanoscale DRAMs", *Microelectron. Reliab.*, 2007, vol. 47, pp. 913–923.

[2] J. Lu, and Y. Kuo, "Hafnium-doped tantalum oxide high-*k* dielectrics with sub-2 nm equivalent oxide thickness", *Appl. Phys. Lett.*, 2005, vol. 87, 232906 *(3 pages)*.

[3] A. Paskaleva and E. Atanassova, "Evidence for a conduction through shallow traps in Hf doped Ta_2O_5", *Mat. Sci. Semicon. Proc.*, 2010, vol. 13, pp. 349–355.

[4] C. Mahata, T. Das, S. Mallik, M. K. Hota, S. Varma, and C. K. Maiti, "Flatband Voltage Characteristics of Hf-Incorporated Y_2O_3/Strained-Si Gate Stacks with Au, Pt, and Ni Metal Gates", *Electrochem. Solid-State Lett.*, 2011, vol. 14, pp. H30-H83.

[5] L. Stojanovska-Georgievska, E. Atanassova and N. Novkovski, "Alteration of *C-V* characteristics of metal-Ta_2O_5-Si capacitors by constant voltage stress", *Physica Macedonica,* 2008, vol. 58, pp. 107-112.

[6] A. Paskaleva, E. Atanassova and N. Novkovski, "Effects of the metal gate on the stress-induced traps in Ta_2O_5/SiO_2 stacks", *Microelectron. Reliab.,* 2008, vol. 48, pp. 514-525.

[7] H. Kanbur, Ş. Altındal, A. Tataroğlu, "The effect of interface states, excess capacitance and series resistance in the Al/SiO_2/p-Si Schottky diodes", *Appl. Surf. Sci.*, 2005, vol. 252, pp. 1732–1738

[8] L. S. Georgievska, N. Novkovski and E. Atanassova: Frequency dependence of *C-V* characteristics of unstressed HfO_2-Ta_2O_5 stacks, *Physica Macedonica*, 2012, vol. 59, pp.

[9] W.-H. Wu, B.-Y. Tsui, M.-C. Chen, Y.-T. Hou, Y. Jin, H.-J. Tao, S.-C. Chen, M.-S. Liang "Spatial and energetic distribution of border traps in the dual-layer HfO_2/SiO_2 high-k gate stack by low-frequency capacitance-voltage measurement", *Appl.Phys. Lett.*, 2006, vol. 89, 162911 *(3 pages)*

S. Kar S, "Extraction of the capacitance of ultrathin high-*k* gate dielectrics", *IEEE Trans. Electron. Dev.*, 2003, vol 50, pp. 2112–2119.

S. M. Sze, *Physics of semiconductor devices*, 2nd edition, Willey, New York, 1981.

E.H. Nicollian and J.R. Brews, *MOS Physics and Technology*, Wiley, New York, 1982.

I. Dokme and S. Altindal, The *C-V-f* and *G/ω-V-f* characteristics of Au/SiO_2/n-Si capacitors, 2007, *Physica B,* vol. 391 pp. 59-64.

PARTICIPATION OF MECHANICAL OSCILLATIONS IN THERMODYNAMICS OF CRYSTALS WITH SUPERLATTICE

S. K. Jaćimovski[1], D. Lj. Mirjanić[2],* and J. P. Šetrajčić[3],*

[1] *Academy of Criminology and Police, Cara Dušana 196, 11080 Zemun, Serbia*

[2] *University of Banja Luka, Faculty of Medicine, Save Mrkalja 11,*
78000 Banja Luka, Republic of Srpska – B&H

[3] *University of Novi Sad, Faculty of Sciences, Department of Physics,*
Trg Dositeja Obradovića 4, 21000 Novi Sad, Vojvodina – Serbia

*Academy of Sciences and Arts of the Republic of Srpska, Bana Lazarevića 1,
78000 Banja Luka, Republic of Srpska – B&H

Abstract. The superlattice, consisting of two periodically repeating films, is analyzed in proposal paper. Due to the structural deformations and small thickness, the acoustic phonons do not appear in these structures. The spontaneous appearance of phonons is possible in an ideal structure only. Therefore the thermodynamical analysis of phonon subsystems is the first step in investigations of superlattice properties. Internal energy as well as specific heat will be analyzed, too. Low-temperature behavior of these quantities will be compared to the corresponding quantities of bulk structures and of thin films. The general conclusion is that the main thermodynamic characteristics of superlattices are considerably lower than those of the bulk structure. Consequently, their superconductive characteristics are better than the superconductive characteristics of corresponding bulk structures. Generally considered, the application field of superlattices is wider than that of bulk structures and films.

1. INTRODUCTION

Possible applications of superlattices require knowledge of their thermodynamic characteristics [1]. Regardless of the type of superlattice, the thermodynamics of their subsystems (electrons, excitons, spin waves, etc) are determined when the subsystem is in thermodynamical equilibrium with the phonons [2–5]. Therefore the thermodynamical analysis of phonon subsystems is the first step in investigations of superlattice properties. Internal energy as well as specific heat will be analyzed, too. Low-temperature behavior of these quantities will be compared to the corresponding quantities of bulk structures and of thin films [6–9]. This should describe the approach which we would use for the book that deals with thermodynamics.

2. THE MODEL

It will be assumed that the symmetry is disturbed along the z-direction. Translation symmetry of the cubic structure is conserved in XY planes. In the Fig.1 the scheme of a superlattice in the z-direction, only, is given.
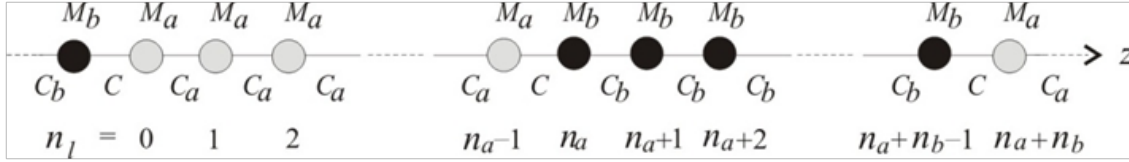

Fig. 1: The model of superlattice.

The Hamiltonian of the phonon subsystem [9] of a superlattice can be written as follows:

$$H = \frac{1}{2}\sum_{n,\alpha}^{n_a+n_b-1}\sum_{n_l=0}^{n_a+n_b-1}\left\{\sum_{n_l=0}^{n_a+n_b-1}\frac{\left[p_{n,n_l,\alpha}^{(a/b)}\right]^2}{M_{a/b}} + \frac{C_{\_/a/b}}{2}\left(u_n^\alpha - u_{n+\lambda}^\alpha\right)^2\right\}; \quad \lambda = \pm 1; \tag{1}$$

All of these formulas are given in the nearest neighbor approximation. Taking into account that a superlattice is a periodic crystal structure, the following cyclic conditions for any configuration function are valid:

$$\begin{aligned} f_{m_x m_y m_z m_l + N_{x/y}} &= f_{m_x m_y m_z m_l}; & e^{iN_{x/y}k_{x/y}a_{x/y}} &= e^{i2\pi v_{x/y}}; \\ f_{m_x m_y m_z m_l + (n_a+n_b)N_z} &= f_{m_x m_y m_z m_l}; & e^{i(n_a+n_b)N_z k_z \tilde{a}} &= e^{i2\pi v_z}. \end{aligned} \tag{2}$$

Allowed values for the z-component of the wave vector k_z are defined by integer $v_z \in \{0, \pm 1, \pm 2, \dots \dots \pm N_z/2\}$. In this way the boundaries of the first Brillouin's zone in z-direction are defined as follows:

$$k_z \in \left[\frac{-\pi}{(n_a+n_b)\tilde{a}}, \frac{\pi}{(n_a+n_b)\tilde{a}}\right], \quad \tilde{a} = \frac{(n_a-1)a^a + (n_b-1)a^b + 2a}{n_a+n_b}, \tag{3}$$

We now introduce the symbolic notation: $\vec{n} \equiv \{n_x, n_y, n_z\}, n_{x/y/z} \in \left[-N_{x/y/z}/2, N_{x/y/z}/2\right]$, where: $n_{x/y}$ is a counter of lattice nodes in x and y direction, n_z is a counter of positions along the basic motive of superlattice (z direction), n_l is a counter of node positions within the basic motive.

3. DISPERSION LAW

The phonon dispersion law will be found using the Green's function [10]:

$$G_{\vec{n},n_l,\vec{m},m_l}(t-t') \equiv \left\langle\left\langle u_{\vec{n},n_l}(t)\middle|u_{\vec{m},m_l}(t')\right\rangle\right\rangle = \theta(t-t')\left\langle\left[u_{\vec{n},n_l}t), u_{\vec{m},m_l}(t')\right]\right\rangle \tag{4}$$

with the equation of the motion of the form:

$$-M_i\omega^2 G_{\bar{n},n_l;\bar{m},m_l}(\omega)=-\frac{i\hbar}{2\pi}\delta_{\bar{n},\bar{m}}\delta_{n_l,m_l}+\frac{1}{i\hbar}\left\langle\left\langle[p_{\bar{n},n_l},H]\big|u_{\bar{m},m_l}\right\rangle\right\rangle_\omega \tag{5}$$

where $M_i\in(M_a,M_b)$. After the calculation of the commutators from (5) and application of partial configurational Fourier's transformation (this transformation is applied to coordinates x, y and z but not to coordinate l, where the translation symmetry is disturbed):

$$G_{\bar{n},n_l;\bar{m},m_l}(\omega)=\frac{1}{N}\sum_{\bar{k}}G_{n_l,m_l}e^{i[a_x k_x(n_x-m_x)+a_y k_y(n_y-m_y)+\tilde{a}_z(n_a+n_b)k_z(n_z-m_z)+J]} \tag{6}$$

where

$$J=\begin{cases}1. & a^a k_z(n_l-m_l), \quad n_l-m_l<n_a\\2. & a^a k_z(n_a-1)+ak_z, \quad n_l-m_l=n_a\\3. & a^a k_z(n_a-1)+ak_z+a^a k_z(n_l-m_l-n_a), \quad n_a<n_l-m_l<n_a+n_b\\4. & a^a k_z(n_l-1)+a^b k_z(n_b-1)+2ak_z, \quad n_l-m_l=n_a+n_b\end{cases},$$

we obtain the system of n_a+n_b non-homogeneous algebraic-differential equations for Green's functions. This model can be reduced to the model of a simple cubic lattice (and in this way simplified) with the help of substitutions:

$$a^a=a^b=\tilde{a}=a=a_z; \quad \Omega_{a_x}^2=\Omega_{a_y}^2=\Omega_{a_z}^2=\alpha\Omega_a^2;$$
$$a_x^{a/b}=a_y^{a/b}=a=a_z; \quad \Omega_{b_x}^2=\Omega_{b_y}^2=\Omega_{b_z}^2=\beta\Omega_b^2$$

$$\rho_a=\frac{\omega^2}{\Omega_a^2}-4\alpha(\sin^2\frac{ak_x}{2}+\sin^2\frac{ak_y}{2})-2\alpha; \quad \rho_b=\frac{\omega^2}{\Omega_b^2}-4\beta(\sin^2\frac{ak_x}{2}+\sin^2\frac{ak_y}{2})-2\beta. \tag{7}$$

In "cut-off" case ($\alpha=\beta=1$, $\rho_a=\rho_b=\rho$), the system of equations of phonon Green's functions in superlattices in individual layer is:

$$\rho G_s+e^{ix}G_{s+1}+e^{-ix}G_{s-1}=R_s \tag{8}$$

were are $x\equiv ak_z$. We seek for the solution equations in the form $G_s=Pe^{isx}$. Since $G_{s\pm1}=G_s e^{\pm ix}$, for Green's function we obtain the following expression:

$$G_s=\frac{R_s}{\rho+\cos 2x}. \tag{9}$$

The poles of Green's function determine value ρ, where from (9) following dispersion law of phonon was obtained:

$$\omega_{\bar{k}}=2\Omega\sqrt{\sin^2\frac{ak_x}{2}+\sin^2\frac{ak_x}{2}+\sin^2\frac{ak_s}{2}};k_s=2k_z. \tag{10}$$

In small wave-vector approximation: $\omega_{\vec{k}} = \Omega ak; \quad k = \sqrt{k_x^2 + k_y^2 + k_z^2}$, the maximal wave-vector value is determined as:

$$ak_M = a\sqrt{\frac{2}{3}k_D^2 + k_{\max}^2} = \sqrt{\frac{2}{3}\sqrt[3]{6\pi^2} + \left(\frac{2\pi}{n_a + n_b}\right)^2} \; .$$

4. THERMODYNAMICAL BEHAVIOUR

Internal energy of the system is [10]:

$$U_s = \frac{3}{(2\pi)^3}Na^3 \int\limits_0^{2\pi} d\phi \int\limits_0^{\pi}\sin\theta d\theta \int\limits_0^{k_{\max}} dk k^2 \frac{\hbar\Omega ka}{e^{\frac{\hbar\Omega ak}{\theta}}-1} \tag{11}$$

where phonon dispersion law is given by $\hbar\Omega ak$. Introducing substitution: $\hbar\Omega ak_{\max}/\theta$ after partial integration we obtain the following expression for internal energy

$$
\begin{aligned}
U_s = \frac{3N}{2\pi^2}\theta\{6\varsigma(4)\frac{\theta^3}{(\hbar\Omega)^3} - [a^3 k_M^3 Z_1(\frac{\Delta_m}{\theta}) + 3\frac{\theta}{\hbar\Omega}a^2 k_M^2 Z_2(\frac{\Delta_m}{\theta}) + \\
+ 6(\frac{\theta}{\hbar\Omega})^2 ak_M Z_3(\frac{\Delta_m}{\theta}) + 6(\frac{\theta}{\hbar\Omega})^3 Z_4(\frac{\Delta_m}{\theta})]\}
\end{aligned}
\tag{12}
$$

Since the specific heat is given by [9]:

$$C_{vs} \equiv C_s = \frac{k_B}{N}\frac{\partial U}{\partial \theta} \, , \tag{13}$$

using (12) we find that:

$$
\begin{aligned}
C_s = \frac{3k_B}{2\pi^2}\{a^3 k_M^3 \frac{\Delta_m}{\theta}\frac{1}{1-e^{\Delta_m/\theta}} - 4a^3 k_M^3 Z_1(\frac{\Delta_m}{\theta}) - 12\frac{\theta}{\hbar\Omega}a^2 k_M^2 Z_2(\frac{\Delta_m}{\theta}) - (3.2) \\
-24(\frac{\theta}{\hbar\Omega})^2 ak_M Z_3(\frac{\Delta_m}{\theta}) + 24(\frac{\theta}{\hbar\Omega})^3[\varsigma(4) - Z_4(\frac{\Delta_m}{\theta})]\}.
\end{aligned}
\tag{14}
$$

Temperature dependence of the thermal capacity is determined by two specific terms. First term is: $\approx (1 - e^{\Delta_m/\theta})^{-1}/\theta$ which is "responsible" for behavior of the system at extremely low and extremely high temperatures. Second term containing zeta functions characterizes temperature behavior in middle temperature range. Graphical presentation of the temperature dependence of relative thermal capacity $C_{bfs} \equiv C_{bfs}(x)/C_0$; $C_0 = k_B/2(\Delta/E_0)^3$; $x \equiv \theta/\theta_D$ is given on Fig.2.

5. CONCLUSIONS

The superlattice, consisting of two periodically repeating films, is analyzed in proposal paper. Due to the structural deformations and small thickness, the acoustic phonons do not appear in these structures. The spontaneous appearance of phonons is possible in an ideal structure only. The general

conclusion is that the main thermodynamic characteristics of superlattices are considerably lower than those of the bulk structure. Consequently, their superconductive characteristics are better than the superconductive characteristics of corresponding bulk structures. Generally considered, the application field of superlattices is wider than that of bulk structures and films.
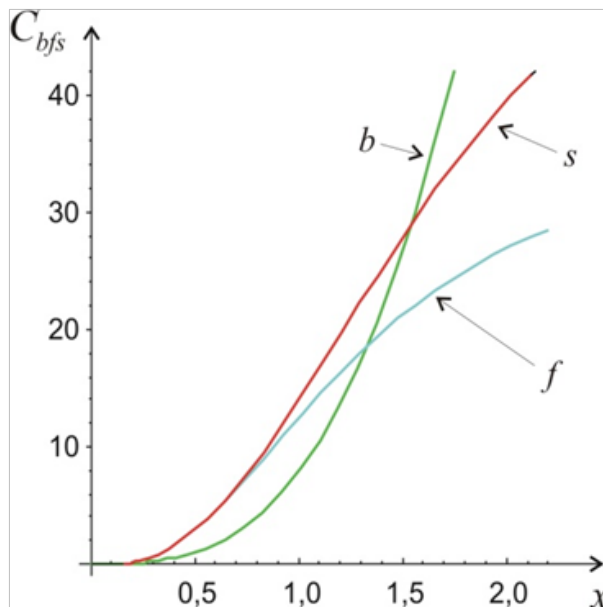

Fig. 2: Specific heats of bulk (b), films (f) and superlattice (s).

From the Fig.2 it can be concluded the behavior of thermal capacity of superlattice is similar to that of film (it is higher then in bulk structure) while difference is more expressive in middle temperature range. So, it can be concluded that the superlattices in low temperature range are somewhat better heat conductors than the bulk structures. In the same time the heat conduction of films is higher than that of superlattices. On the other hand in high temperature range superlattices are better heat isolators than film structures and the corresponding infinite crystal structures.

Acknowledgment

REFERENCES

[1] M.G.Cottam, D.R.Tilley: Introduction to Surface and Superlattice Excitations, Univ. Press, Cambridge (1989).
[2] C.Kittel: Quantum Theory of Solids, Wiley \& Sons, New York (1963).
[3] B.S.Tošić and D.Popov, J.Phys.Chem.Sol. **61**, 1561 (2000).
[4] B.S.Tošić, J.P.Šetrajčić, D.Lj.Mirjanić and Z.V.Bundalo, Physica A **184**, 354 (1992).

[5] J.P.Šetrajčić, V.M.Zorić, N.V.Delić, D.Lj.Mirjanić and S.K.Jaćimovski: Phonon Participation in Thermodynamics and Superconductive Properties of Thin Ceramic Films, Chapter 15, pp. 317-348, In „Thermodynamics", Ed.M.Tadashi, ISBN: 978-953-307-544-0, InTech, Vienna (2011).

[6] S.K.Jaćimovski, J.P.Šetrajčić, B.S.Tošić and V.D.Sajfert, Materials Science Forum **453-454**, 33-36 (2004).

[7] S.G.Davison and M.Steslicka: Basic Theory of Surface States, Clarendon, Oxford (1996).

[8] S.Lazarev, M.R.Pantić, S.M.Stojković, B.S.Tošić and J.P.Šetrajčić, J.Phys.Chem.Sol. **61**, 931 (2000).

[9] J.P.Šetrajčić, V.M.Zorić, N.V.Delić, D.Lj.Mirjanić and S.K.Jaćimovski, Phonon Participation in Thermodynamics and Superconductive Properties of Thin Ceramic Films, Chapter 15, pp. 317-348, In „Thermodynamics", Ed.M.Tadashi, ISBN: 978-953-307-544-0, InTech, Vienna (2011); Available from: http://www.intechopen.com/articles/show/title/phonon-participation-in-thermodynamics-and-superconductive-properties-of-thin-ceramic-films

[10] G.Mahan: Many Particle Physics, Plenum Press, New York (1990).

IMPEDANCE SPECTROSCOPY ANALYSIS
OF YCrO$_3$ AND YCo$_{0.5}$Cr$_{0.5}$O$_3$

M. Pecovska Gjorgjevich[1], S. Aleksovska[2] and S. Dimitrovska-Lazova[2]

[1]*Institute of Physics, Faculty of Natural Sciences and Mathematics,*

[2]*Institute of Chemistry, Faculty of Natural Sciences and Mathematics,*

"Sts Cyril and Methodius" University, 1000 Skopje, R Macedonia

Abstract. YCrO$_3$ and YCo$_{0.5}$Cr$_{0.5}$O$_3$ were prepared by solution combustion method and additionally heated at 800^{0}C for 4 hours. The X-ray diffraction analysis showed an orthorhombic phase of perovskite structure. The electrical properties of the pellets are investigated by impedance spectroscopy in the temperature range 301-339 K and frequency range 10Hz to 10MHz (bellow dielectric phase transition temperature ~ 400 K). Impedance measurements show increase of *Z'* and *Z"* with temperature, which indicates that dc conductivity decreases with heating (metallic behavior). The Nyquist plot reveals non-Debye behavior with possible two relaxation process for YCrO$_3$ and YCoCrO$_3$. The relaxation times of processes involved were calculated. The most probable relaxation times follow the Arrhenius law which allows us to estimate the activation energies of the processes in the perovskite materials. AC conductivity slope shows two processes, one starting from ~1MHz for all temperatures and another initiating from 325 K in the medium frequency range. The start of the conductivity dispersion is moving towards lower frequencies with increasing temperature. Activation energy of dc conductivity is calculated. The ac conductivity behavior is analyzed using Jonscher's power law $\sigma = A\omega^n$. The influence of Co in the structure is observed in an increasing conductivity and change in the conductivity process for higher temperatures.

PACS: 77.84.-s, 72.80.-r, 84.37.+q

1. INTRODUCTION

The perovskite-like structure, named after the CaTiO3 perovskite mineral,[1] is a ternary compound of formula ABO$_3$ where A and B cations differ in size. Perovskite structure materials play an important role in dielectric ceramics with different effects on physical properties because of variation of ionic size and small displacements of atoms which lead to the distortion of the structure and the reduction of symmetry.

The rare-earth chromate YCrO$_3$ is a perovskite like ceramic which exhibits weak ferromagnetism below T$_N$ = 140 K (canted antiferromagnetic order), and is also a weak ferroelectric below T$_C$ = 470 K, (weak polarization and dielectric anomaly appear).[2] This type of materials are called biferoics (multifunctional materials which are both ferromagnetic and ferroelectric) and are very interesting because of their potential application in technology as

high-temperature electrode and thermoelectric materials. In such materials the impedance and dielectric properties are of great scientific and technological interest.

ABO$_3$ perovskite ceramics exhibit relatively high electrical conductivity at elevated temperatures by substitution on either the A or B sites with acceptor- or donor-type cations. The factors that define their dielectric behavior are intrinsic (crystal structure, phonon interaction etc) and extrinsic (heterogenity of the medium such as porosity, impurities, grain boundaries and random crystal orientation.[3] The electrical conductivity in YCrO$_3$ is essentially due to the 3rd band of the Cr ions.[4] The modification in B ion (replacement of Cr with Co) also modify the dielectric response characteristics. YCo$_{0,5}$Cr$_{0,5}$O$_3$ is also a perovskite that shows biferoic behavior with some differences in the structure and therefore in the electric behavior. As we know ferroelectricity requires the displacement of the B cation in the ABO$_3$ structure (A and B are cations and O is anion) relative to the oxygen cage to create an electric dipole moment.

In this article we will observe impedance and conductivity changes of these two types of perovskites owing to frequency and temperature variations. Complex Impedance Spectroscopy (CIS) is a well known and powerful technique used for analysis of the electrical properties of electroceramics. It involves measurements of real and imaginary parts of impedance for a wide range of frequency and enables one to resolve the contributions of various processes such as grain effects, grain boundary and electrode polarization and activation energy of the processes involved. Complex data can be represented in any of the four related basic formalisms: complex impedance Z*, complex permittivity ε*, complex admittance Y* and complex modulus M*. Since relaxation times of processes involved are different because of different capacitive components, we use complex impedance plot (Nyquist plot) to define one, two or three semicircular arcs corresponding to high frequency end bulk electrical conduction, intermediate frequency range connected to conduction by grain boundaries and low frequency arc from electrode processes. Each of these semicircles could be represented by a single *RC* combination connected to the relaxation time of the process ($\tau = RC$), where *R* is the ohmic resistance and *C* is the capacitance of the certain circuit. The depressed semicircle with center below the real axis gives non-Debye behavior indicating the presence of CPE (distributed element). The semicircle passes through a maximum at angular frequency ω (relaxation frequency) and satisfies the condition $\omega\tau = 1$.

2. THEORY AND DISCUSION

The classical model to describe the impedance behavior is that of Debye and it is written in the form:

$$Z^* = Z' - iZ'' = \frac{R}{1 + i\omega\tau},$$ (1)

where $\tau = RC$. This equation implies a simple RC circuit in parallel which gives rise to a semicircle whose center lies on the real axis in the complex plane (*Z''* vs. *Z'*) or a Debye peak in the spectroscopic plots of the imaginary component (*Z'* vs. log *f*) where:

$$Z' = \frac{R}{1 + (i\omega RC)^2} \tag{2}$$

and

$$Z'' = R\frac{\omega RC}{1 + (i\omega RC)^2} . \tag{3}$$

In the above equations ω is the angular frequency. Usually the center of the semicircle lies off the real axis by an angle θ $(= \beta\pi/2)$. It is described by the following equation:

$$Z^* = \frac{R}{1 + (i\omega RC)^n} , \tag{4}$$

$n = 1 - \beta$, where β is the angle of deviation from the ideal semicircular arc. The simple Debye equation for the relaxation is the case for $\beta = 0$, i.e., $n = 1$. Complex impedance plane plots of Z' versus Z'' (where Z' and Z'' are the real and imaginary parts of the complex impedance plane, respectively) are useful for determining the dominant resistance of a sample but are insensitive to the smaller values of resistances.

In the present investigation, we used Impedance Spectroscopy for analyzing YCrO$_3$ and YCo$_{0.5}$Cr$_{0.5}$O$_3$ perovskite structures in temperature range 301-339 K and frequency range 10 Hz - 10 MHz. The perovskites YCrO$_3$ and YCo$_{0.5}$Cr$_{0.5}$O$_3$ were prepared by solution combustion method using urea as a fuel and additionally heated at 800^{0}C for 4 hours. The X-ray difraction analysis of the crystal structures showed that both compounds crystallize in the orthorhombic space group *Pnma* with four formula units per unit cell.

Table1. The lattice cell parameters, relative atomic coordinates, temperature factors and R-factors.in the structure of YCrO$_3$ and YCo$_{0.5}$Cr$_{0.5}$O$_3$

Атоми	Парам.	YCo$_{0,5}$Cr$_{0,5}$O$_3$	YCrO$_3$
	a (Å)	5,4725(3)	5,5210(2)
	b (Å)	7,4524(4)	7,5317(3)
	c (Å)	5,1926(2)	5,2404(2)
Y	x	0,06691(15)	0,0660(26)
	z	0,9839(3)	0,9826(5)
	B		1,79(5)
O1	x	0,4708(10)	0,4637(17)
	z	0,0993(9)	0,1104(18)
	B		1,9(3)
O2	x	0,3007(8)	0,2981(15)
	y	0,0534(5)	0,0537(10)
	z	0,6966(8)	0,6936(14)
	B		2,0(2)
R_I	R_p:	12,1	16,9
	R_{wp}:	8,97	14,9
	R_{exp}:	2,66	12,2
	χ^2:	11,3	1,49

Table2. Selected distances and angles in the structure of $YCrO_3$ and $YCo_{0.5}Cr_{0.5}O_3$.

	$YCo0,5Cr0,5O3$	$YCrO3$
Y−O1	3,317	3,3912
	2,29	2,2963
	3,074	3,1588
	2,227	2,2056
Y−O2 x 2	2,451	2,4744
	2,269	2,2861
	3,451	3,4858
	2,619	2,6487
B−O1 x 2	1,9397	1,9753
B−O2 x 2	1,977	1,9959
	1,957	1,9799
B−O1−B	146,06	143,98
B−O2−Bx 2	146,27	146,82

The lattice cell parameters, temperature factors and *R*-factors are given in Table 1, and selected distances and angles in the structure of these two perovskites is given in Table 2. $YCo_{0.5}Cr_{0.5}O_3$ has stable perovskite structure. The substitution of bigger Cr^{3+} with smaller Co^{3+} ion decreases the unit cell parameters, cell-volumes and the pseudo-parameter *a*. The distortion in $YCrO_3$ is mainly due to the octahedral tilting (Fig. 1). Substitution of Cr with Co influences change in parameters ratio *c/a*. For $YCrO_3$ $a \approx c$ and for $YCo_{0.5}Cr_{0.5}O_3$ $a>c$.
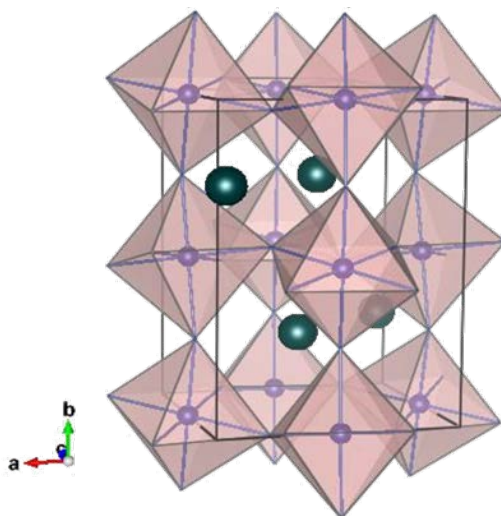

Fig. 1. The distortion of the BO_6 coordination octahedral in the orthorhombic perovskite strucure.

The sintered pellets were electroded by high purity ultrafine silver paste and then connected to the HP 4192A Impedance Analyzer for electrical characterization. We used *ac* impedance spectroscopy in order to avoid the electrode polarization. When applying the external electric field, electrically heterogeneous materials polarize and charge carriers move relatively easer through one of the phases than another one and they stack at grain boundaries. Charges build up at the interfaces and get polarized in the presence of the electric field,

depending on conductivities of the phases that build the ceramics.[3]. The real and imaginary part of the complex impedance were measured in series mode for determine bulk resistance and grain resistance of the sample. The amplitude of the applied *ac* electric field was 1V.
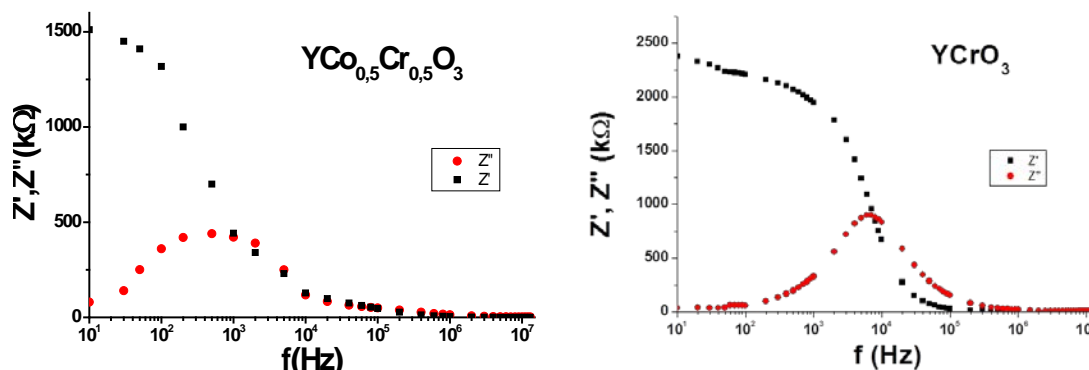

Fig. 2. Frequency dependence of real and imaginary part of YCrO$_3$ (a) and YCr$_{0.5}$Co$_{0.5}$O$_3$ (b) at 339 K.

Figure 2.a. and b. represents the frequency dependence of *Z'* and *Z"* of YCrO$_3$ and YCo$_{0.5}$Cr$_{0.5}$O$_3$ respectively. *Z'* decreases with increase in frequency for both samples implying relaxation process in the structures. The value of *Z'* is higher and *Z"* lower for YCrO$_3$ than for YCo$_{0.5}$Cr$_{0.5}$O$_3$, i.e. the conductivity is lower, because of the bigger radius of Cr. The presence of Co in the structures shifts the *Z"* peak towards lower frequencies increasing the relaxation times.
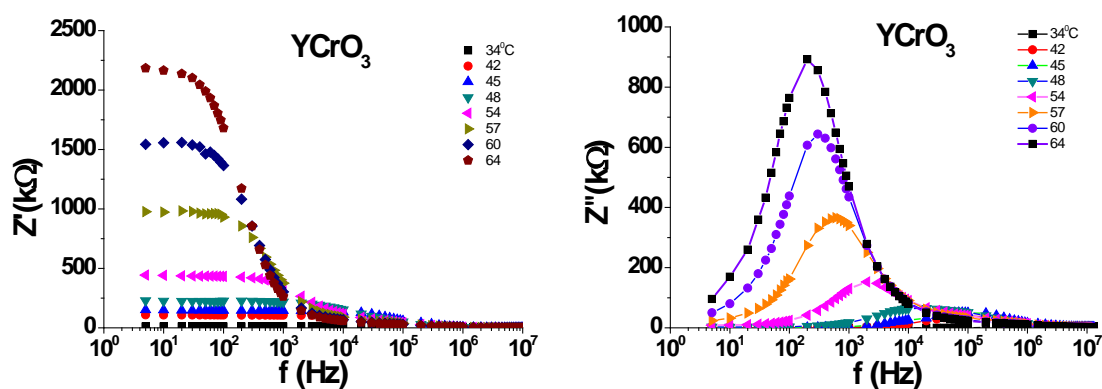

Fig. 3: Frequency dependence of *Z'* and *Z"* for YCrO$_3$ at different temperatures.

Figures 3 and 4 show the frequency dependence of *Z'* and *Z"* of YCrO$_3$ and YCo$_{0.5}$Cr$_{0.5}$O$_3$ respectively for different temperatures. Increasing of *Z'* and *Z"* and decreasing of conductivity at low frequencies with increasing temperature reveals positive temperature coefficient of resistance, i.e. metallic behavior of the samples. Release of the space charge is defined above 1MHz when all *Z'* values merge. *Z"* peak, centered at the dispersion region of *Z'*, shifts to lower frequencies with increasing temperature due to change in relaxation in the sample. A symmetric broadening of the peaks with the increase of temperature suggests the presence of temperature-dependent relaxation process of the materials.
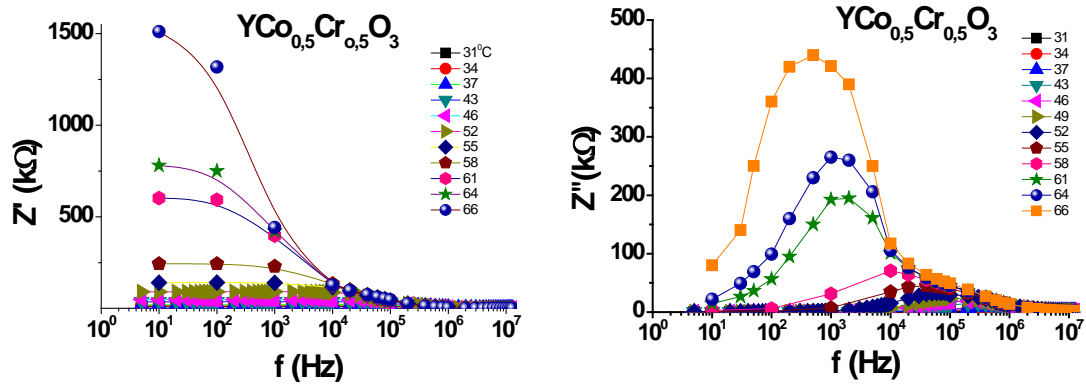
Fig. 4: Frequency dependence of *Z'* and *Z"* for YCo$_{0.5}$Cr$_{0.5}$O$_3$ at different temperatures.

The relaxation time $\tau_m = 1/\omega_m$ is determined for the position of maximum of *Z"*, where ω_m is angular frequency corresponding to this maximum. Calculated values of relaxation times for temperature interval 301– 337 K from the *Z"* versus log *f* plots are given in TABLE 3 for YCrO$_3$ and TABLE 4 for YCo$_{0.5}$Cr$_{0.5}$O$_3$. The value of relaxation times is increasing with increasing temperature which indicates conductor behavior of the structures, more pronounced for YCrO$_3$.[5] The most probable relaxation times within the investigated temperature range, follow the Arrhenius law given by:

$$\tau_m = \tau_0 \exp\left(\frac{E_a}{kT}\right), \tag{5}$$

where τ_0 is the pre-exponential factor, E_a is the activation energy of the possible process, *k* is Boltzmann constant and *T* is absolute temperature. From the linear least squares fit we observed two different slopes with obtained activation energies E_a of 0,949eV and 3,003eV for YCo$_{0.5}$Cr$_{0.5}$O$_3$ for temperature region 301-325 K and 325-337 K, and only one slope for whole temperature range with E_a= 2,73eV for YCrO$_3$.

Figure 5 represents the so-called Nyquist plot (*Z"* *vs Z'*) at different temperatures for YCrO$_3$. Here we can separate the grain effect at high frequencies from the grain boundary effect at lower frequencies. The presence of surface (electrode) polarization at low frequencies is not given on the graph. The last one is highly capacitive phenomenon, characterized by larger relaxation times than the polarization mechanism in the bulk. The results usually appear in two separate semicircles, one representing the bulk effect at high frequencies and the other surface effect at low frequency range. The sharp increase of the impedance with temperature, which is connected to the reducing of conductivity, confirms the conductive behavior of the material. Both grain and grain-boundary contribution represented with two overlapping arcs, are comparable in the material at lower temperatures. It is known [6] that, in electroceramics, if the pore size is greater than 1 μm, it would lead to the overlapping of the semicircles. With the increase of the temperature the grain boundary contribution increases rapidly and overcomes the grain effect. Single grain boundaries are insulating and with temperature increase they become dominant. The semicircle due to resistance within the grains of the materials becomes small

related to other arc due to the partial or complete blocking of charge carriers at grain boundaries. The electrical behavior of the structures can be described by RC equivalent circuits, one for the grain contribution and the other for grain boundary contribution.
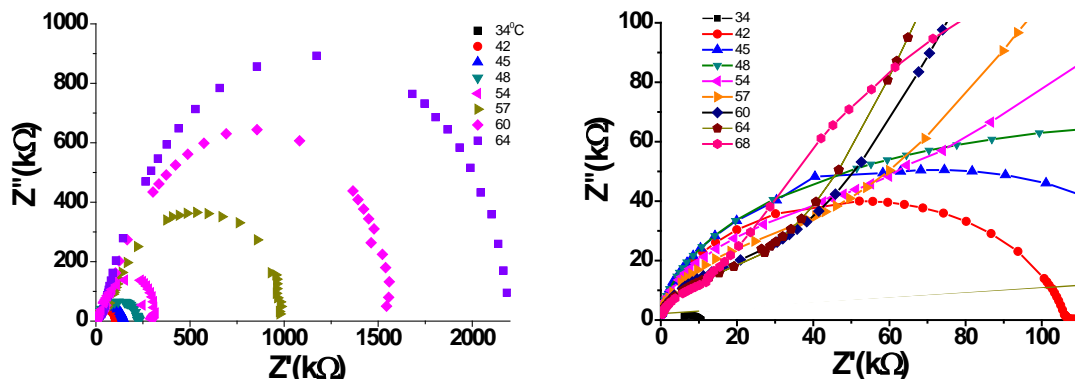

Fig. 5: a) Nyquist plot for YCrO$_3$ for various temperatures with dominant grain boundary effect. b) High frequency end of the plot showing the bulk processes in the structure.

The values of grain-boundary resistance are extracted from the intercept of the low frequency semicircle with the real axis and reveal that the rate of decrease of grain-boundary conductivity is different in different regions, which means different activation energies involved in different temperatures regions for the conductivity due to grain-boundary.[7] The grain-boundary resistance (R_{gb}) values are given in TABLE 4. The next graph, Fig.6, shows *Z' vs Z"* plot for YCo$_{0.5}$Cr$_0$.5O$_3$. The results are similar as for YCrO$_3$ with lower values of resistance. The presence of at least two depressed semicircles in the plot reveal non-Debye behavior with possible two relaxation processes for both structures. Intersection of the semicircle with the real axis shifts away from the origin with increase in temperature and the frequency of the intersection with real axis also increase with temperature.
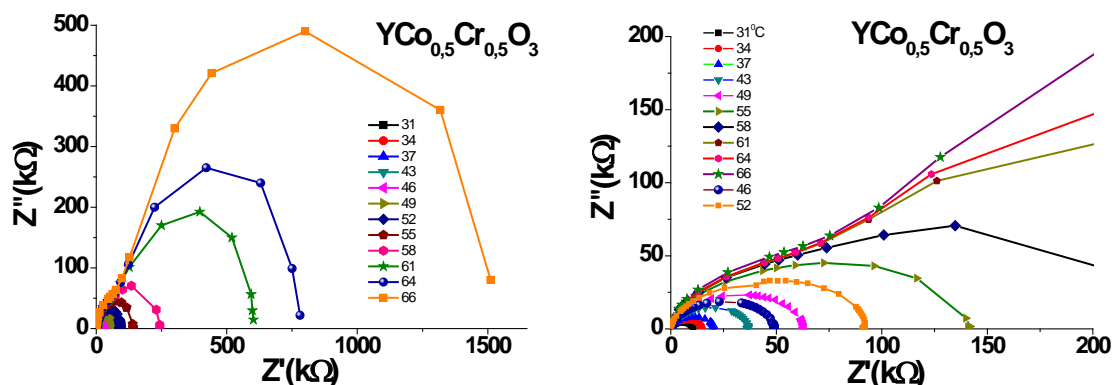

Fig. 6: a) Nyquist plot for YCo$_{0.5}$Cr$_{0.5}$O$_3$ for various temperatures with dominant grain boundary effect. b) High frequency end of the plot showing the bulk processes in the structure.

Table 3. Calculated values of grain boundary resistance, relaxation time and capacitance of YCrO$_3$.

T (K)	307	315	318	321	324	327	330	333	337
R_{gb} (kΩ)	10,5	108,6	146,6	229,9	264	441	977	1556	2184
τ (10^{-6}s)	0,177	1,59	2, 59	7,59	22,7	79,6	265	531	796
C (10^{-11}F)	0,686	1,465	1,551	3,463	8,616	18,053	27,164	34,112	36,455

Table 4. Calculated values of R_{gb}, relaxation time and capacitance of YCo$_{0,5}$Cr$_{0,5}$O$_3$.

T (K)	304	307	310	316	319	321	325	328	331	334	337
R_{gb} (kΩ)	10,4	14,1	19,7	36,1	48,9	62,5	90,9	140,8	243,8	593,4	750,2
τ (10^{-6}s)	0,027	0,027	0,318	0,796	0,796	1,59	1,99	3,98	15,9	31,8	79,6
C (10^{-11}F)	2,185	1,615	1,617	2,205	1,627	2,548	2,189	2,827	6,529	5,367	10,61

The *ac* conductivity for YCrO$_3$ and YCo$_{0,5}$Cr$_{0,5}$O$_3$ perovskites was calculated from measured real and imaginary parts of the impedance data and pellet dimensions. Figure 7 gives comparison between conductivities of two structures at 301 K showing higher values for YCo$_{0,5}$Cr$_{0,5}$O$_3$ confirming the results from the impedance measurements. We observe characteristic behavior of conductivity spectra, i.e. for low frequencies σ_{dc} is dominant and at higher frequencies conductivity increases with increasing frequency. The slope of the conductivity for high frequencies is lower for YCo$_{0,5}$Cr$_{0,5}$O$_3$ and the dispersion starts at higher frequencies compared to YCrO$_3$.
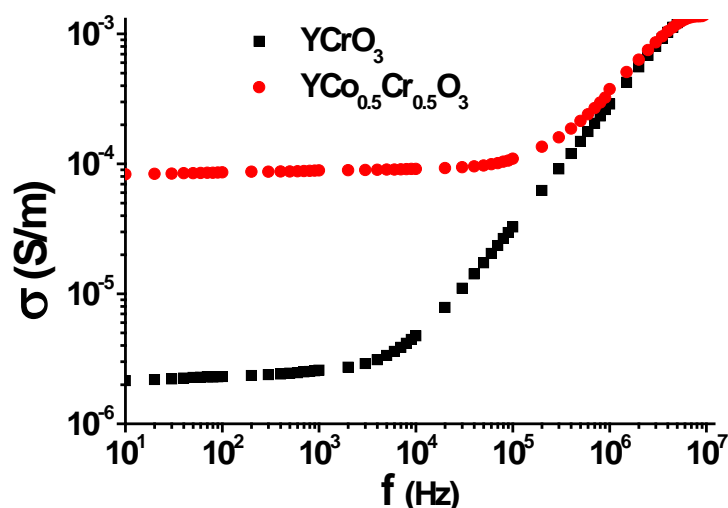

Fig. 7: Comparison of frequency dependent conductivity for both structures at 301K.

Conductivity obeys the Jonscher's power law for whole temperature region investigated:

$$\sigma = \sigma_{dc} + A\omega^n \quad , \quad 0 < n < 1 \tag{6}$$

A plateau is significant at lower temperatures and disappears with increase of temperature (Fig.7), while σ_{ac} is proportional to the increase of frequency, obeying power law. The frequency at which the dispersion region starts from the *dc* conductivity plateau can be defined as the characteristic frequency (f_p) where the relaxation effects of the ions occur. This

characteristic frequency is termed as hopping rate (f_p) or cross over frequency and it occurs at $\sigma_{fp} = 2\sigma_0$. The relation between the *dc* conductivity and the hopping rate is given by $\sigma_{fp} = k\, 2\pi f_p$ where *k* is the empirical constant, which depends on the concentration of mobile ions and type of the conduction mechanism.

Figure 8 and Figure 9 give the frequency dependent conductivity of YCrO$_3$ and YCo$_{0.5}$Cr$_{0.5}$O$_3$ respectively for various temperatures. Observed decreasing σ_{dc} with increasing temperature confirmed the conduction behavior for both YCrO$_3$ and YCo$_{0.5}$Cr$_{0.5}$O$_3$. The values of σ_{dc} obey Arrhenius plot from which we calculated activation energies for conducting process:

$$\sigma = \sigma_0 \exp\left(-\frac{E_a}{kT}\right) \tag{7}$$

The activation energy for *dc* conductivity is found to be 0,934 eV for YCrO$_3$ and 0,867 eV for YCo$_{0.5}$Cr$_{0.5}$O$_3$ until 325 K. With increasing temperature above 325 K E_a goes to 1,106 eV for YCrO$_3$ and 2,018eV for YCo$_{0.5}$Cr$_{0.5}$O$_3$. The behavior of two samples is similar, but with higher values of *dc* conductivity for YCo$_{0.5}$Cr$_{0.5}$O$_3$.
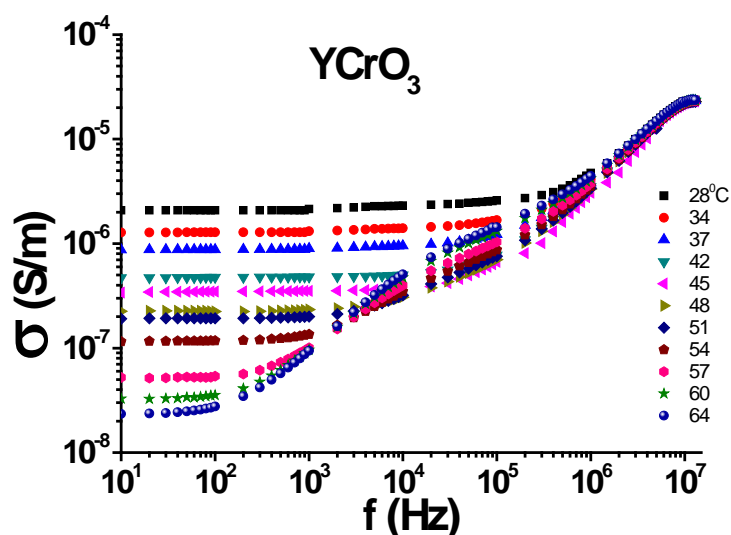

Fig. 8: Frequency dependent conductivity of YCrO$_3$ for various temperatures.

We investigated *ac* conductivity behavior with temperature for various frequencies and observed strong dependence at low frequencies and almost temperature independent conductivity at high frequencies (the region where ions are not capable of responding the alteration of external electric field).The dispersion region increases with increase in temperature, whereas characteristic frequency f_p shifts towards the low frequencies. The conductivity is changing its behavior with increasing frequency and different slopes are observed at different ranges of frequency. We observe two regions predominant with different conduction mechanisms. At the low temperature region, the conduction is presumably predominant by the extrinsic impurity conduction with a very similar activation energy, whereas the conduction at the high temperature range is likely predominant by intrinsic defects [8].
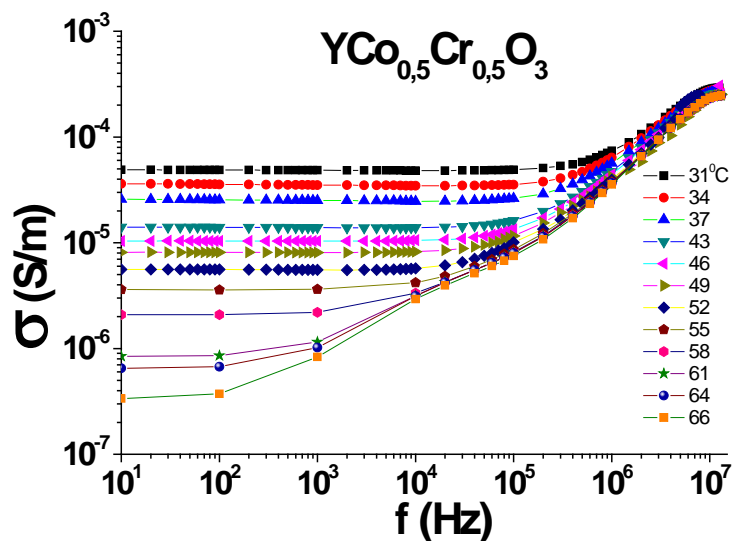
Fig. 9: Frequency dependent conductivity of $YCo_{0,5}Cr_{0,5}O_3$ for various temperatures

The activation energy for f_p was estimated to 1,007eV and 0,975eV until 325K and 2,889eV and 3,5eV over 325K for $YCrO_3$ and $YCo_{0,5}Cr_{0,5}O_3$ respectively. Compared to the activation energies for *dc* conductivity they are similar for low temperature measurements, where both grain and grain boundary effect are equally presented, and vary a great deal at higher temperatures where grain boundary effect becomes dominant.
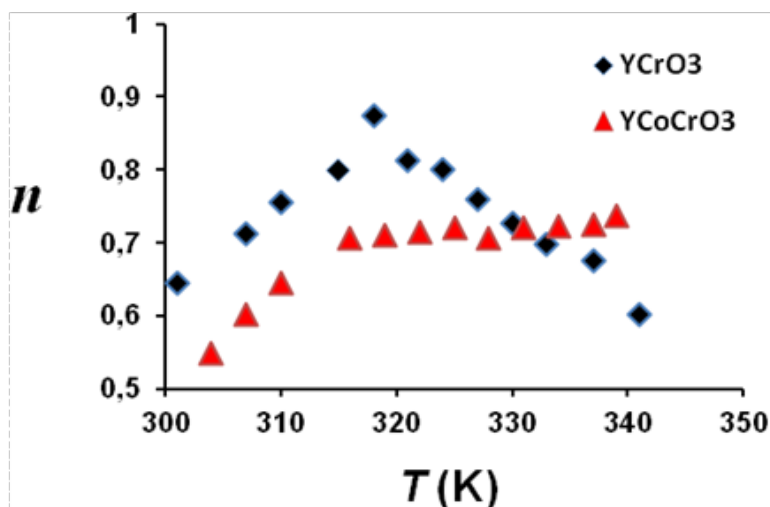
Fig. 10: Variation of exponent *n* from power law with temperature.

The results of fitting the *ac* conductivity to Jonscher power law show changes of conductivity behavior with increasing temperature. The observed enhancement of the exponent *n* with increasing temperature until 325 K for both samples with slightly higher values of *n* for $YCrO_3$, i.e. increasing *ac* conductivity is attributed to the existing oxygen vacancies and increasing concentration of ions, impurities which are more thermally activated by heating at lower temperatures. The difference in the behavior is observed for temperatures over 325 K

where *n* is decreasing for YCrO$_3$ while for YCo$_{0.5}$Cr$_{0.5}$O$_3$ remains almost constant (Fig.10). This explains the change of the slope of conductivity in YCrO$_3$ because of higher concentration of grain boundaries and constant slope in YCo$_{0.5}$Cr$_{0.5}$O$_3$. This confirms the conclusion from the X-ray diffraction analysis for more stable crystal structure of YCo$_{0.5}$Cr$_{0.5}$O$_3$ and distortion in YCrO$_3$ due to the octahedral tilting.

3. CONCLUSIONS

In this article we investigated the electrical properties of two types of perovskites YCrO$_3$ and YCo$_{0.5}$Cr$_{0.5}$O$_3$. They were prepared by solution combustion method and additionally heated at 800^{0}C for 4 hours and after submitted to X-ray diffraction analysis their structure was defined as orthorhombic space group *Pnma* with four formula units per unit cell. YCo$_{0.5}$Cr$_{0.5}$O$_3$ has stable perovskite structure, while distortion in YCrO$_3$ is mainly due to the octahedral tilting.

Influence of the substitution of Cr with Co on the impedance and conductivity is investigated for frequency range 10-10^7 Hz and temperature range 301-339 K using complex impedance spectroscopy technique involving *ac* electric field. The results reveal increase of *Z'* and *Z"* and decrease of conductivity with temperature confirming metallic behavior of the structures. From the Nyquist plot we observed two relaxation processes for both samples, i.e. both grain and grain boundary contribution are present in the relaxation process. Their behavior is similar, but the impedance is lower i.e., conductivity is higher for YCo$_{0.5}$Cr$_{0.5}$O$_3$ confirming better structure with less grain boundary defects which influence its electrical behavior. The values of R_{gb} for different temperatures were extracted from the plot and they confirm the previous conclusion since YCo$_{0.5}$Cr$_{0.5}$O$_3$ has lower values of resistance than YCrO$_3$. The broadening of *Z"* with increase of temperature suggests temperature dependent relaxation process. The values of activation energies calculated from the slope lnσ versus 1000/T are similar to those obtained from Arrhenius plot of relaxation times. The *ac* conductivity behavior is analyzed using Jonscher's power law $\sigma = A\omega^n$. Both structures have similar behavior at low temperatures with lower value of *n* for YCo$_{0.5}$Cr$_{0.5}$O$_3$. The influence of Co in the structure is observed in the high frequency region where the value of *n* is almost constant, while for YCrO$_3$ it is decreasing.

REFERENCES

[1] Principles of Electronic Ceramics, L. L. Hench and L. K. West, John Wiley & Sons,Inc., (1990), pp 244-247.

[2] Observation of local non-centrosymmetry in weakly bifferoic YCrO$_3$, K.Ramesha, A.Llobet, Th. Proffen, C. R. Serrao and C. N. R, Rao, *J.Phys: Condens. Matter* **19,** 102202 (2007)

[3] Effect of sintering on microstructure and dielectric response in YCrO$_3$ nanoceramic, J.Bahadur, D.Sen, S Mazumder, V.K. Aswal, V. Bedekar, R. Shukla and A. K. Tyagi, pp.959-963,*Pramana- Journal of Physics,* **71**, 5 (2008)

[4] Formation, powder characterization and sintering of $YCrO_3$ prepared by sol-gel technique using   hydrazine, T.Tachiwaki, Y.Kunifusa, M. Yoshinaka, K.Hirota, O.Yamaguchi, International   *Journal of Inorganic Materials* **3**, 107-111 (2001)

[5] Crystallographic phases, phase transitions and barrier layer formation in $(1-x)$ $[Pb(Fe_{1/2}Nb_{1/2})O_3]-x$PbTiO$_3$, Singh S P, Singh A K, Pandey (2003) *J. Mater. Res.* **18** (11) 2677-2687

[6] Densification of Yttria-stabilized zirconia impedance spectroscopy analysys, M. C. Steil, F . Thevenot and M. Kleitz, *J. Electrochem.Soc.* **144** (3) (1997) 390

[7] Impedance spectroscopy analysis of double perovskite Ho_2NiTiO_6, Dev K. Mahato, A. Dutta, T.   P. Sinha, *J. Mater. Sci.* (2010) **45**:6757–6762

[8] Dielectric properties of layered perovskite $S_{1-x}A_xBi_2Nb_2O_9$ ferroelectrics. A=La,Ca and x=0,0.1., M. J. Forbess, S. Seraji, Y. Wu, C. P. Nguyen, and G. Z. Caoa, *Appl. Phys. Lett.*, **76** (20)

NANOPARTICLE MANIPULATION BY DIELECTROPHORESIS

A. Neculae, R. Giugiulan and M. Lungu

West University of Timisoara, Faculty of Physics, Blv. V. Parvan no.4, 300223 Timisoara, Romania

Abstract. In the last decades, non-uniform electric field proved to be the most promising technique for nanoparticles manipulation with applications in fields such as medicine, biology, physics or nanotechnology. The paper presents a set of numerical results concerning the influence of the dielectrophoretic (DEP) forces on a nanoparticle suspension. The DEP force depends on the electric properties of the nanoparticles, as well as their shape, size and mass, and the properties of the surrounding medium. The numerical study was performed in the frame of a mathematical model describing the electric field distribution and the suspended nanoparticle movement in a dense and viscous fluid. The equations are solved, together with the appropriate boundary conditions using a code based on the finite element method. The dielectrophoretic force distribution, the particle trajectories and the nanoparticle concentration profile are computed. This type of analysis leads to the optimization of the control parameters and is crucial in the designing process of an experimental microfluidic device with application in the separation of submicronic particles.

PACS: 02.60.Cb, 47.11.Fg, 47.61.Fg, 47.57.E-

1. INTRODUCTION

Dielectrophoresis (DEP) is a phenomenon in which, under spatially non-uniform AC or DC electric fields, dielectric particles move because of the interaction of the dipole induced in the particle and the applied field gradient [1]. This interaction does not require the particle to be charged and its strength depends strongly on the medium and particles' electrical properties, on the particles' shape and size, as well as on the frequency of the electric field. In classical dielectrophoresis, the positive DEP force attracts particles into the regions of strong electric fields, while negative DEP force repels them from those regions [2]. DEP methods can be used in many forms (electrorotation, traveling wave DEP, negative and positive DEP) to manipulate and more generally, control the position, orientation and velocity of micro- and nanometer scale particles, including carbon nanotubes and biological particles such as viruses, DNA, bacteria and cells of various kinds [3].

This paper represents a numerical study on the behavior of a suspension of submicron particles under the action of dielectrophoretic force in a system consisting of a micro-channel controlled with an interdigitated electrode array. The reported results concern the influence of the geometry and experimental parameters on the dielectrophoretic force, particle trajectories and concentration field.

2. THEORETICAL CONSIDERATIONS

To compute the electric field and the dielectrophoretic forces, the electric potential is solved for a defined space and set of boundary conditions (that represent the electrode array). In this paper phasor notation is used, with an arbitrary potential oscillating at frequency ω defined as [4]:

$$V(\mathbf{x},t) = \text{Re}\{\tilde{V}(\mathbf{x})e^{j\omega t}\}, \tag{1}$$

where $j = (-1)^{1/2}$, $\mathbf{x}$ is the coordinate, Re{} indicates the real part and the tilde indicates the phasor $\tilde{V} = V_R + jV_I$, with V_R and V_I the real and respectively imaginary part of the electric potential.

For a homogeneous medium, the electrical potentials satisfy the Laplace's equation:

$$\nabla^2 V_R = 0 \quad \text{and} \quad \nabla^2 V_I = 0, \tag{2}$$

and the time-averaged dielectrophoretic force can be expressed as [6]:

$$\langle \mathbf{F}_{DEP} \rangle = \frac{3}{4}\varepsilon_m \tilde{k}_r(\omega)\nabla\left(\left|\nabla V_R\right|^2 + \left|\nabla V_I\right|^2\right), \tag{3}$$

where $\tilde{k}(\omega)$ is the Clausius–Mossotti (CM) factor: $\tilde{k}(\omega) = \tilde{\varepsilon}_p - \tilde{\varepsilon}_m / \tilde{\varepsilon}_p + 2\tilde{\varepsilon}_m$, with $\tilde{\varepsilon}_p$ and $\tilde{\varepsilon}_m$ the absolute complex permittivity of the particle and the medium, respectively, and depends on the dielectric properties of the particles and medium and on the geometry of the particles. The complex permittivity is $\tilde{\varepsilon} = \varepsilon - j\sigma / \omega$, where ε represents the electric permittivity and σ the conductivity of the dielectric. The real part $\tilde{k}_r(\omega)$ of CM factor gives the DEP force in the vertical direction. In a dielectric medium, the direction of the DEP force is influenced by the polarizability of the particle, which depends on the permittivities of the particle and the suspending medium. When the sign of $\tilde{k}_r(\omega)$ is positive, the particle is more polarizable than its surrounding medium and its movement is oriented towards regions of highest field strength, known as positive dielectrophoresis (pDEP). When Re{k} is negative, particles with polarizability less than that of the medium move towards the region of lowest field gradient, known as negative dielectrophoresis (nDEP).

The macroscopic behavior of a suspension of spherical particles in a dense and viscous fluid can be modeled considering the mechanical equilibrium between an external spatially dependent force $\mathbf{F}$ and the Stokes drag. When the size of the particles, relative to the length of the microchannel and the volume fraction φ of particles is small, the dynamics of the two-phase system can be expressed by the following system of equations [6]:

$$\begin{aligned}\mathbf{v} &= \mathbf{u} + \frac{2a^2}{9\eta}\mathbf{F}, \quad \text{where} \quad \nabla\mathbf{u} = 0 \\ \frac{\partial\varphi}{\partial t} + \nabla\cdot\mathbf{j} &= 0, \quad \text{where} \quad \mathbf{j} = \varphi\mathbf{v} - D\nabla\varphi.\end{aligned} \tag{4}$$

Here **u** and **v** are the fluid and particle velocities, respectively, a the particle radius, η the viscosity of the fluid, t the time, **j** the particle flux, D the diffusion coefficient of the particles and **F** denotes the dielectrophoretic external field.

In order to avoid extreme numbers in the numerical calculations, the potential is scaled with V_0, the amplitude of the applied signal, and the distances are scaled with d, the width of the electrode.

In terms of dimensionless electric potentials $V'_R = V_R/V_0$, $V'_I = V_I/V_0$ and displacement **x'**=**x**/d, the time-averaged expression for the dielectrophoretic force becomes:

$$\langle \mathbf{F}_{DEP} \rangle = F_{0DEP} \nabla' \left(\left| \nabla' V'_R \right|^2 + \left| \nabla' V'_I \right|^2 \right), \quad \text{where} \quad F_{0DEP} = \frac{3}{4} \varepsilon_m \tilde{k}_r \frac{V_0^2}{d^3}. \tag{5}$$

Using the scales of $d, d^2/D, D/d$ and φ_0 (the initial average volume fraction) for the length, time, velocity and particle volume fraction, respectively, the macroscopic transport is expressed in terms of dimensionless variables by the following system of equations:

$$\begin{aligned} \mathbf{v}' &= \mathbf{u}' + Q\mathbf{F}', \quad where \quad \nabla \mathbf{u}' = 0 \\ \frac{\partial \varphi'}{\partial t'} + \nabla \cdot \mathbf{j}' &= 0 \quad where \quad \mathbf{j}' = \varphi'\mathbf{v}' - D\nabla\varphi' \end{aligned}. \tag{6}$$

The prime symbol above denotes the dimensionless quantities, $Q = 2a^2 F_0 d / 9\eta D$ with F_0 a measure of the intensity of the external field.

3. NUMERICAL RESULTS AND DISCUSSIONS

All the numerical simulations were performed using a finite element code, FreeFEM++ [7]. Figure 1 presents a typical DEP array of rectangular shape electrodes. We noted with d the electrode width, l the distance between two adjacent electrodes, w the electrodes height and h the dielectrophoretic chamber height.
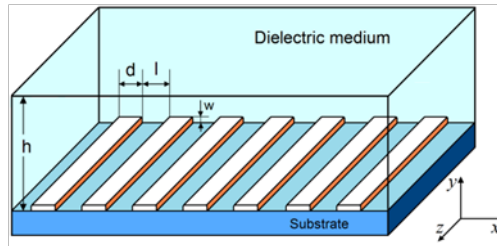
Fig. 1: Schematic of the dielectrophoretic chamber with interdigitated bar electrodes at bottom surface used for DEP separation.

For the computation of the dielectrophoretic force, we solved the Laplace's equations (2) for the real and imaginary components of the potential, together with the associated boundary conditions. Due to the symmetry of the problem and considering the electrodes long compared to their width, problem can be treated as two-dimensional. The computational domain

and the boundary conditions can be assumed as in Figure 2, where the particular case $l = d$ and $h=2d$ was considered.

Fig. 2: Computational domain with boundary conditions for the real part V_R of the electric potential.

The numerical analyses were performed for a computational domain with electrodes of dimensionless width $d' =1$ and different shapes. The calculated values of the magnitude of dimensionless dielectrophoretic force $\langle \mathbf{F}_{DE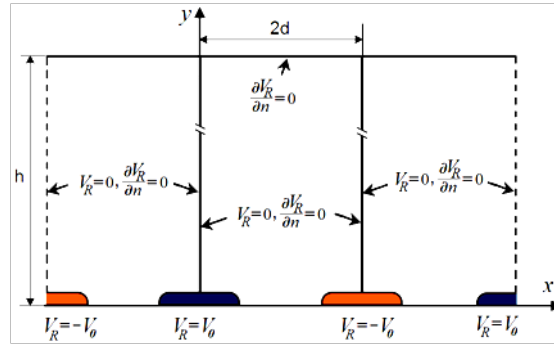P} \rangle / F_{0\,DEP}$ in the case of electrodes with negligible height and with elliptic shape, respectively, are presented in Figures 3(a) and 3(b) respectively.In both cases, the magnitudes of the computed quantities, and consequently the effect of the DEP force, increase to a maximum value at the electrode edge and diminish rapidly with the distance on vertical direction.
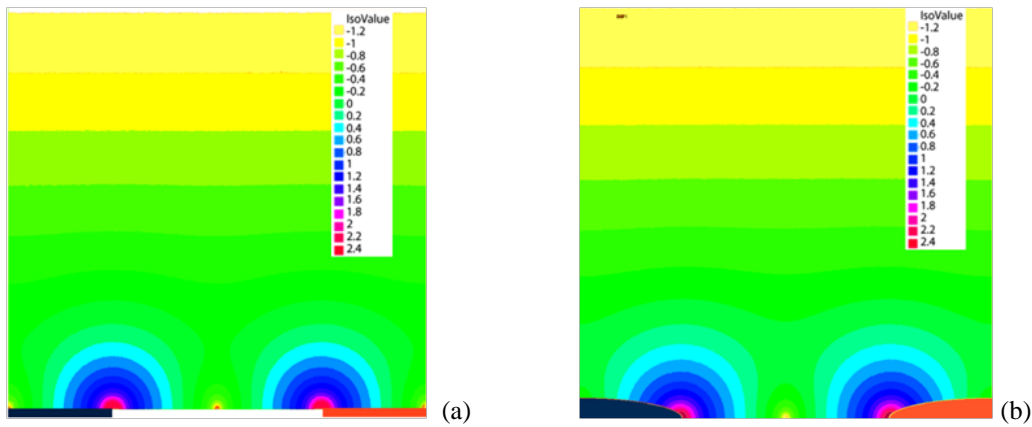
Fig. 3: Calculated values for the magnitudes of the dimensionless DEP force $\langle \mathbf{F}_{DEP} \rangle / F_{0\,DEP}$, plotted on logarithmic scale; (a) plane electrodes, (b) elliptic electrodes.

The analysis of particles trajectories is performed by integrating the dimensionless movement equation (6a) and considering a Poiseuille flow profile for the fluid, with a maximum value of dimensionless velocity equal to unity. The computed trajectories for particles entering the computational domain at $x'_0=0$ and different values of y'_0 in the case of positive and negative DEP are shown in Figures 4 (a) and (b) respectively. As it can be seen, the trajectories are strongly influenced by the DEP force in the vicinity the electrode. When the distance particle-electrode is large, the influence of the DEP force is very week. This analysis reveals that the

nanoparticles in suspension tend to concentrate to the channel walls for positive DEP or to the channel center for negative DEP.
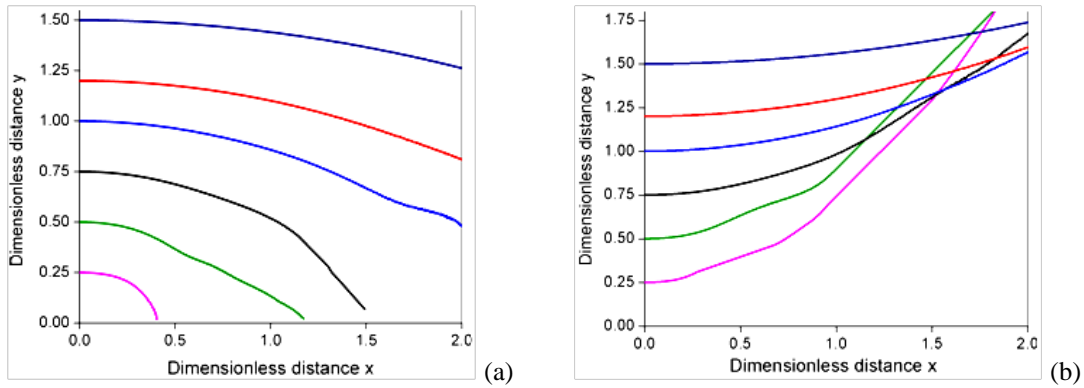
Fig. 4: Calculated particle trajectories in case of positive DEP (a), negative DEP (b).

The global concentration field is influenced both by the DEP force and the velocity of the fluid flow. In figures 5a,b we present two examples of computed stationary concentration field in the case of a typical force parameter $Q=0.2$ (positive DEP) and two different flow velocity values.
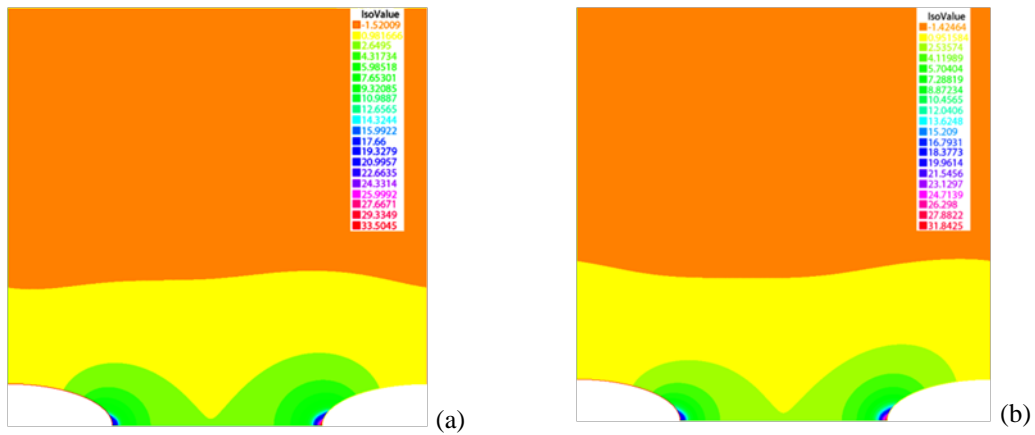
Fig. 5: Positive DEP for $Q=0.2$ and $v=1$ (a), and $v=10$ (b).

The assembly of numerical results shows that in the case of positive DEP the nanoparticles in suspension tend to concentrate on electrodes edge. Depending on their properties (nature, size), the concentration profile can be controlled by adjusting the applied voltage at the command electrodes and the fluid flow.

4. CONCLUSIONS

The paper presents a set of numerical results concerning the description of the nanoparticles behavior in a suspension under the action of DEP force. As $\tilde{k}_r(\omega)$ is a complex function of particle and fluid properties (permittivity, conductivity) and frequency of the applied field, a particle can experience both positive and negative DEP forces at different combinations of the above variables. The results reveal the influence of the main experimental parameters on the dielectrophoretic effect on the suspension's concentration field and provide an important tool in the particle manipulation within microfluidic systems.

Acknowledgements

REFERENCES

[1] N.G. Green and H. Morgan, J. Phys. D: Appl. Phys. **31**, L25-L30(1998).

[2] C. Zhang, K. Khoshmanesh, A. Mitchell and K. Kalantar-Zadeh, Anal. Bioanal. Chem. **396**, pp. 401–420 (2010).

[3] M.P. Hughes, Nanotechnology, 11 (2000).

[4] H. Morgan and N.G. Green, in "Research Studies" ltd. Baldock, **50–62**, pp. 200–210 (2003).

[5] N.G. Green, A. Ramos and H. Morgan, J. of Electrostatics **56**, pp. 235-254 (2002).

[6] M. Lungu, A. Neculae and M. Bunoiu, AIP Conf. Proc. **1162**(1), pp. 144-149 (2010).

[7] www.freefem.org.

CONTROLLED RELEASE STUDIES OF CALCIUM ALGINATE HYDROGELS

S. Rendevski[1], A. Andonovski[2], N. Mahmudi[3]

[1]*Faculty of Electrical Engineering, University "Goce Delcev", Krste Misirkov, b.b., 2000 Stip, Republic of Macedonia*

[2] *Faculty of Natural Sciences and Mathematics, University "Ss. Cyril and Methodius", Gazi Baba, b.b., 1000 Skopje, Republic of Macedonia*

[3] *Faculty of Natural Sciences and Mathematics, State University of Tetovo, bul. Ilinden, b.b., 1200 Tetovo, Republic of Macedonia*

Abstract. Controlled release of substances in many cases may be achieved from calcium alginate hydrogels. In this research, the time dependence of the mass of released model substance bovine serum albumin (BSA) from calcium alginate spherical hydrogels of three different types (G/M ratio) have been investigated. The hydrogels were prepared with the drop-wise method of sodium alginate aqueous solutions with concentration of 0.02 g/cm^3 with 0.01 g/cm^3 BSA and a gelling water bath of chitosan in 0.2 M CH$_3$COOH/0.4 M CH$_3$COONa with added 0.2 M CaCl$_2$.The hydrogel structures were characterized by dynamic light scattering and scanning electron microscopy. The controlled release studies were conducted by UV-Vis spectrophotometry of the released medium with pH=7 at 37 ^{0}C. The results showed that the model of osmotic pumping is the dominant mechanism of the release. Also, large dependences of the release profile on the homogeneity of the hydrogels were found.

PACS: 47.57.Ng; 82.70.Gg; 87.85.jf

1. INTRODUCTION

Controlled release systems of active substances are widely used in many applications in medicine, chemical technology, food technology, etc. Although the active substances can be various, the matrix (or carrier of the active substance) is common for all of them. The type of the matrix mainly determines the effects of the controlled release. Most common phenomena that are used for choosing type of the matrix are: diffusion of the active substance through the matrix; erosion of the matrix caused by some chemical reaction; swelling of the matrix at contact with the surrounding fluid; and osmotic pumping of the active substance out of the matrix. Most important criterion that must be followed when choosing the type of the matrix is to develop a system with controlled release properties that do not depend significantly on the change of the physico-chemical conditions in the controlled release surroundings (media). At the same time the kinetics of release of the active substance should be reproducible and

predetermined [1]. When studying kinetics of controlled release of active substance from hydrogel particles of calcium alginate with chitosan membrane, three different types of controlled release systems have been investigated: reservoir with membrane, erosion type and osmotic type. Choosing the system type reservoir with membrane is based on the fact that the gel matrix of calcium alginate (CA) is wrapped in a membrane of chitosan that stays stable from the start of the release of the active substance to the manifestation of the "osmotic breaking" when the membrane is ruptured due to high internal osmotic pressure in the matrix. From the start of active substance release from CA particles with membrane of chitosan to the "osmotic breaking" of the matrix, the system becomes complicated. In between these two phases the active substances diffuse in the interior of the matrix because of the gel's erosion. The gel's erosion is caused from the fluid diffusion from the surrounding environment with ionic strength of 0.1 M NaCl or higher. When number ratio of Na^+ ions over against Ca^{2+} ions embedded to the guluronic monomers of the alginate macromolecules in the gel are less then 1:25, an exchange of the Ca^{2+} ions in the gel with the Na^+ ions occurs that destabilizes the gel structure and causes gel's dissolution (washing) [2].

The experimental investigation of the controlled release properties is based on determination of the kinetics of release, i.e. accumulative released mass of active substance in the releasing bath at different times, M_t, starting from the null time (after the moment of positioning the controlled release system into the releasing bath) and up to the moment of total dissolution (disintegration) of the release matrix. The second important quantity to investigate is the release rate, dM_t/dt – first derivative of the accumulative released mass over time t.

For the controlled release model of reservoir with membrane, when the reservoir is with definite volume V_1, and the releasing bath is considered as infinite because of the much larger volume of the reservoir, the mass of the released active substance and the release rate over time t is determined by the expressions [3]:

$$M_t = M_1 \left[1 - e^{-\frac{A \cdot D_m K}{\delta \cdot V_1} t} \right], \tag{1}$$

$$\left(\frac{dM_t}{dt} \right)_r = \frac{M_1 \cdot A \cdot D_m \cdot K}{\delta \cdot V_1} \cdot e^{-\frac{A \cdot D_m K}{\delta \cdot V_1} t}, \tag{2}$$

where M_1 is a mass of the active substance of the reservoir.

For the erosion model of controlled release of calcium alginate gel particles with radius a with chitosan membrane in large volume of releasing bath (infinite volume), the dependence of the released mass M_t of active substance over time t is given according to relation [3]:

$$\frac{M_t}{M_\infty} = 1 - \frac{6}{\pi} \sum \frac{1}{n^2} \cdot e^{-\frac{D_a n^2 \pi^2}{a^2} t} \tag{3}$$

where M_∞ is a released mass at time of total erosion of the gel matrix, D_a is a diffusion coefficient of the active substance in the dissolved gel. In Eq (3), number of the summing parts

n used for calculation is usually taken to a value at which there is no significant divergence between the calculated at measured quantities M_t/M_∞. For the osmotic pumping model for system with constant volume, the volume rate of release of active substance in releasing bath is equal to the volume rate of diffusion of water into the gel system. The dependence of the released mass M_t of active substance over time *t* for this model is given according to relation [3]:

$$\left(\frac{dM_t}{dt}\right)_r = \sigma RTA\frac{L_p}{\delta}C_a^2 , \tag{4}$$

where σ - coefficient of fluid reflectivity of the gel membrane (equal to 1 for ideal semipermeabile membrane and equal to 0 for nonporous membrane), *R* – universal gas constant, *T* – temperature, A – surface area of membrane pores, L_p – coefficient of hydraulic membrane's permeability, δ - membrane thickness, C_a – active substance concentration in the gel matrix.

2. EXPERIMENTS

A bovine serum albumin (BSA) was used as an active substance in this research. The purpose of the research was to investigate the influence of the inhomogenity of the internal structure of calcium alginate gel particles with chitosan membrane on the controlled release properties. Three different types of sodium alginate were used in this research: type LF120M with weight-average molecular weight of $M_w = 671\cdot10^3$ g/mol and G/M ratio of 50/50, type LF200M with $M_w = 687\cdot10^3$ g/mol and G/M ratio of 55/45 and LF240D with $M_w = 497\cdot10^3$ g/mol and G/M ratio of 70/30. The gel spherical particles were obtained by the drop-wise method [4,5]. For each type of alginate the procedure for obtaining gel particles with membrane is the same as the following. The gelling solution of sodium alginate has a concentration of 2 % w/w in double distilled and deionized water in which BSA with concentration of 1 % w/w was added and well mixed for 24 h. The gelling bath was a solution of chitosan ($M_w = 5.67\cdot10^4$ g/mol, deacetlylation degree 0.88) with concentration of $0.25\cdot10^{-2}$ g/cm^3 in 0.2 M CH$_3$COOH/0.4 M CH$_3$COONa with added 0,2 M CaCl$_2$ as a gelling agent for ionic gelation. The CA gel particles were obtained by setting drops of the gelling solution from a needle in the gelling bath at 25 ^{0}C put on a magnetic stirrer with 300 rpm. After the first contact of the drops and the gelling medium, chitosan membrane is immediately formed. After 1 h of steering, the gel spheres were washed with distilled water and were ready for controlled release characterization. This is the procedure for obtaining homogenous gel particles. The only difference for the inhomogeneous gel particles was that in the gelling bath of sodium alginate 1 mM CaCl$_2$ and 10 mM CaCl$_2$ were added as inducer of aggregated structures that are spread through the gel matrix after finishing full gelation from such systems. The sizes of the aggregated structures (microgel domains) in the gelling solution were measured by dynamic light scattering techniques. The inhomogeneities of the gels are visible on SEM pictures obtained in this research (fig.1 and fig.2). We found that size of gel particles do not depend on

type of alginate. The size change depends only on the concentration of added $CaCl_2$ in the gelling solution. The diameter of gel particles is average value of measurements on ten different particles: - for particles without $CaCl_2$, $d = (2.45 \pm 0.35)$ mm; - for particles with 0.1 mM $CaCl_2$, $d = (2.70 \pm 0.55)$ mm; - for particles with 10 mM $CaCl_2$, $d = (3.00 \pm 0.75)$ mm.

Controlled release studies were conducted as the following [5]. A releasing bath is thermostated at 37 ^{0}C on a magnetic stirrer on 300 rpm. The releasing bath is a phosphate buffer solution with pH = 7.4. The releasing bath contains 0.1 M NaCl that breaks the calcium bridges in the gel matrix and thus disintegrate the gel because diffusion of releasing medium through chitosan membrane's pores. The volume of gel particles in the releasing bath is 1cm^3, and the volume of the releasing bath is 30 cm^3. The experimental condition of constant active substance concentration on the outer surface of the membrane is provided by constant steering of the releasing bath. Weight of gel particles is an important quantity for determination of the active substance loading coefficient (ratio of BSA mass and mass of gel particles).
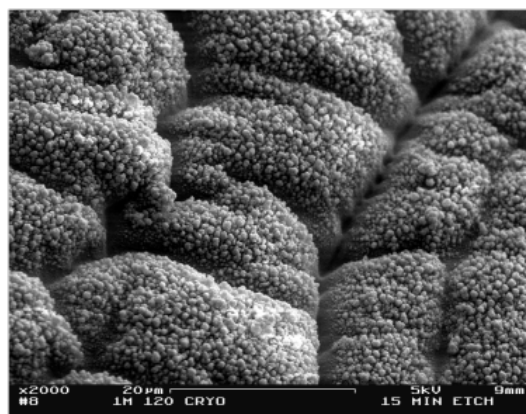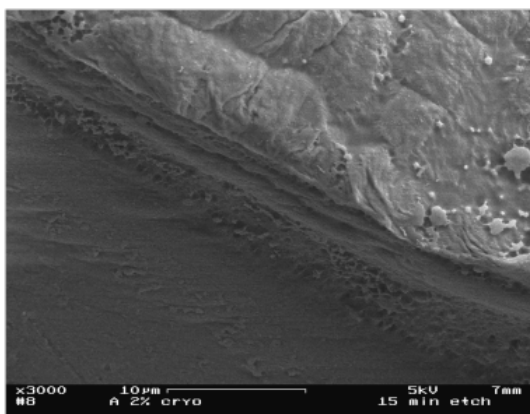
Fig.1. SEM on homogenous LF120M particles.   **Fig.2.** SEM on inhomogeneous LF120M particles

After putting the gel particles in the releasing medium, at the beginning on short time intervals and then on longer, 1 cm^3 of the releasing bath in which BSA is released is taken off and the same volume is replaced with pure releasing medium. The taken 1 cm^3 released volume is placed in CECIL series 2000 UV-Vis spectrophotometer to measure absorbance A at 280 nm, a wavelength at which BSA in phosphate buffer solution shows maximum absorption. The concentration of BSA is determined by the Lamber-Beer's law of light absorption. Before measuring the kinetics of controlled release of BSA, a calibration curve is constructed that represents the dependence of light absorbance at 280 nm of several BSA solutions with known concentrations c, $A = kdc$, where d is UV cell length and k is a calibration curve constant.

Scanning electron microscopy of gel particles is performed on the following way [5]. The particles were taken from water filled container for their transport and put on paper to wipe excess water from their surface. After that, the particles were put in nitrogen gas chamber and after that set in the preparation chamber at temperature – 110 ^{0}C. Here, gel particles were kept for 15 minutes for water sublimation from the gel. Six slices from center to the shell were cut from each particle on microtome machine and coated with 25 nm layer of Au/Pd. The slices

were investigated in Cryo FE-SEM, LEO Electron Microscopy, Germany) kept on -110 ^{0}C. Fig.1 and fig.2 presents two examples of SEM pictures from all nine investigated systems for visualizing differences between homogenous and inhomogeneous particles.

The size of microgel structures in the gelling solutions of the nine systems of CA gel particles was investigated by dynamic light scattering method [5,6]. The measure for the size is the characteristic correlation length ξ included in the Stokes-Einstein equation $D = kT/(6\pi\eta\xi)$, where η - dynamic viscosity of the gelling solution, k – Boltzmann's constant, T – temperature and D – coefficient of translational diffusion of the polymer chains in solution. The coefficient D is determined from the dynamic light scattering measurement of the autocorrelation function $G(\tau)$ that depends on the scattering wave vector $q = (4\pi/\lambda)\sin(\theta/2)$ and time τ of sampling intensity of the scattered light: $G(\tau) = 1 + e^{-2Dq^{2}\tau}$. The data for the characteristic length ξ is given on Table 1.

3. RESULT AND DISCUSSION

Figure 3 gives a graph of the measured kinetics of BSA controlled release for one of the nine systems. The other kinetics of release, are similar to the one given in fig.3. The results from the measuring kinetics of controlled release of BSA of the nine different gel particles systems are summarized in table 1. Fig.3 shows a percentage of released mass of BSA on the left ordinate m_t/m_0 %, where m_0 is the mass of BSA in the particles obtained after total disintegration of the particles, and m_t is mass of released BSA at any time during release. On the right ordinate, the releasing rate is given for the same system. In figure 3 (typical of all nine systems) is observable that BSA release starts with a burst effect.
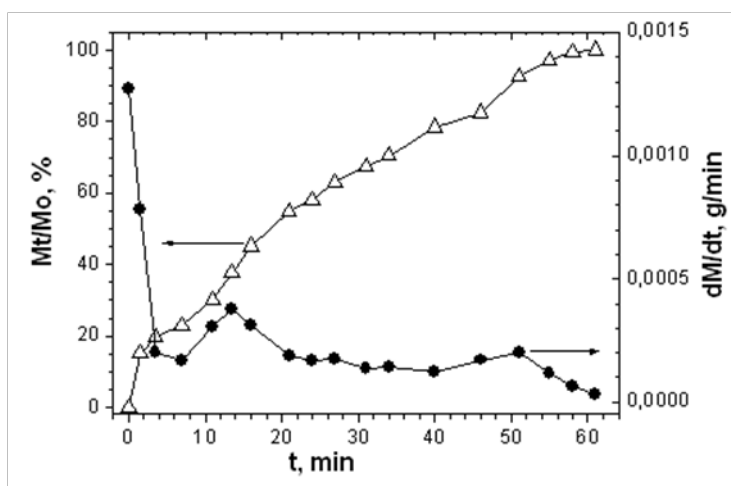
Fig.3. Release kinetics of BSA from CA system type LF240D (without added Ca^{2+} in gelling solution) at 37 ^{0}C.

The integral efficacy of controlled release is calculated by integration of release rate on time (upper boundary is end time of controlled release; lower boundary is time after end of the burst effect). The osmotic disintegration of gel particles is not pronounced equally for all systems. Time for start of osmotic disintegration effect at 37 ^{0}C for homogenous gel particles

without added $CaCl_2$ is: 52 minutes for system LF120M, 115 minutes for system LF200M, greater than 200 minutes for LF240D. The situation is different, for example, when added 10 mM $CaCl_2$. For those systems the time for start of osmotic disintegration effect is not much changed. Only for the system LF240D (with highest G/M ratio) and with added 10 mM $CaCl_2$, time for start of osmotic disintegration effect is much lower (16 minutes). From the three models of controlled release, we found that the osmotic pumping model is valid during all the time of controlled release. Taking the values of the thickness of chitosan membrane of all the particles measured on optical microscopy (22 ± 5) µm and thus knowing the surface area of the particles, BSA concentration in the particles C_a, and taking value 1 for the membrane's reflectivity, we calculated from Eq (4) the coefficient of the hydraulic permeability L_p and the values are given on Table 1 for the three gel systems. The existence of burst effect at the beginning of BSA release from the systems indicates on large concentration of BSA at the surface (membrane) of particles which is expectable to the reservoir model of release. Release profiles of the systems at the osmotic disintegration of particles are not sharp but times broaden, especially observed for inhomogeneous gels. This is an indication that the erosion model is taking place by the mechanism of gel's dissolution during BSA release.

Table.1. BSA release parameters in phosphate buffer solution at 37 0C for three types of CA systems.

	LF120M			LF200M			LF240D		
	0 mM	1 mM	10 mM	0 mM	1 mM	10 mM	0 mM	1 mM	10 mM
Release rate at controlled release stage, mg/min	0.05	0.05	0.12	0.01	0.16	0.09	0.05	0.19	0.27
Release rate at start time (with burst effect), mg/min	0.15	0.38	4.20	5.6	1.70	2.81	1.8	1.8	0.17
Release rate at 90 % release of BSA, mg/min	0.36	0.10	0.18	1.00	0.05	0	0.25	0.20	0.29
Time for release of 90 % BSA, min	58.5	25.5	45.0	119.0	72.5	92.0	25.5	29.0	27.0
Loading coefficient, %	1.0	1.7	2.6	3.3	1.9	1.7	`1.7	1.7	1.6
Loading efficacy	29.8	50.3	76.6	89.9	57.0	51.2	50.7	52.6	51.0
L_p, $m^3 \cdot s/kg$	4.9	1.8	1.6	0.3	5.1	1.9	-	6.7	6.0
Integral efficacy of release, %	29	18	30	3	35	27	0	31	32
Characteristic length ξ, µm	10.69	16.02	323.3	19.32	32.34	589.0	20.9	30.5	523.0

4. CONCLUSIONS

The research on the release properties of BSA from three types of calcium alginate particles with chitosan membrane, showed that the release rate increases with the increase of Ca^{2+} ions concentration in gelling solutions, i.e. by the increase of the inhomogeneity of the gel matrices reflected by the ξ parameter. The release profiles for all the systems showed flat release rate in a wider time domain. The release rates are higher for the system type LF240D

especially for the ones with added Ca^{2+} ions (inhomogeneous). Because of this, the time of 90 % release of BSA for this system is smaller than the other systems. From the analysis of the results, it can be concluded that CA gel particles with smaller G/M ratio showed optimal release properties expressed through high release rates, high time of 90 % release of BSA, optimal loading coefficient, high value of coefficient of the hydraulic permeability L_p, and optimal integral efficacy of release. We found that internal inhomogeneities of gel particles caused change in the structure of the gels that led to less pronounced controlled release properties.

REFERENCES

[1] Tanquary, A.C., Lacey, R.E., Introduction to Controlled Release. Plenum Press, New York (1974)

[2] Spencer, G., Wang, X., *Polymer*, **39**, 2759 (1998)

[3] Fan, L.T., Singh, S.K., Controlled Release: A Quantitative Treatment. Springer, Berlin (2011)

[4] Castilo, E., Ramirez, D., Casas, L., Lopez-Munguia, A., *J. Appl. Bioch. Biotech.*, **35**, 477 (1992)

[5] Rendevski, S., Ph.D. Thesis, University "Ss. Cyril and Methodius", PMF, Skopje (2004)

[6] Berne, B., Pecora, R., Dynamic Light Scattering, Dover Publications, New York (2000)

INTRODUCTION OF IMRT IN MACEDONIA: OPTIMIZING THE MLC PARAMETERS

D. Lukarski[1] and M. Ristova[2]

[1]*University Clinic for Radiotherapy and Oncology, Vodnjanska 17, 1000 Skopje, Macedonia*

[2] *Institute of Physics, Faculty of Mathematics and Natural Sciences, Arhimedova bb, 1000 Skopje, Macedonia*

Abstract. Intensity modulated radiotherapy (IMRT) for the Varian Eclipse Treatment Planning System (TPS) requires optimization of the values of two parameters of the Multi Leaf Collimator (MLC) – the transmission of the MLC and the so called Dosimetric Leaf Gap (DLG). This paper describes the optimization of those parameters for one of the linear accelerators at the University Clinic for Radiotherapy and Oncology in Skopje. The starting values for the MLC parameters were determined by dose measurements with ionization chambers. Those measured values were introduced in the TPS and an IMRT test plan was created. The acquired test plan was used for irradiation of the two-dimensional chamber array "MatriXX", and for comparison of the measured results with the corresponding results calculated by the TPS. By iteratively changing the two MLC parameters we optimized their values, so that the calculation corresponds to the measurement as much as possible. The final results of the optimization were introduced in the TPS thus enabling calculation of IMRT plans and proceed towards the phase of clinical introduction of this radiotherapy technique.

PACS: 87.53.Kn, 87.56.bd, 87.56.nk, 87.55.de

1. INTRODUCTION

The commissioning process of intensity modulated radiotherapy (IMRT) for clinical use is a multi stage process in which the performance of various parts of the system needs to be retested and optimized with more stringent tolerance levels. One of the parts of this system is the Treatment Planning System (TPS), which is used to calculate and optimize the beam directions and intensities in order to achieve the best coverage of the target volume with as much sparing of the surrounding healthy tissue as possible. At the University Clinic for Radiotherapy and Oncology in Skopje the TPS called Eclipse, manufactured by Varian Medical Systems, is used. In this TPS two parameters need to be introduced in order to be able to do treatment planning for IMRT – the transmission of the Multi Leaf Collimator (MLC) and the Dosimetric Leaf Gap (DLG) [1]. In this paper we present the results obtained during the commissioning process of this technique at the University Clinic for Radiotherapy and Oncology in Skopje, for one of the two available linear accelerators at that institution.

2. MATERIALS AND METHODS

The optimization of the two MLC parameters was performed in the following way. First the MLC transmission and the DLG were determined by measurements with ionization chambers. The values obtained were the starting values in the optimization process. Than a specific test plan was created in the TPS and a two dimensional chamber array, called "Matrixx" was irradiated with this test plan. Finally, by iteratively changing the two MLC parameters and recalculating the test plan, the closest agreement between the calculated and the measured two dimensional dose distributions was found.

The MLC transmission was measured by a plane parallel ionization chamber (PPC40) in a plastic (PMMA) phantom. The transmission is the ratio of the measured value with closed and open MLC, for a certain measuring conditions (energy, field size, measurement depth, source to phantom distance, position of the leaf ends). These results are already published [2] and here we will only state that the mean transmission for the 6 MV beam was found to be 1,6%, and for the 15 MV beam, 1,7%.

The DLG is a parameter that accounts for the transmission through the rounded ends of the MLC leafs [1]. In order to determine the value of this parameter, 4 dynamic test fields were created and measured with ionization chamber in air, at source to chamber distance of 100 cm. In each of these fields a leaf gap of certain width was sweeping through the field with speed 1 cm/s from left to right. In the four fields the widths of the gaps were 20 mm, 10 mm, 4 mm and 1 mm. A fifth measurement, with closed MLC leafs, was performed, in order to correct the measurements for the MLC transmission. A linear extrapolation of the corrected values was performed, in order to obtain the field width for which the corrected reading of the ionization chamber would be zero. Thus obtained field width is the required parameter DLG.
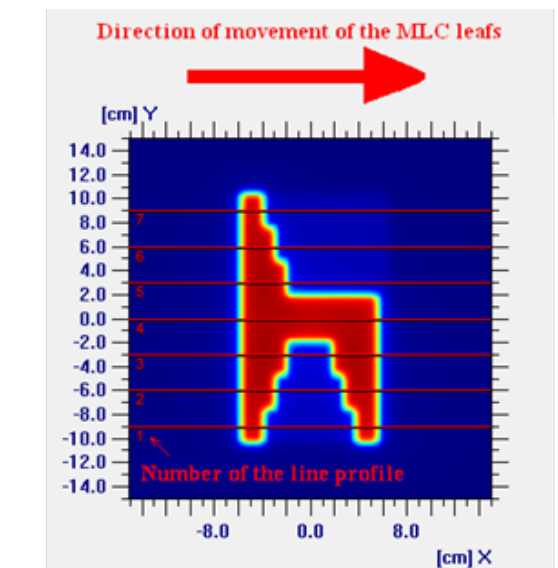

Fig.1: Chair test – the red horizontal lines are the line profiles that are evaluated.

In order to optimize the values of the two parameters, a specific test plan, "Chair", was created in the TPS [3] and with this plan the two dimensional chamber array "Matrixx" was irradiated. In this plan the MLC leafs move from left to right with such speeds that an integral intensity pattern shown on Figure 1 is created. The pattern can be divided in three regions. In the upper region, characterized by the line profiles 5, 6 and 7, the zero intensity region on the right of the back of the chair (the blue region on the right of the red region) is comprised exclusively from the transmission through the MLC leafs. In the region in the middle, characterized by the line profile 4, the movement of the MLC leafs is such that a large region of homogeneous intensity is created (red region), so that absolute dosimetry verification can be performed. In the lower region, characterized by the line profiles 1, 2 and 3, the movements of the leafs are such that between the legs of the chair (the blue region between the two red regions) they are forced to move with maximal speed and minimal opening width, regardless of the MLC parameters entered in the TPS. With this test plan the two dimensional chamber array "Matrixx" was irradiated and the measured dose profiles were influenced only by the behavior of the MLC itself, and not by the MLC parameters that were used by the TPS. In this way, using the upper region, the MLC transmission parameter was optimized and using the lower region, the DLG parameter was optimized.

3. RESULTS

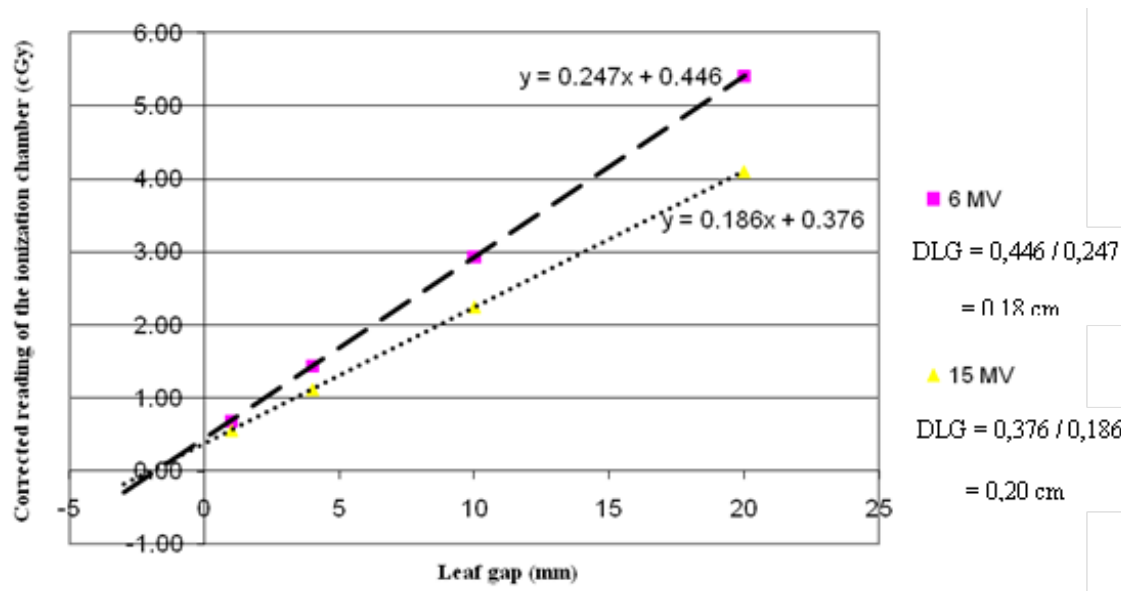On Figure 2, the results from the measurement of the DLG parameter are given.

Fig.2: Determination of the DLG parameter for the measured values with the ionization chamber.

Based on these results, for the DLG parameters the starting values in the process of the optimization were 0,18 cm for the 6 MV beam and 0,2 cm for the 15 MV beam.

As stated before, for the MLC transmission parameter, the starting values in the process of the optimization were 1,6% for the 6 MV beam, and 1,7% for the 15 MV beam.

The optimization was performed by an iterative procedure consisting of changing the two MLC parameters, recalculating the test plan and then comparing and visually evaluating the agreement between the calculated and the measured profiles. The evaluation was performed on three different clinically significant depths in water (we used RW3 solid water slabs placed on top of the "Matrixx") – 3 cm, 5 cm and 10 cm. The optimization was finished when the closest agreement between the calculated and the measured two dimensional dose distributions was achieved. The final values after the optimization are given in Table 1.

Table 1: Final values of the MLC transmission and DLG parameters after the optimization.

Beam quality	MLC transmission (%)	DLG (cm)
6 MV	1,7	0,18
15 MV	2,1	0,20

On figure 3 a comparison of the profile number 1 is given for 6 MV for depth of 3 cm water. On the left side, the comparison of the measured and calculated profile before the optimization is given and on the right side the comparison of the measured and calculated profile after the optimization is given. The part of the profile that is of interest is marked with the arrows. From this figure we can see the improvement in the correspondence of the calculation to the measurement based on the optimization of the value for the DLG parameter.

Fig.3: Profile 1 from the "Chair" test for 6 MV for depth 3 cm – a) before optimization, b) after optimisation.

On figure 4 a comparison of the profile number 7 is given for 15 MV for depth of 5 cm water. On the left side, the comparison of the measured and calculated profile before the optimization is given and on the right side the comparison of the measured and calculated profile after the optimization is given. The part of the profile that is of interest is marked with the arrows. From this figure we can see the improvement in the correspondence of the

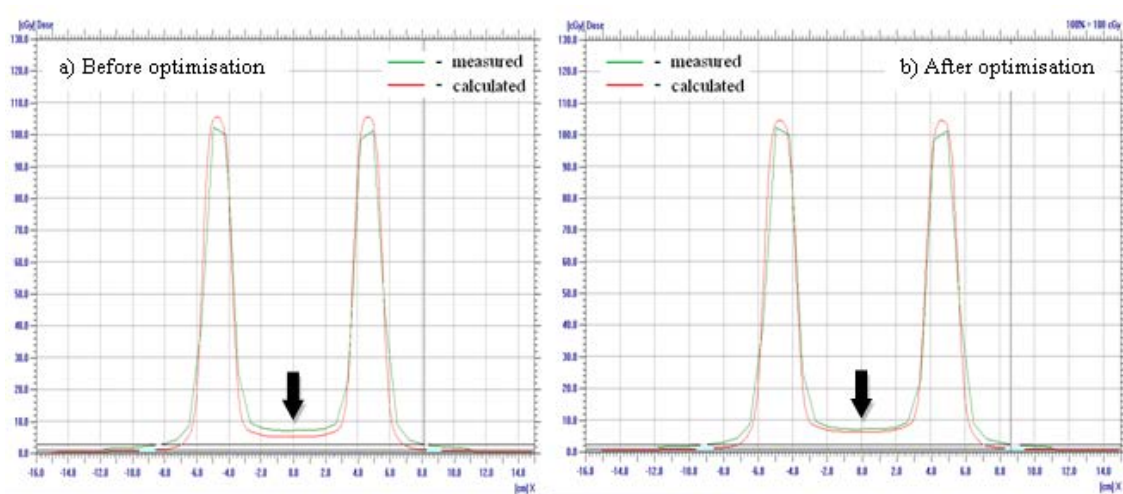calculation to the measurement based on the optimization of the value for the MLC transmission parameter.
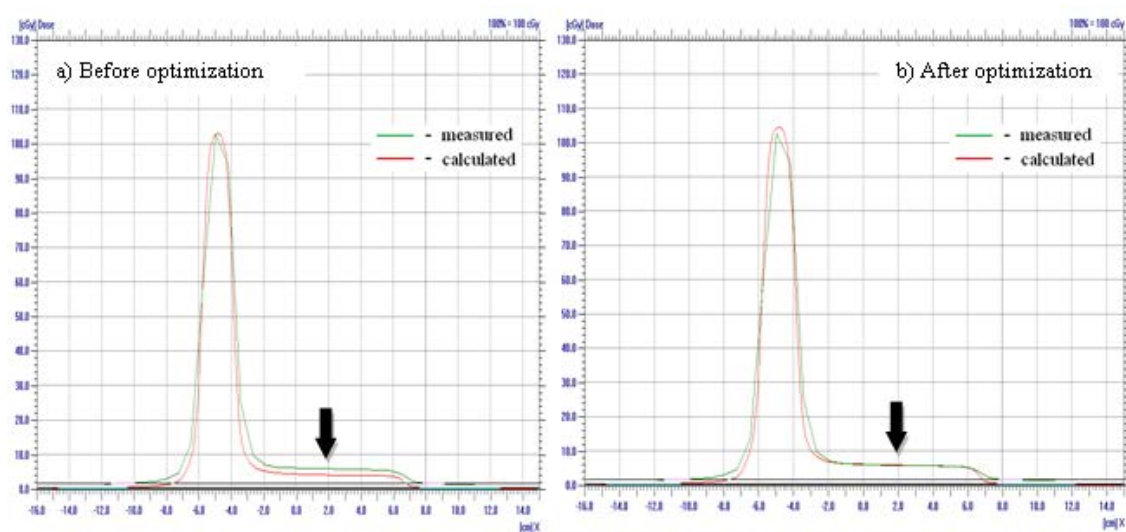
Fig.4: Profile 7 from the "Chair" test for 15 MV for depth 5 cm in water – a) before optimization and

b) after optimization.

3. CONCLUSIONS

In the process of commissioning of IMRT one of the most important parts of the process is the commissioning of the TPS. In this paper we presented the determination of the MLC parameters required by the TPS, in order to be able to perform the process of treatment planning. We determined these parameters by a process of iterative optimization which resulted in a greater correspondence of the calculated dose distributions with the ones that were measured. These optimized values of the MLC parameters will enable more accurate calculation of the IMRT treatment plans, with greater correspondence between the desired dose and the dose actually delivered to the patient, thus enabling better coverage of the target volumes and reduced dose to the surrounding healthy tissues, which in turn will improve the probability of the desired treatment outcome for the patient.

REFERENCES

[1] Varian Medical Systems, "Eclipse Algorithms Reference Guide", P/N B500298R01B, November 2006.
[2] Д. Лукарски, С. Петковска, Зборник на трудови од Првата македонска конференција за медицинска физика и биомедицински инженеринг, Скопје, Р. Македонија, p 47-52, (2007).
[3] Van Esch A et al., Radiother. Oncol. Vol. 65, p.53 (2002).

HARMONIC OSCILLATOR DRIVEN BY GENERALIZED NOISES: OVERDAMPED BEHAVIOR

T. Sandev[1]

[1]*Radiation Safety Directorate, Partizanski odredi 143, PO Box 22, 1020 Skopje, Macedonia*

Abstract. An analytical treatment of a generalized Langevin equation for a harmonic oscillator driven by generalized noises is presented. The overdamped limit (cases of high viscous damping) as a model of conformational dynamics of proteins is considered. The behavior of the oscillator is analyzed by calculation of the mean square displacement and normalized displacement correlation function. The results are expressed in terms of Mittag-Leffler type functions. Standard Brownian motion is a special case of the considered model. It is shown a good agreement with some experimental results.

PACS: 02.50.−r, 05.40.−a, 05.10.Gg, 05.40.Ca

1. INTRODUCTION

The standard Brownian motion, which represents a random process driven by Gaussian white noise, can be analyzed either by standard diffusion equation for the probability distribution function or by stochastic Langevin equation for a Markov process, where the consecutive displacements are independent. Analysis lead to Gaussian form of the probability distribution function $u(x,t) = (1/\sqrt{4\pi K_1 t})\exp(-x^2/4K_1 t)$, where K_1 is the diffusion coefficient of dimension $[K_1] = \mathrm{m}^2/\mathrm{s}$, and linear dependence of the mean square displacement (MSD) on time, i.e. $\langle x^2(t) \rangle = 2K_1 t$. Normal diffusion appears when the microscopic time scale is short comparing with the observation time. Contrary, one may observe deviations from Brownian diffusion. Thus, MSD has a power law dependence on time $\langle x^2(t) \rangle = 2K_\alpha t^\alpha / \Gamma(1+\alpha)$ [1], where K_α is the generalized diffusion coefficient of dimension $[K_\alpha] = \mathrm{m}^2/\mathrm{s}^\alpha$, and α is the anomalous diffusion exponent. Such diffusion is the so-called anomalous diffusion (subdiffusion if $0 < \alpha < 1$ and superdiffusion if $1 < \alpha$), which is a characteristic for non-Markovian processes, and can be observed in different systems [1-4]. This means that the evolution of the system in a given moment of time t depends on the past; the time domain of the memory is long comparing with the characteristic time scale of the motion. Anomalous diffusion can be studied either by fractional differential equations for the probability distribution function [1,5,6] or by stochastic equations, such as the generalized Langevin equation (GLE). GLE for a particle of mass in a given potential $V(x)$ is given by [7]:

$$m\ddot{x}(t) + \int_0^t \gamma(t-t')\dot{x}(t)dt' + \frac{dV(x(t))}{dx} = \xi(t),$$

$$\dot{x}(t) = v(t), \tag{1}$$

where $x(t)$ is the particle displacement, $v(t)$ is the particle velocity, $F(x) = -dV(x(t))/dx$ is the external force acting on the particle due to the potential $V(x)$, $\gamma(t)$ is the frictional memory kernel, and $\xi(t)$ is a stationary random force with a zero mean $\langle \xi(t) \rangle = 0$. Its correlation is given by:

$$\langle \xi(t)\xi(t') \rangle = C(t'-t). \tag{2}$$

The notation $\langle \cdot \rangle$ means an ensemble averages, i.e. statistical averaging over an ensemble of particles at a given moment of time *t*. In case when fluctuation and dissipation come from same source then correlation (2) is related with $\gamma(t)$ via the second fluctuation-dissipation theorem [7]:

$$C(t) = k_B T \gamma(t) \tag{3}$$

where k_B is the Boltzmann constant and T is the absolute temperature of the environment in which the particle is immersed. Otherwise, relation (3) does not hold. GLE (1) can be derived from the Hamiltonian representing the physical microscopic interactions between the particle and the surrounding complex environment [7].

The case of large friction (high damping) in GLE (1) usually is analyzed to model experimental data related to the movements within proteins. Large friction means that the acceleration of the particle $\ddot{x}(t)$ is negligible. Due to the liquid environment of proteins frictional term usually is very high, so the overdamped behavior of the particle is of importance [2,8,9]. When the movement is confined to a short range, which is a case for movement within proteins, the potential function can be well approximated by a harmonic potential $V(x) = m\omega^2 x^2 / 2$, where ω is the oscillator frequency. Thus, GLE (1) in which appears a term of form $m\omega^2 x(t)$ represents a suitable model of anomalous dynamics within proteins [2,8,9].

Different frictional memory kernels $\gamma(t)$ have been introduced. In [10] we introduced an internal noise with correlation of form:

$$C(t) = \frac{C_{\alpha,\beta,\delta}}{\tau^{\alpha\delta}} t^{\beta-1} E_{\alpha,\beta}^{\delta}\left(-\frac{t^\alpha}{\tau^\alpha}\right), \tag{4}$$

where τ is the characteristic memory time, $C_{\alpha,\beta,\delta}$ is a coefficient independent on time and which may depends on $\alpha > 0$, $\beta > 0$, $\delta > 0$. Here $E_{\alpha,\beta}^{\delta}(\cdot)$ is the three parameter Mittag-Leffler (M-L) function $E_{\alpha,\beta}^{\delta}(z) = \sum_{k=0}^{\infty} (\delta)_k / \Gamma(\alpha k + \beta) \cdot z^k / k!$, $(\beta, \delta, z \in \mathbb{C}, \Re(\alpha) > 0)$, $(\delta)_k$ is the Pochhammer symbol, $(\delta)_0 = 1$, $(\delta)_k = \Gamma(\delta + k) / \Gamma(\delta)$.

For $\delta = 1$ it becomes a two parameter M-L function $E_{\alpha,\beta}^{1}(z) = E_{\alpha.\beta}(z)$ and for $\beta = \delta = 1$ – one parameter M-L function $E_{\alpha,1}^{1}(z) = E_{\alpha}(z)$. By using asymptotic expansion formula [12], $E_{\alpha,\beta}^{\delta}(z) = (-z)^{\delta} / \Gamma(\delta) \sum_{k=0}^{\infty} \Gamma(\delta+k) / \Gamma(\beta - \alpha(\delta+k)) \cdot (-z)^{-k} / k!$, $|z| > 1$, for large values of z, it can be shown that $\gamma(t)$ satisfies $\lim_{t \to \infty} \gamma(t) = \lim_{t \to \infty} s\hat{\gamma}(s) = 0$ [10], where $\hat{\gamma}(s) = L[\gamma(t)] = \gamma_{\alpha,\beta,\delta} s^{\alpha\delta - \beta} / (s^{\alpha} + \tau^{-\alpha})^{\delta}$ is the Laplace transform of $\gamma(t)$, $\gamma_{\alpha,\beta,\delta} = C_{\alpha,\beta,\delta} / k_B T \tau^{\alpha\delta}$ [10]. The case $\tau \to 0$, $\alpha \neq 1$, $\beta = \delta = 1$ yields the power law frictional memory kernel $C(t) = C_{\alpha} t^{-\alpha} / \Gamma(1-\alpha)$, which has been used to model anomalous diffusive processes [13-15]. Note that the standard Brownian motion is a special case of the considered problem and can be obtained in case when $\alpha = \beta = \delta = 1$ and $\tau \to 0$ (noise term becomes the Dirac delta or white noise). In [10,16-19] M-L frictional memory kernels were used as generalizations of the one of power law form. In [19-21] fractional GLEs with different noise terms were analyzed and used for modeling generalized diffusive processes.

This paper is organized as follows. In section 2 formal solution of the GLE is given. The asymptotic behavior of the oscillator in the long time limit is analyzed. Exact results for the MSD, and normalized displacement correlation function in case of generalized internal noises, in the overdamped limit, are derived. Some possible applications of the considered model are discussed. Conclusions are given in section 3.

2. GLE FOR A HARMONIC OSCILLATOR. SOLUTION AND RESULTS

Let us solve the GLE (1) for a harmonic oscillator. By Laplace transform one obtains:

$$\hat{X}(s) = x_0 \left[s^{-1} - \omega^2 \hat{I}(s) \right] + \left[v_0 + \frac{1}{m} \hat{F}(s) \right] G(s) \tag{5}$$

$$\hat{V}(s) = \left[v_0 + \frac{1}{m} \hat{F}(s) \right] \hat{g}(s) - \omega^2 x_0 \hat{G}(s) \tag{6}$$

where $\hat{X}(s) = L[x(t)]$, $\hat{V}(s) = L[v(t)]$, $x_0 = x(0)$ and $v_0 = v(0)$ are initial particle displacement and initial particle velocity, respectively, $\hat{F}(s) = L[\xi(t)]$,

$$\hat{I}(s) = \frac{s^{-1}}{s^2 + s\hat{\gamma}(s)/m + \omega^2}, \tag{7}$$

$\hat{G}(s) = s\hat{I}(s)$, $\hat{g}(s) = s\hat{G}(s)$. The inverse Laplace transform of relations (5) and (6) yields:

$$x(t) = x_0 \left[1 - \omega^2 I(t) \right] + v_0 G(t) + \frac{1}{m} \int_0^t G(t-t') \xi(t') dt' =$$

$$= \langle x(t) \rangle + \frac{1}{m} \int_0^t G(t-t') \xi(t') dt'. \tag{8}$$

$$v(t) = v_0 g(t) - \omega^2 x_0 G(t) + \frac{1}{m} \int_0^t g(t-t') \xi(t') dt' =$$

$$= \langle v(t) \rangle + \frac{1}{m} \int_0^t g(t-t') \xi(t') dt' \qquad (9)$$

where $\langle x(t) \rangle = x_0 [1 - \omega^2 I(t)] + v_0 G(t)$, $\langle v(t) \rangle = v_0 g(t) - \omega^2 x_0 G(t)$ are mean particle displacement and mean particle velocity, respectively, and $I(t) = L^{-1}[\hat{I}(s)]$, $G(t) = L^{-1}[\hat{G}(s)]$ and $g(t) = L^{-1}[\hat{g}(s)]$ are the so-called relaxation functions. They are related to the MSD $\langle x^2(t) \rangle$, time-dependent diffusion coefficient $D(t) = (1/2) d\langle x^2(t) \rangle/dt$, velocity autocorrelation function (VACF) $C_V(t) = \langle v(t) v(0) \rangle / \langle v^2(0) \rangle$. In the long time limit ($t \to \infty$), one obtains $\langle x^2(t) \rangle = (2k_B T/m) I(t)$, $D(t) = (k_B T/m) G(t)$ and $C_V(t) = g(t)$ [14,16,17].

2.1. Asymptotic behavior

Sometimes, finding the relaxation functions is very complicated problem. Since we are interested to analyze the anomalous diffusive behavior of the oscillator, we investigate the asymptotic behavior of relaxation functions in the long time limit by using Tauberian theorem [22]. It stands that if the asymptotic behavior of a given non negative and monotone function $r(t)$ for $t \to \infty$ is $r(t) \simeq t^{-\alpha}$, then its corresponding Laplace transform pair $\hat{r}(s) = L[r(t)]$, has the behavior $\hat{r}(s) \simeq \Gamma(1-\alpha) s^{\alpha-1}$, for $s \to 0$. Thus, for $\beta - 1 < \alpha\delta < \beta + 1$, it is obtained:

$$I(t) = \sum_{k=0}^{\infty} \left(-\omega^2 \right)^k t^{2k+2} E_{2-(1+\alpha\delta-\beta),2k+3}^{k+1} \left(-\frac{C_{\alpha,\beta,\delta}}{k_B T m} t^{2-(1+\alpha\delta-\beta)} \right)$$

$$\simeq \frac{k_B T m}{C_{\alpha,\beta,\delta}} t^{1+\alpha\delta-\beta} E_{1+\alpha\delta-\beta,2+\alpha\delta-\beta} \left(-\frac{k_B T m \omega^2}{C_{\alpha,\beta,\delta}} t^{1+\alpha\delta-\beta} \right) \quad \text{for} \quad t \to \infty. \qquad (10)$$

By using $E_{\alpha,\beta}(z) = z E_{\alpha,\alpha+\beta}(z) + 1/\Gamma(\beta)$, relaxation function (10) yields the MSD:

$$\langle x^2(t) \rangle = \frac{2k_B T}{m\omega^2} \left[1 - E_{1+\alpha\delta-\beta} \left(-\frac{k_B T m \omega^2}{C_{\alpha,\beta,\delta}} t^{1+\alpha\delta-\beta} \right) \right], \qquad (11)$$

from where we find $D(t)$ and $C_V(t)$. Relation (11) turns to $\langle x^2(t) \rangle \simeq t^{1+\alpha\delta-\beta}/\Gamma(2+\alpha\delta-\beta)$ in case of a free particle ($V(x) = 0$) [10], from where one concludes that anomalous diffusion occurs (subdiffusion if $\beta - 1 < \alpha\delta < \beta$ and superdiffusion if $\beta < \alpha\delta < \beta + 1$). Relation (11) gives the equilibrium value $\langle x^2(t) \rangle_{t\to\infty} = 2k_B T/m\omega^2$. Note that relation (10) is the exact expression for the case $\tau \to 0$. The result for $C_V(t) \simeq t^{\alpha\delta-\beta-1}/\Gamma(\alpha\delta - \beta)$ can be used, for example, in the description of experimental data for VACF in the motion of atoms in liquid argon [23]. For $\alpha = \beta = \delta = 1$ it is obtained the result for the standard Brownian motion, i.e. a linear dependence of the MSD on time.

2.2. High viscous damping

Next we investigate the behavior of oscillator in case of high friction. Neglecting the inertial term, by applying an inverse Laplace transform [24] of relation (7), relaxation function becomes:

$$I_0(t) = L^{-1}\left[\frac{s^{-1}}{s\hat{\gamma}(s)/m + \omega^2}\right] = \frac{1}{\omega^2}\sum_{k=0}^{\infty}\left(-\frac{\gamma_{\alpha,\beta,\delta}}{m\omega^2}\right)^k t^{(\beta-1)k} E_{\alpha,(\beta-1)k+1}^{\delta k}\left(-\frac{t^\alpha}{\tau^\alpha}\right). \tag{12}$$

From the asymptotic expansion formula for the three parameter M-L function, $I_0(t)$ becomes:

$$\begin{aligned}I_0(t) &= \frac{k_B T m}{C_{\alpha,\beta,\delta}} t^{1+\alpha\delta-\beta} E_{1+\alpha\delta-\beta,2+\alpha\delta-\beta}\left(-\frac{k_B T m\omega^2}{C_{\alpha,\beta,\delta}} t^{1+\alpha\delta-\beta}\right) = \\ &= \frac{1}{\omega^2}\left[1 - E_{1+\alpha\delta-\beta}\left(-\frac{k_B T m\omega^2}{C_{\alpha,\beta,\delta}} t^{1+\alpha\delta-\beta}\right)\right],\end{aligned} \tag{13}$$

in the long time limit. Thus, MSD has the form (11). Thus, the anomalous diffusive behavior of the oscillator may be investigated by considering high viscous damping, instead of the GLE (1).

2.3. Results and discussion

Let us now consider the following initial conditions: $\langle x_0^2\rangle = k_B T/m\omega^2$, $\langle x_0 v_0\rangle = 0$, $\langle \xi(t)x_0\rangle = 0$ [15]. Thus, for the normalized displacement correlation function given by $C_X(t) = \langle x(t)x_0\rangle/\langle x_0^2\rangle$, which is an experimentally measured quantity, one obtains:

$$C_X(t) = L^{-1}\left[\frac{1}{s} - \frac{\omega^2 s^{-1}}{s\hat{\gamma}(s)/m + \omega^2}\right] = 1 - \omega^2 I_0(t) \tag{14}$$

where $I_0(t)$ is given by (13). For $\tau \to 0$ it follows $C_X(t) = E_{1+\alpha\delta-\beta}\left(-(k_B T m\omega^2/C_{\alpha,\beta,\delta})t^{1+\alpha\delta-\beta}\right)$, which is in agreement with experimental results for the fluctuations of the distance between fluorescein-tyrosine pair within a single protein [9].

Let us further analyze obtained results. Firstly, note that relaxation function (12) is represented in terms of infinite series of three parameter M-L functions. The long time limit yields relation (11) which is represented by one parameter M-L function. It is known that $f(t) = E_\alpha(-t^\alpha)$ is a completely monotone function for $0 < \alpha < 1$ [25], i.e. $(-1)^n f^{(n)}(t) \ge 0$ for all $t > 0$ and all $n = 0, 1, 2, \ldots$ The case $1 < \alpha$ may show interesting oscillation-like behavior. By taking constants that appear in relation (11) equal to one and by using $\omega = 1$, the MSD (11) is completely monotone for $0 < 1 + \alpha\delta - \beta < 1$. From Fig. 1(a) ($\omega = 1$) we see that for $\alpha = 3/2$, $\beta = 1$, $\delta = 1/2$ (solid line), and $\alpha = 1/2$, $\beta = 7/16$, $\delta = 3/4$ (dashed line), MSD has

monotonic behavior since $0 < 1 + \alpha\delta - \beta < 1$. For $\alpha = 5/4$, $\beta = 1/2$, $\delta = 1$ (dot-dashed line), and $\alpha = 3/4$, $\beta = 1/4$, $\delta = 1$ (dotted line), MSD shows oscillation-like behavior since $1 + \alpha\delta - \beta > 1$. In Fig. 1(b) graphical representation of $C_X(t) = 1 - \omega^2 I(t)$, where $I(t)$ is given by (10), for $\alpha = 1/2$, $\beta = 7/16$, $\delta = 3/4$, is presented. We see that for $\omega = 0.3$ (solid line), $C_X(t)$ has monotonic decay and does not cross the zero line. For $\omega = 3$ (dashed line) and $\omega = 1$ (dot-dashed line), $C_X(t)$ crosses the zero line and it has oscillation-like behavior. For $\omega = 0.74$ (dotted line), $C_X(t)$ has non monotonic decay. It approaches the zero line but does not cross it. These results are different than the ones for a classical damped oscillator, where only two types of motion may appear: overdamped motion when $\langle x(t) \rangle > 0$ for any time t when $\langle x_0 \rangle > 0$ and there are no oscillations, and underdamped motion when $\langle x(t) \rangle$ crosses the zero line and oscillates [15]. The frequency on which transition from overdamped to underdamped motion appears is so-called critical frequency. Here, in the considered GLE, there are additional definitions of critical frequencies [15] on which the oscillator changes its behavior, for example from monotonic to non monotonic decay of $C_X(t)$ without crossings of the zero line. They depend on parameters of the frictional memory kernel and their estimation is a nontrivial problem [15]. Such oscillations, as shown in Fig. 1(b), were observed in the molecular dynamic simulations of fluctuations of donor-acceptor distance for a single protein [26]. Furthermore, such oscillations and power law decay of the distance between fluorescein-tyrosine pair within a single protein have been observed experimentally [9].

3. CONCLUSIONS

It is shown that the GLE for a harmonic oscillator is a suitable model for anomalous dynamics within proteins. It is shown that the case of high friction, which is simpler, can be used for analyzing the anomalous diffusive behavior instead of the GLE (1). The obtained analytical results for the MSD and normalized displacement correlation function are in good agreement with some known experimental observations.
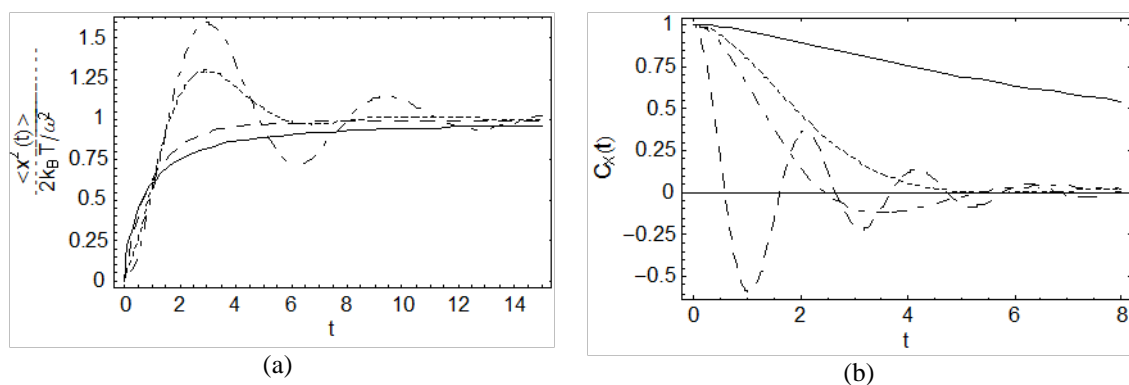

(a)   (b)

Fig. 1: Graphical representation of: (a) MSD; (b) $C_X(t)$.

REFERENCES

[1] R. Metzler and J. Klafter, Phys. Rep. **339**, 1 (2000)

[2] S.C. Kou and X.S. Xie, Phys. Rev. Lett. **93**, 180603 (2004)

[3] J . Tang, R.A. Marcus, Phys. Rev. Lett. **95**, 107401 (2005)

[4] S.C.Weber, A.J. Spakowitz, and J.A. Theriot, Phys. Rev. Lett. **104**, 238102 (2010)

[5] T. Sandev, R. Metzler and Z. Tomovski, J. Phys. A: Math. Theor. **44**, 255203 (2011)

[6] Z. Tomovski, T. Sandev, R. Metzler and J. Dubbeldam, Physica A **391**, 2527 (2012)

[7] R. Zwanzig, Nonequilibrium Statistical Mechanics, Oxford Univ. Press, New York, 2001.

[8] S.C. Kou, The Annals of Applied Statistics **2**, 501 (2008)

[9] W. Min et al., Phys. Rev. Lett. **94**, 198302 (2005)

[10] T. Sandev, Ž. Tomovski, and J.L.A. Dubbeldam, Physica A **390**, 3627 (2011)

[11] T.R. Prabhakar, Yokohama Math. J. **19**, 7 (1971)

[12] R.K. Saxena, A.M. Mathai, and H.J. Haubold, Astrophys. Space Sci. **209**, 299 (2004)

[13] E. Lutz, Phys. Rev. E **64**, 051106 (2001)

[14] F. Mainardi and P. Pironi, Extracta Math. **10**, 140 (1996)

[15] S. Burov and E. Barkai, Phys. Rev. E **78**, 031112 (2008)

[16] A.D. Viñales and M.A.. Despósito, Phys. Rev. E **75**, 042102 (2007)

[17] A.D. Viñales, K.G. Wang, and M.A.. Despósito, Phys. Rev. E **80**, 011101 (2009)

[18] T. Sandev and Ž. Tomovski, Phys. Scr. **82**, 065001 (2010)

[19] T. Sandev, R. Metzler, and Ž. Tomovski, Fract. Calc. Appl. Anal. **15**, 426 (2012)

[20] C.H. Eab and S.C. Lim, Physica A **389**, 2510 (2010)

[21] S.C. Lim and L.P. Teo, J. Stat. Mech. P08015 (2009)

[22] R. Gorenflo and F. Mainardi, J. Phys.: Conf. Ser. **7**, 1 (2005)

[23] A. Rahman, Phys. Rev. **136**, A405 (1964)

[24] Ž. Tomovski, R. Hilfer, and H.M. Srivastava, Integral Transform. Spec. Funct. **21**, 797 (2010)

[25] E. Capelas de Oliveira, F. Mainardi, and J. Vaz Jr., Eur. Phys. J. Spec. Top. **193**, 161 (2011)

[26] G. Luo et al., J. Phys. Chem. B **110**, 9363(2006)

ХАРМОНИСКИ ОСЦИЛАТОР ДВИЖЕН СО ГЕНЕРАЛИЗИРАНИ ШУМОВИ: ПОВЕДЕНИЕ ПРИ СИЛНО ТРИЕЊЕ

Т. Сандев[1]

[1]*Дирекција за радијациона сигурност, Партизански одреди 143, ПФах 22, 1020 Скопје, Република Македонија*

Апстракт. Презентиран е аналитички третман на генерализирана равенка на Ланжевен за хармониски осцилатор движен со генерализирани шумови. Разгледан е случајот на силно вискозно триење како модел за конформациона динамика на протеини. Поведението на осцилаторот е анализирано со пресметување на средното квадратно поместување и нормираната корелациона функција на поместувањето. Резултатите се претставени со помош на функциите на Митаг-Лефлер. Стандардното Брауново движење претставува специјален случај на разгледаниот модел. Покажана е добра согласност со некои експериментални резултати.

CHANGE IN GELLATION TIME OF SODIUM ALGINATE BIOPOLYMER HYDROGELS WITH CHANGE OF DOSE OF GAMMA IRRADIATION

R. Popeski-Dimovski[1], S. Rendevski[2] and N. Mahmudi[3]

[1]Faculty of Natural Sciences and Mathematics, University "Ss. Cyril and Methodius", Gazi Baba, b.b., 1000 Skopje, Republic of Macedonia

[2] Faculty of Electrical Engineering, University "Goce Delcev", Krste Misirkov, b.b., 2000 Stip, Republic of Macedonia

[2] Faculty of Natural Sciences and Mathematics, State University of Tetovo, bul. Ilinden, b.b., 1200 Tetovo, Republic of Macedonia

Abstract: Gamma irradiation induces many changes in the polymers and with that most of the properties of polymer gels. In this research we observed changes in gellation time of sodium alginate with changes in absorbed dose of gamma irradiation by measuring gel's viscosity from the start of gellation (activation of the gel forming component) to the end of gellation (maximum viscosity). Prior to gellation, the sodium alginate powder samples were gamma irradiated by exposing it to five different absorbing doses (nonirradiated, 2.5 kGy, 5 kGy, 10 kGy, 15 kGy). We used sodium alginate with $\overline{M}_w$ of $670 \cdot 10^3$ g/mol and G/M ratio of 70/30. $CaCO_3$ served as a source of Ca^{2+} ions for ionic (physical) cross-linking of the alginate and GDL as a week acid for activation of Ca^{2+} ions. We found that the gellation time is in linear proportion to the absorbed dose of gamma irradiation of the sodium alginate polymer.

PACS: 61.80.Ed, 83.80.Rs, 83.80.Kn

1. INTRODUCTION

γ-Rays, with its high energy, impact and cut the polymer chains. Depending from the radiation flux and time and from there the absorbed dose there can be two results. In the first case when we have low dose the polymer chains cut and reconnect whit a gellation effect on the polymer. In the second case when we have higher dose the polymer chains are cut in many places and this process is not followed with reconnection that leads to degradation of the gel. Splicing of the chain and degradation is followed with decrease of the molar weight of the polymer and with that a change in the mechanical and bioadhesive properties [1-3]. Here we used low doses of up to 10kGy and trough compressibility tests we followed the degradation of the polymer gels. [4,5]. The average molecular weight between crosslink points in the gel M_c is connected to the number of crosslink points in unit volume. So if a γ quant enters this volume and cuts one covalent bond in the same time it can come to formation of two new crosslink

points increasing its number or a connection of two free chains reducing the number of crosslink points. In this way through the connection of M_c with the density of gel and elastic modulus we can follow the interaction of γ-rays with the gel network pic. 1.

Alginate is natural occurring polysaccharide found in substantial amounts in brown seaweeds. They are unbranched binary co-polymers of (1–4)-linked residues of b-D-mannuronic acid (M) and a-L guluronic acids (G). Alginic acid and its water-soluble sodium salt have a great ability to give highly viscous solutions even at moderate concentrations. Aqueous solution of sodium alginate forms stable gels in the presence of multivalent cations such as Ca^{2+} and Mg^{2+}. Gel formation occurs due to the ionic interaction between guluronic acid residues from two or more alginate chains and cations, yielding a three-dimensional network of alginate molecules well described by the ''egg-box [6]. Functional and physical properties, mechanical strength, porosity, gel uniformity, biocompatibility, and influence on encapsulated cells properties of alginate gels vary widely depending on ratio of mannuronic to guluronic acids, the frequency and size of guluronic acid blocks and the molecular weight of the polymer [7,8].

Currently Ca^{2+} is preferred to crosslink alginate for biomedical applications because of the mild reaction conditions compared for example to the cellular toxicity of both Ba^{2+} and Sr^{2+} [9,10]. Two methods of gellation have been extensively described and used to create alginate hydrogels: diffusion gelling and in-situ gelling. Diffusion gelling is an ideal approach that is widely used for rapidly encapsulating cells and substances in microspheres of alginate used for controlled released methods where polymer gels swell in a medium in order to release a given substance. In this method calcium ions diffuse through the liquid alginate boundary, cross-linking alginate strands as the ions move through the volume of the alginate solutions. However, cross-links are not uniformly distributed throughout the gel that has a great influence on the properties of the gel including its swelling time. [11,12] . On the other hand, in recent years there has been a very big interest in the preparation of homogeneous alginate gels in different forms by using in-situ gelling methods. In this method $CaCO_3$ is mixed with alginate to create a homogeneous mixture. D-Glucono-d-lactone (GDL) is added to acidify the solution and release calcium ions, making them available for cross-linking. The resultant hydrogel has a uniform distribution of cross-links [13].
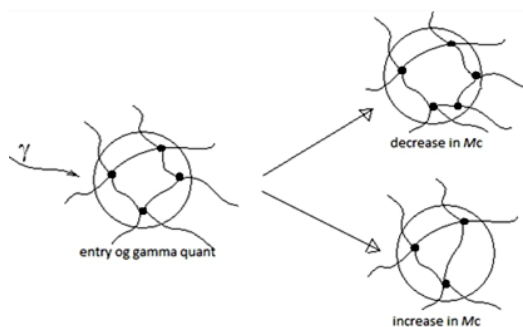

Fig. 1: Possible outcome after entry of gamma quant .

In this study we observe the change of gellation time with the change of dose of gamma radiation within different types of alginate. NaAlg powder samples were irradiated with gamma rays in air at ambient temperature in the solid state at low dose rates.

2. MATERIALS AND METHODS

Sodium alginate samples were obtained from FCM Biopolymers Company, Norway and used as received. The initial weight-averaged molecular weight of NaAlg type LF120M is $\overline{M}_w$ of $670 \cdot 10^3$ g/mol, and the guluronic to mannuronic acid residues G/M is 70/30. Calcium carbonate and D-glucono-δ-lactone (GDL) were obtained from Aldrich. The polymer powder samples were placed in tightly closed cylindrical containers, and irradiated at the required doses of 2.5 kGy, 5 kGy, 10 kGy and 15 kGy in a Gammacell 220 type 60 Co-gamma irradiator at room temperature in air.

2.1 Preparation of Alginate Gels

A $CaCO_3$-GDL system was used to achieve activated controlled gellation. Calcium carbonate ($CaCO_3$) was used as a source of calcium ions to initiate gellation and GDL was used as a weak acid for the activation of calcium ions from the carbonate. A molar ratio of calcium ion to GDL of 0.36 was used in order to secure preparation of an uniform gels from 1.5% sodium alginate solution as follows: 0.105g of sodium alginate was dissolved in 7 ml of deionized water and 0.0158 g $CaCO_3$ was put into the sodium alginate solution and the mixture was vortexed for 60 seconds. 0.056 g of GDL was dissolved in 0.02 mL of deionized water and added into alginate solution immediately and vortexed for 45 seconds and then put to rest. Through the same method calcium alginate activated solutions were prepared from irradiated sodium alginates [14].

2.2 Viscosity test equipment

After activation the solution is put in the cylindrical part of the test equipment. Then a type SC4-21 spindle is inserted and set to rotate at speed of 50 rpm. Temperature of the measurement was 25 ^{o}C. Sheer rate of the viscosity testings was 46.50 s^{-1}. During measurements the % torque changes from starting value up to max. of 105% when the motor of the instruments stops to prevent damage to the instrument. The tube and spindle are then cleaned and prepared for the next solution. It is noted that solutions are activated immediately before the viscosity test.

3. RESULTS AND DISCUSSION

Here we give the results for the gellation time for alginate irradiated with different gamma irradiation doses.

From fig.2 we get overall idea for the change in gellation time of the alginate with constant concentration and cross-link ratio but with different dose of irradiation. Starting from

fig.3 to fig.7 we give separate graphs for each dose with a logarithmic fit $y = (A_1 - A_2)/1 + (x/x_0)^p + A_2$ that gives us great extrapolation curve to find the final viscosity and gellation time.
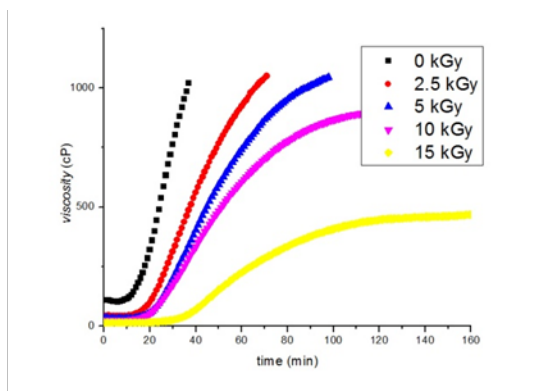

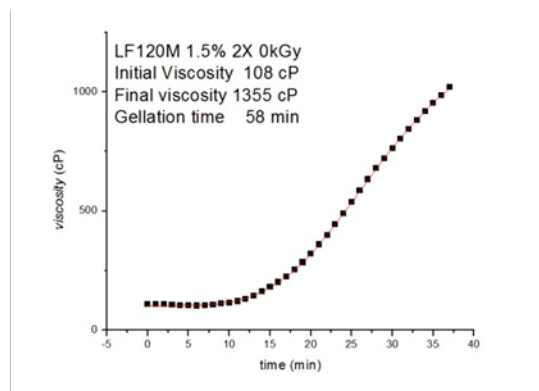**Fig. 2**: Overall change in gellation time for alginates

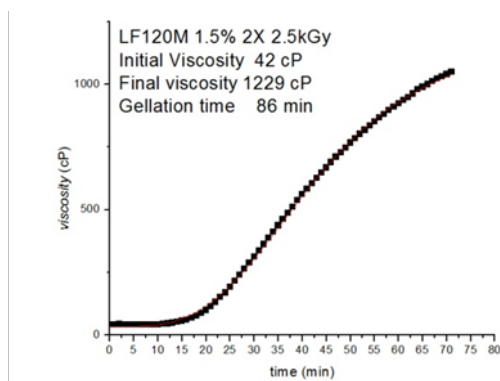**Fig. 3:** Gellation curve for alginate type LF120M at 0 kGy.

Fig. 4:Gellation curve for alginate type LF120M at 2.5kG.
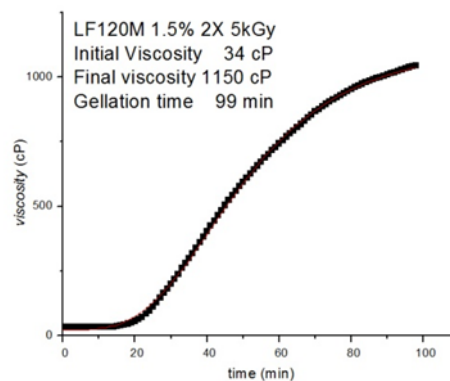
Fig. 5: Gellation curve for alginate type LF120M 5 kGy.
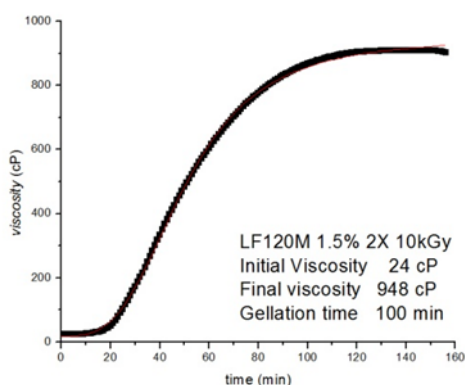
Fig. 6:Gellation curve for alginate type LF120M at 10 kGy.
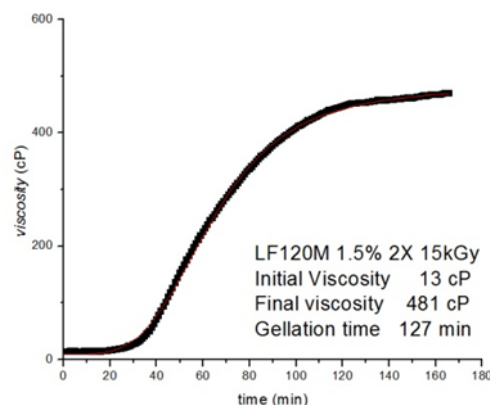
Fig. 7: Gellation curve for alginate type LF120M at 15 kGy.

In the following table we summarize the results.

Table 1: Viscosity results.

Irradiation (kGy)	Initial Viscosity (cP)	Final Viscosity (cP)	Gellation time (min)
0	108	1355	58
2.5	42	1229	86
5	34	1150	99
10	24	948	100
15	13	481	127

From a linear fit of the results shown in Table 1 we can see that the final viscosity decreases linearly with increase of the irradiation dose (Fig.8). The results in table 1 clearly show that gamma radiation has a degrading effect on the polymer. Because the gellation time is connected to the molecular weight or simply the length of the chains we see that with the increase of the dose the polymer degrades and with it the time it takes for the chains to form a gel network increases.
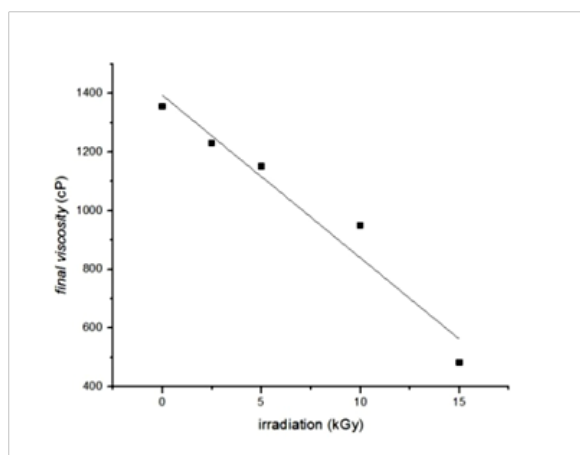
Fig. 8: Linear fit of the dicrease in the final viscosity.

4. CONCLUSION

In this study we confirm that irradiation has a degrading effect on the structure of alginates and that increase in gellation time is linearly correlated to the absorbed dose of gamma irradiation. In further research that we are going to follow it is of great importance to determine the molecular weight of the irradiated alginates and correlate the molecular weight to the final viscosity. In this way if we know the initial molecular weight of nonirradiated alginate sample we can use gellation time experiment as another method to determine the molecular weight of the irradiated alginates at any doses.

REFERENCES

[1] Anne Charlier, Bernard Lecerc, Guy Couarraze*, Releas of miferpristone from biodegradable matrices: experimental and theoretical valuations, *International journal of pharmaceutics* **200,** 115-120 (2000)

[2] M. Sen, O.Guven, Radiation synthesis of poly(N-vinyl 2-pyrrolidone/itaconic acid) hydrogels and their controlled release behaviours, *Radiation Physics and Chemistry* **55,** 113-120 (1999)

[3] B. Rabgarjan, L.S. Coons and A.B. Scranton, Characterization of hydrogels using luminescence spectroscopy, *Biomaterials* **17,** 649-661 (1996)

[4] David, B.I., An Introduction to Polymer Physics, Cambridge University Press, New York (2002)

[5] Blackley, D.C., Synthetic Rubbers, Applies Science Publishers, London (1983)

[6] Grant, G.T., Morris, E.R., Rees, D.A ., Smith, P.J.C., Thom, D., 1973. Biological interactions between polysaccharides and divalent cations: the egg-box model. FEBS Lett. 32, 195–198.

[7] Smidsrod, O., 1974. Molecular basis for some physical properties of alginates in gel state. J. Chem. Soc. Faraday Trans. 57, 263–274.

[8] Klock, G., Frank, H., Houben, R., Zekorn, T., Horcher, A., Siebers, U., Wohrle, M., Federlin, K., Zimmermann, U., 1994. Production of purified alginates suitable for use in immunoisolated transplantation. Appl. Microbiol. Biotechnol. 40, 638–6 43.

[9] K. I. Draget, G. SkjakBraek, O. Smidsrod, Alginate ba-sed new materials, Int. J Biol Macromol., 21 (1997) 47.

[10] O. Smidsrod. A. Haug, Effect of divalent metals on properties of alginate solutions I. Calcium ions, Acta Chem. Scand., 19 (1965)

[11] 329Stojan J. Rendevski, Influence of microgel particles of sodium alginate on gel structure of calcium alginate gels used for controlled release of active substances, Doctoral dissertation, Skopje, 2004.

[12] RENDEVSKI, S., POPESKI-DIMOVSKI, R. "A new method for measuring swelling kinetics of polymer gels, AIP Conference Proceedings, 899, 775 (2007)

[13] C. K. Kuo, P. X. Ma, Ionically crosslinked alginate hydrogels as scaffolds for tissue engineering: Part 1. Structure, gellation rate and mechanical properties, Biomaterials, 22 (2001) 511.

[14] Riste P.Dimovski, γ radiation induced changes in the bioadhesion properties of Ca-alginate gels, Master thesis, Skopje, 2009

CHARACTERIZATION OF AAm/MBA HYDROGELS PREPARED BY RADIATION INDUCED POLYMERIZATION

N. Mahmudi[1*] and S. Rendevski[2]

[1] *Faculty of Natural Science and Mathematics, State University of Tetovo, Bul. Ilinden bb, 1200 Tetovo, Republic of Macedonia*

[2] *Faculty of Electrical Engineering, University "Goce Delcev", Krste Misirkov, b.b., 2000 Stip, Republic of Macedonia*

Abstract. In this research the network structure of polyacrylamide hydrogels prepared by gamma radiation-induced polymerization has been investigated. The average molecular weight between cross-link junctions $\overline{M}_c$ and effective cross-link density of hydrogels were calculated from swelling data as well as shear modulus data. The mechanical tests showed that by increasing the amount of the crosslinker methylenebisacrylamide (MBA) into hydrogels, the value of shear modulus G and cross-link density ν_e increased, but the average molecular weight between cross-link junctions $\overline{M}_c$, decreased. The $\overline{M}_c$ and the effective cross-link density ν_e obtained from the mechanical characterization were significantly different than the values obtained from swelling experiments. These differences were attributed to the uncertainty on the value of the χ parameter used in the Flory-Rehner equations. The results have shown that simple compression analyses can be used for the determination of ν_e without any need of polymer-solvent interaction parameter for its calculations from the swelling analysis.

PACS: 61.25.hp; 61.80.Ed; 62.20.de; 82.35.Lr

INTRODUCTION

Cross-linked polymers are generally chemically prepared from AAm monomers in the presence of cross-linking agent and water. It is also well known that ionizing radiation that induces simultaneous polymerization and crosslinking has some advantages over chemical cross-linking and it is widely used in recent years for the synthesis of various hydrogels for biomedical applications. One of the basic parameters that describe the structure of a hydrogel network is the average molecular weight between cross-links or cross-link density of the network, $\overline{M}_c$. Several theories have been proposed to calculate the average molecular weight between cross-links. In the highly swollen state, the constrained junction theory indicates that a real network exhibits properties closer to those of the phantom network model. The following equation derived from the phantom network model has been used for nonionic polymeric networks known as Flory–Rehner equation [1,2]:

$$\overline{M}_c = -\frac{(1-2/\varphi)V_1 v_{2r}^{2/3} v_{2m}^{1/3}}{\overline{v}\left(\ln(1-\chi_{2m})+v_{2m}+v_{2m}^2\right)} \,, \tag{1}$$

where $\overline{v}$ - polymer specific volume; V_{2m} – polymer volume fraction of crosslinked polymer at swelling equilibrium; V_{2r} – polymer volume fraction in relaxed state; V_1 – molar volume of the swelling agent (water); ϕ - number of branches originating from the crosslinking sites.

The shear modulus values were calculated from the equation (2), where f is the force acting per unit cross-sectional area of the gel speciment, and λ is the deformation ratio:

$$f = G(\lambda\text{-}\lambda^{-2}). \tag{2}$$

When the equation (2) is applied to the initial stages of deformation, plots of f versus $\lambda - \lambda^{-2}$ yield straight lines (Fig. 2) where λ is the deformation ratio and equal to *L/Lo*. *Lo* and *L* are the lengths of the undeformed and deformed hydrogels during compression, respectively. The *G* values were calculated from the slope of the lines and are listed in Table 2. *G* is in connection to other parameters in the equation (3):

$$G = A\frac{\rho}{\overline{M}_c}RTv_{2r}^{2/3}v_{2m}^{1/3}\,, \tag{3}$$

where *A* is a prefactor and equals 1 for an infinite network and $(1\text{-}2/\phi)$ for a phantom network; ρ is polymer density [3]. The effective cross-link density, v_e, of a cross-linked structure can be obtained from the results of compressive strain measurements using Eqs. (2)–(4)[4]:

$$\overline{M}_c = \frac{\rho}{v_e}\,. \tag{4}$$

By using *G* values and other relevant experimental parameters, $\overline{M}_c$ could be calculated from the mechanical analysis according to equation (3). v_e usually is calculated from the corresponding relation, $v_e = \rho/\overline{M}_c$. The values of $\overline{M}_c$ and v_e calculated from the mechanical properties are different from those obtained by using Eq.(1) and swelling experiments. Large difference between them was attributed to the uncertainty on the value of the χ parameter used in the modified Flory-Rehner equation (1),[5,6]. The χ_s parameter is calculated from the swelling analysis according to relation $\chi_s \cong 1/2 + v_{2m}/3$. The real χ_m parameter is calculated by using $\overline{M}_{c(m)}$ values from Eq(1). Recalculated χ_m by using $\overline{M}_c$ from Eq(3) in Eq(1) and the differences between χ_s and χ_m are also given in Table 2.

2. EXPERIMENTAL

In the research, three components were used in the preparation of acrylamide–methylenebisacrylamide (AAm//MBA/water) hydrogels, namely acrylamide as monomers and

methylenebisacrylamide as the cross-linking agents and water as dispersing medium. The mass proportion of the monomers in the initial mixtures is summarized in Table 1. The AAm/MBA/water solutions were placed in PVC straws of 3 mm diameter and irradiated at 15 kGy. This has been determined to be minimum dose corresponding to complete conversion. Fresh hydrogels obtained in long cylindrical shapes were cut into pieces 3–4 mm in length. Unreacted monomer and uncrosslinked polymers were removed by washing the gels for two days in distilled water. They were dried in vacuum oven on 315 K. Percentage gelation i.e. percentage conversion of monomers and cross-linking agent into insoluble networks, was based on the total weight of the cross-linking agent and monomer in the initial mixture. Washed and dried hydrogels were left to swell in distilled water at room temperature to determine the maximum swelling degree. Elastic properties and shear modulus of hydrogels were determined by using a Zwick Z010 model Universal Testing Instrument and uniaxial compression module. The crosshead speed was 5 mm/min.

Table 1: Mass of monomer, cross-linking agent and water into composition

Sample code	Mass of monomer (g)	Mass of cross-linking agent (mg)	Water (ml)
0.4g AAm / 1mgMBA/1ml H$_2$O	0.4	1	1
0.4g AAm / 2mgMBA/1ml H$_2$O	0.4	2	1
0.4g AAm / 4mgMBA/1ml H$_2$O	0.4	4	1
0.4g AAm / 6mgMBA/1ml H$_2$O	0.4	6	1
0.4g AAm / 8mgMBA/1ml H$_2$O	0.4	8	1
0.4g AAm /15mgMBA/1ml H$_2$O	0.4	15	1

3. RESULT AND DISCUSSION

For the characterization of the network structure and determination of effective cross-link density of prepared hydrogels their swelling behavior at pH 7 was first investigated. The percentage swelling of hydrogels was calculated by the following equation;

$$S\% = \left[\left(m_t - m_0 \right) / m_0 \right] \cdot 100 . \tag{5}$$

where m_t and m_o are the weights of the swollen and dry gels respectively.

The S% equilibrium swelling values of all prepared hydrogels were collected in Table 2. As can be seen from this table S% swelling of hydrogels is lower than 512%. The equilibrium value of swelling was used in each case to calculate the volume fraction of polymer (v_{2m}) by using Eq. (6) given below where ρ and ρ_w are the densities of dry gel and water. w is the weight fraction of polymer in swollen gel.

$$1/v_{2m} = \left[1 + \rho / \rho_w \left(w^{-1} - 1 \right) \right] . \tag{6}$$

The χ parameter of hydrogels is generally calculated by using the following equation [7].

$$\chi \cong 1/2 + v_{2m}/3, \tag{7}$$

which is the result of an assumption as $\overline{M}_c$ goes to infinity which makes the denominator in Eq. (1) equal to zero i.e.

$$\ln\left(1 - v_{2m}\right) + v_{2m} + \chi v_{2m}^2 = 0 \tag{8}$$

For small v_{2m} values the χ parameter approaches to 0.5. The $\overline{M}_{c(s)}$ values are calculated by using v_{2m} and values of χ obtained from Eq. (7) and other parameters from swelling experiments. The results collected in Table 2 derived from swelling experiments have "s" in the abbreviations.

For the investigation of the effect of MBA on the mechanical properties of AAm hydrogels and for the determination of true $\overline{M}_c$ ($\overline{M}_{c(m)}$) and χ parameter, uniaxial compression was applied by using the Universal Testing Instrument. The subscript ''m'' was used to indicate that these parameters are calculated from mechanical measurements. Typical stress–strain curves of hydrogels were given in Fig.1. As can be seen from the figure, the magnitude of stress increased with increasing MBA content in the hydrogel for a given strain. Shear modulus values of hydrogels were calculated by using elastic deformation theory and Eq. (2). [1]. By using G values and other relevant experimental parameters, $\overline{M}_c$ and v_e were calculated from Eqs. (3) and (4) and collected in Table 2. As can be seen from Table 2, the magnitudes of $\overline{M}_c$ calculated from mechanical properties are different from those obtained by using swelling experiments. Large difference was attributed to using incorrect χ parameter in the modified Flory–Rehner equation. The actual χ parameters were calculated by using $\overline{M}_{c(m)}$ values and Eq. (1). Recalculated χ parameters (χ_m) and the differences between χ_s and χ_m are also given in Table 2.

For the investigation of the effect of χ parameter on the $\overline{M}_c$ values, the theoretical $\overline{M}_c$ values were obtained (Fig. 3) by using χ and experimentally obtained polymer based parameter. As can be seen from Fig. 3 and Table 2, for first sample of AAm/MBA composition, only 0.034428 changes in χ parameter caused 8.48 fold increase in the $\overline{M}_c$ value. For the second sample changes in χ parameter by 0.050436 caused 10.4 fold increase in $\overline{M}_c$. For the third sample, 0.047788 difference in the χ parameter caused 8.04 fold increase in $\overline{M}_c$. For the fourth sample, 0.044212 difference in the χ parameter caused 6.45 fold increase in $\overline{M}_c$. For the fifth sample, 0.034103 difference in the χ parameter caused 4.24 fold increase in $\overline{M}_c$. For the sixth sample, 0.039008 difference in the χ parameter caused 4.05 fold increase in $\overline{M}_c$. These results clearly show that for the precisely determination of crosslink density of low degree swelling hydrogels, the χ parameter must be calculated (measured) more precisely [5,6].

In this study we also showed the effect of higher concentration of the cross-linking agent MBA on the increasing of mechanical properties of AAm/MBA hydrogels which is

shown on Table 2. The increasing of cross-linking agent from 1mg in the first sample to 15 mg in the sixth sample causes the increasing of G value from 87.1 kPa to 298.5 kPa.

As can be seen from Table 2, the increasing of amount of cross-linking agent from 1mg to 2mg caused the decreasing of $\overline{M}_c$ calculated by swelling method and compress test for 1.34 and 1.64 fold, respectively; the increase from 2mg to 4mg caused the decreasing of $\overline{M}_c$ calculated by swelling method and compress test for 1.49 and 1.16 fold, respectively; the increase from 4mg to 8mg caused the decreasing of $\overline{M}_c$ calculated by swelling method and compress test for 1.33 and 1.065 fold, respectively and the increase from 8mg to 15mg caused the decreasing of $\overline{M}_c$ calculated by swelling method and compress test for 1.55 and 1.48 fold, respectively.
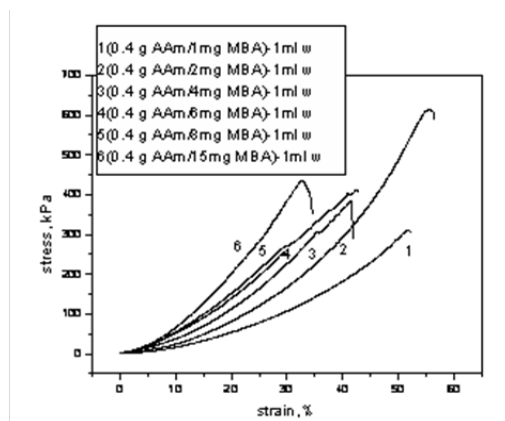

Fig. 1: Strain versus stress curves of AAm/MBA hydrogels
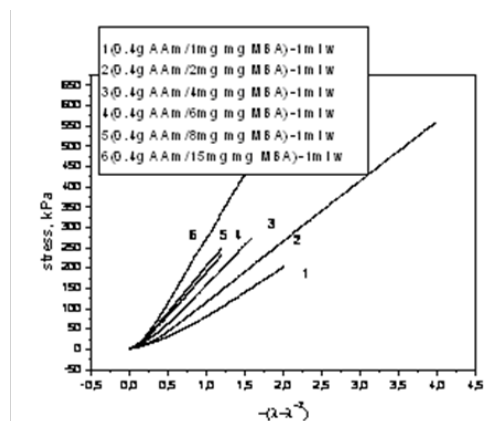
Fig. 2: $-(\lambda-\lambda^{-2})$ versus stress curves of AAm/MBA hydrogel.

Table 2: The swelling and mechanical parameters of AAm/MBA hydrogels: Flory polymer interaction parameters χ_s, χ_m; average molecular weight between hydrogel junction zones $\overline{M}_{c\,(s)}$, $\overline{M}_{c\,(m)}$; effective crosslink density $ve_{(s)}$, $ve_{(m)}$, all obtained from the swelling and mechanical analysis, and shear modulus values G.

Sample	S,%	χ_s	$\overline{M}_{c\,(s)}$	$\overline{M}_{c\,(m)}$	χ_m	$ve_{(s)}$	$ve_{(m)}$	$\chi_s - \chi_m$	G (kPa)
0.4g AAm / 1mgMBA/1ml H_2O	512	0.54282	21028	2478	0.508392	6.29E-05	0.000534	0.034428	87.1
0.4g AAm / 2mgMBA/1ml H_2O	476	0.546041	15665	1506	0.495606	8.36E-05	0.000869	0.050436	143.9
0.4g AAm / 4mgMBA/1ml H_2O	410	0.551385	10445	1298	0.503597	0.000128	0.00103	0.047788	175.3
0.4g AAm / 6mgMBA/1ml H_2O	376	0.555835	7844	1215	0.511622	0.000168	0.001087	0.044212	198.5
0.4g AAm / 8mgMBA/1ml H_2O	337	0.562963	4998	1178	0.52886	0.000254	0.001078	0.034103	215.3
0.4g AAm /15mgMBA/1ml H_2O	318	0.568819	3224	795	0,529812	0.000375	0.001519	0.039008	298.5

4. CONCLUSION

The aim of this study was to control the mechanical properties of radiation synthesized hydrogels by using different amounts of cross-linker into feed solution.

The decreasing of percentage swelling of hydrogels, the decreasing of the average molecular weight between junctions $\overline{M}_c$ and increasing of G modulus is caused by increasing of the amount of cross-linking agent into feed solution. The characterization of the network structure of hydrogels was done by determination of molecular weight between cross-links and effective cross-link density of radiation synthesized AAm/MBA hydrogels by using data from swelling analyses and compression tests. Values calculated from mechanical tests were found to be quite different from those obtained by using swelling experiments. Large difference was attributed to the incorrect value of the χ parameter used in the modified Flory–Rehner equation. These results clearly show that for reliable determination of cross-link density of hydrogels the χ parameter must be precisely determined experimentally from swelling experiments.
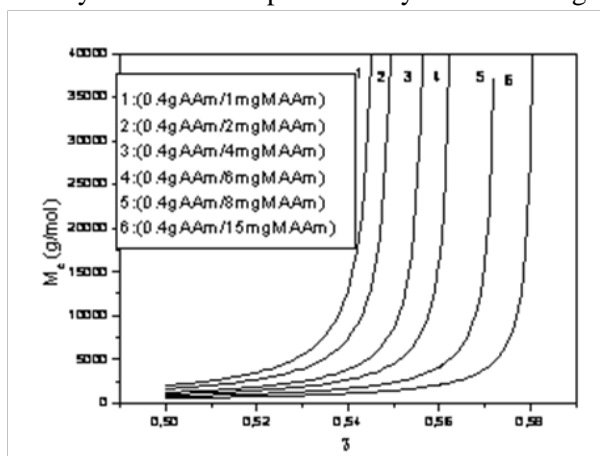
Fig. 3: The change of $\overline{M}_c$ with χ value of AAm/MBA hydrogels.

REFERENCES

[1] J.E. Mark, B. Erman (Eds.), Rubberlike Elasticity a Molecular Primer, Wiley, New York (1988).

[2] M. Şen, N. Pekel, O. Güven, *Angew. Macromol. Chem.* 251 (1998) 1.

[3] O. Okay, S. Durmaz, *Polymer*, 43, 1215-1221 (2002).

[4] O. Uzun, M. Hassnisaber, M. Şen, O. Güven, *Nuclear Instruments and Methods in Physics Research B.* 208, 242-246 (2003).

[5] N. Mahmudi, M. Şen, S. Rendevski, O. Güven, *Nuclear Instruments and Methods in Physics Research B.* 265, 375-378 (2007)

[6] N. Mahmudi, M. Şen, O. Güven S. Rendevski, *Sixth International Conference of the Balkan Physical Union,* Proceedings AIP. CP899 (2007).

[7] W. Xue, S. Champ, M.B. Huglin, *Polymer* 42, 3665-3669 (2001).

FORENSIC SPEAKER IDENTIFICATION THROUGH COMPARATIVE ANALYSIS OF THE FORMANT FREQUENCIES OF THE VOWELS IN THE MACEDONIAN LANGUAGE

V. Pop-Dimitrijoska[1], G. Apostolovska[1], B. Gerazov[2], Z. Ivanovski[2] and J. Jovanovski[3]

[1]Institute of Physics, Faculty of Natural Sciences and Mathematics, Gazi Baba bb, 1000 Skopje, Macedonia

[2]Institute of Electronics, Faculty of Electrical Engineering and Information Technologies, Rugjer Boshkovik bb, 1000 Skopje, Macedonia

[3]Faculty of Computer Science and Engineering, Rugjer Boshkovik 16, 1000 Skopje, Macedonia

Abstract. The main objective of this study is forensic speaker identification from an incriminated recording. The identification was made through a comparative analysis between first three formants F_1, F_2 and F_3 of the voice samples from the questioned and suspects' recordings. The measurements were made with the PRAAT software, for each of the five vowels in the Macedonian language: *a, e, i, o* and *u,* which were isolated from the recordings. Used methodology of recording examinations employed in this research showed positive identification of the questioned voice. The forensic audio analysis still doesn't have its place in legal and the crime fighting systems in Macedonia. This is a sufficient reason to put a bigger accent on the research of this issue in the future that will contribute in solving many criminal cases which until now, because of the type of generally accepted evidence, were not resolved.

1. INTRODUCTION

Voice identification is based on the theory that each person's voice is unique like his fingerprint and his DNA. But this analogy is not entirely accurate, given that the "voice print" is not as unique, distinctive and inimitable as a fingerprint. However, voice has individual characteristics that are a result of the organs for sound production, the shape of the vocal tract, the oral cavity, the way of pronunciation, the regional accent, and others, that enable the discrimination of voices, which is not absolute, but is expressed by a probability scale.

A very significant element of speaker identification studies is the analysis of the vowel system used by the speaker. Vowels are voiced segments with a formant structure. Formants are the distinguishing and meaningful frequency components of human speech. They are the resonant frequencies that individualize the speaker, as a result of the anatomical structure of his speech organs. During an analysis of the vowels, the most important is the relative position of the first, second, third, and sometimes fourth formant [5], [3].

1.1. Collecting voice samples and measurements

In this paper we demonstrated a procedure for conducting a voice identification analysis. From an allegedly incriminated recording, taken with a mobile phone, it is necessary to identify the person from the recording. There are 18 suspects whose voice samples have been taken and it is necessary to identify which of those suspects is the one from the incriminated recording, by performing comparative analysis of the formants, as the most important acoustic parameter.

Three voice samples from 18 female individuals, aged 27 to 42 have been taken. They all come from the same language area and speak the Macedonian language, which is also their mother tongue.

The digital recordings of the suspects and the incriminating recording are taken by a mobile phone, iPhone 4s, and they are in a MPEG-4 Audio File Format (.m4a). The recording of the speech samples was done in a quiet environment with short reverberation.

While taking the voice sample from the suspects, they were given a printed version of the speech from the incriminating recording and the text was read in order to capture the speed of the voice, its accent, dialect, etc. In this way the recordings of the suspects will more reliably reflect the dynamics of speech from the incriminating recording. The goal was to minimize the attempts to disguise the voice, by eventually adding false accent, a change in the speed of pronunciation and so on. The best technique for obtaining the prosodic features is the technique of repeating with the speaker [2].

A further analysis is conducted by using the PRAAT software, so vocal segments are carefully and meticulously selected, with duration of 0.02-0.10 seconds and the mean values of the formants are read. Some of the vocals were rejected from the analysis because of:

- the merging of vowels with other speech sounds,
- the difficulties in reading the formants in the vocal segments smaller than 0.02 s,
- the occurrence of noise or whisper when the vocal segments are located at the end of the sentence,
- the occurrence of discontinuities and jumps of the formants in the vocal segments etc.

Only 57 vowels from text were successfully isolated and measurements were made of the mean values of the first three formants F_1, F_2 and F_3 for each of the five vowels in the Macedonian language: *a*, *e*, *i*, *o* and *u*. This was done for all three recordings of the 18 suspects, including the recording of the unknown person, so exactly 513 vowels were measured for every suspect.

2. RESULTS

Because the closest suspect to the incriminating record is required, the distances between the measured values of the formants are calculated and a similarity in the distribution of the formants is examined through the following methods.
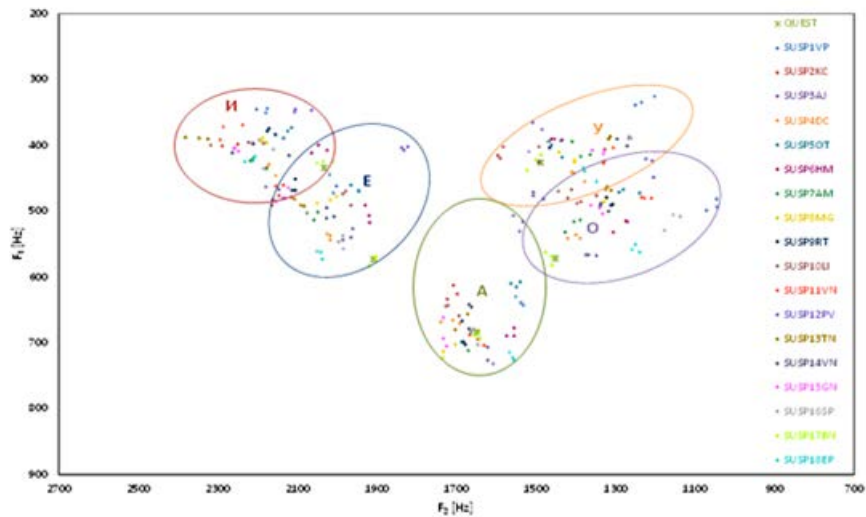
Fig. 1: Distribution of the mean values of formants from all audio samples.

Graphical presentation of formants distribution. Fig. 1 shows the distribution of the mean values of the formants for all the vowels, from all suspects including the unknown person. A most evident overlapping can be seen in QUEST and SUSP17BN. In Fig. 2 are shown distribution of the mean values of those two recordings in order to show their match more clearly.
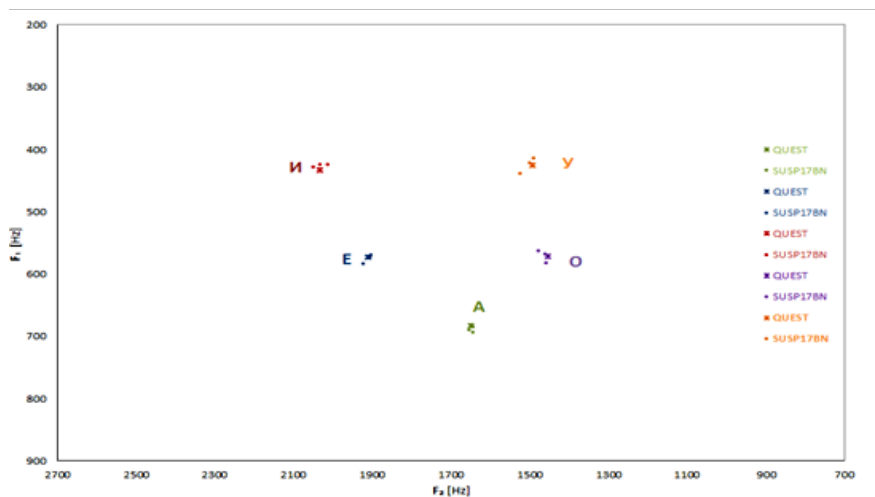
Fig. 2. Matching of the mean values of formants between QUEST and SUSP19BN

Fig. 2: Matching of the mean values of formants between QUEST and SUSP19BN.

Histograms. They show an important visual representation of the distribution of the data. For this purpose, normalized histograms for the formants F_1, F_2 and F_3, for all involved persons were calculated and visualized with Matlab. The widths of the intervals (bin-width) of the histograms are set 50 Hz for F_1, 100 Hz for F_2 and 100 Hz for F_3. The arithmetic means are marked with a red line, the standard deviations are marked with magenta, as follows: $\pm 1\sigma$, where there are 68.2% of all the data and $\pm 2\sigma$, where there are 95.4% of all the data. The histograms of the suspects are shown in blue, and the green shows the unknown person. From the histograms, a similarity in the distribution of the bins of the histogram between QUEST and SUSP17B can be observed, and it is the most distinctive in the histograms of the vowels *e* and *o*. Fig. 3 shows a histogram of the vowel *e*.

Euclidean distances. From the measures for calculating distance, we used the Euclidean distance, which is selected as a representation for the shortest straight-line distance between the two points, given by the Pythagorean formula. The average value of the Euclidean distances for all vowels will be shown here, first in 2D, between the frequencies (F_1, F_2), and then in 3D, between the frequencies (F_1, F_2, F_3). The summarized results of the computed distances are shown in Table 1, from where it is obvious that the smallest distance is between the formants of QUEST and SUSP17BN.

Percentage of relative deviation. The idea is to calculate the relative deviations of the formants i.e. their relative errors, presuming that the two recordings which are compared belong to the same person. The result is expressed as a percentage. A low percentage would mean a slight deviation between the recordings and a possibility that they originate from the same person. The summarized results are shown in Table 1, from where it can be seen that the percentage of deviation is the smallest between QUEST and SUSP17BN, suggesting the possibility that they originate from the same person.
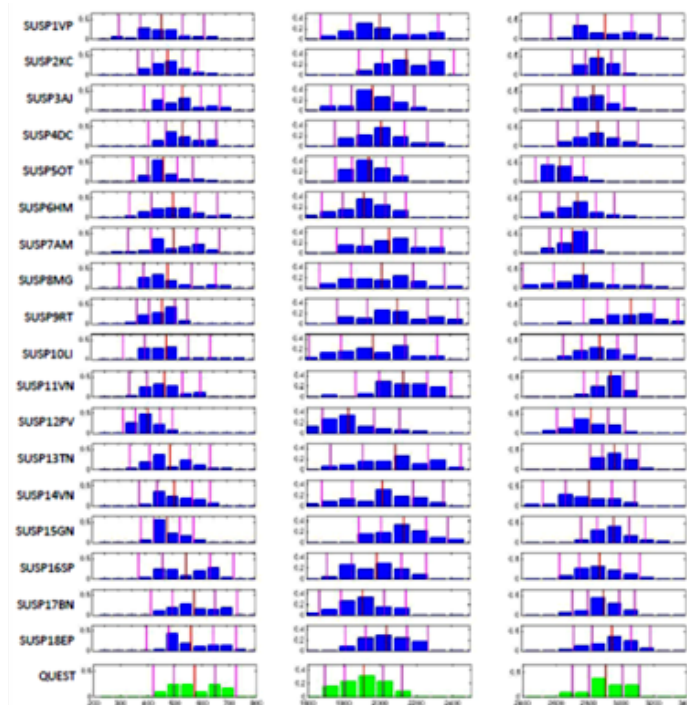

Fig. 3. Histograms of F_1, F_2, F_3, for the vowel *e*. There is evident similarity between formant distribution of QUEST and SUSP17BN

Automatic voice identification with the software - **SIS II**. In order to receive more reliable results, they are reviewed by using specialized forensic software for audio-analysis and speaker identification - SIS II, from the Russian company Speech Technology Center (STC). The software has a special plugins for speaker identification - Automatic Identification Plugins. The obtained results showed biggest similarity of QUEST with SUSP17BN and they are shown in Table 1.

Using the software for the purposes of this study was temporarily enabled by the company Speech Technology Center (STC) [6].

Table 1. Summarized results of the comparison between formants

Suspects Code	Euclidean distances measured between (F_1, F_2) [Hz]						Euclidean distances measured between (F_1, F_2, F_3) [Hz]						Relat. deviat.	Similarity calculated with SIS II
Vocals	*a*	*e*	*i*	*o*	*u*	Σ/n	*a*	*e*	*i*	*o*	*u*	Σ/n		
SUSP1VP	159	195	238	408	307	261	258	253	316	450	357	327	12.5%	49.3%
SUSP2KC	130	274	264	166	197	206	248	303	305	224	243	264	7.4%	67.2%
SUSP3AJ	88	110	200	136	130	133	189	168	246	159	190	190	4.0%	69.5%
SUSP4DC	122	138	188	111	120	136	315	218	223	156	189	220	4.1%	66.4%
SUSP5OT	131	153	161	221	156	164	409	318	244	311	302	317	10.1%	53.2%
SUSP6HM	107	133	119	190	88	127	288	239	174	296	326	265	6.5%	73.7%
SUSP7AM	89	190	218	100	131	146	334	291	285	204	274	278	6.4%	65.4%
SUSP8MG	105	187	199	189	186	173	259	308	285	255	275	276	6.9%	62.1%
SUSP9RT	94	241	244	177	91	170	211	339	351	340	204	289	7.6%	63.0%
SUSP10LI	94	190	202	131	73	138	154	243	250	171	140	192	5.6%	66.7%
SUSP11VN	147	275	306	255	188	234	218	303	366	265	214	273	8.3%	56.9%
SUSP12PV	218	217	163	286	203	217	265	258	254	320	298	279	13.1%	55.1%
SUSP13TN	115	231	335	188	180	210	183	267	402	221	233	261	8.1%	66.1%
SUSP14VN	90	177	213	188	218	177	206	248	295	254	335	268	7.3%	68.8%
SUSP15GN	106	263	237	147	157	182	207	296	287	233	273	259	7.5%	74.5%
SUSP16SP	65	143	174	320	231	187	188	211	251	444	407	300	7.8%	61.7%
SUSP17BN	32	48	57	43	40	44	63	68	103	72	87	78	0.6%	98.8%
SUSP18EP	132	156	228	215	224	191	198	206	272	228	296	240	4.9%	50.4%

3. CONCLUSIONS

The performed aural and spectrographic comparative analysis, and the results obtained with the different statistical approaches indicate a reliable identification of the unknown person from the incriminating recording, with the person SUSP17BN.

This research demonstrates an attempt of forensic speaker identification, through a comparative analysis of the formants and its aim is to show that under controlled conditions, without a professional and specialized hardware and software equipment, such an identification

is possible, based on the analysis and measurement of one of the most important acoustic parameters.

The study identifies the problems of inferring identity from speech in forensics. So when conducting voice identification analysis, we must consider the following problems:

- the complexities of voice sample comparison;
- the probabilistic nature of the technique;
- the difficulties introduced by differential variation within and between voices [1];
- the necessity for both acoustic and auditory comparison, and for the comparison of linguistic and non-linguistic features;
- the expertise required in several areas related to speech science, such as: linguistics, acoustics, statistics and of course forensics.

This research is the first of its kind in the Republic of Macedonia and it includes all recommended norms, technical standards or protocols that are practiced in such expertise and are accepted worldwide [4].

REFERENCES

[1] P. Rose, *Forensic speaker identification*, Taylor & Francis, 2002

[2] M. Heđever, *Uvod u forenzičnu fonetiku i akustiku*, skripta, Sveučilište u Zagrebu, 2009

[3] *Handbook of forensic science* - Jagiellonian University, Institute of Forensic Research, Poland, 2008

[4] S. Cain, *American Board of Recorded Evidence - Voice Comparison Standards*, The Forensic Examiner, April 1999

[5] K. Klus, A. Trawiñska, *Forensic speaker identification by the linguistic-acoustic мethod in Keú and Ies*, Problems of Forensic Sciences, vol. LXXVIII, 160–174, 2009

[6] http://speechpro.com/product/forensic_analysis/ikarlab - SIS II documentation.

WOODS-SAXON POTENTIAL IN THE PRESENCE
OF A COSMIC STRING

K. Jusufi[1] and D. Jakimovski[2]

*[1]Departament of Physics, Faculty of Natural Sciences and Mathematics,
State University of Tetovo, Ilinden Street nn,1200, Macedonia*

*[2]Institute of Physics, Faculty of Natural Sciences and Mathematics,
Ss. Cyril and Methodius University, PO Box 162, 1000 Skopje, Macedonia*

Abstract. We study the behavior of a non-relativistic quantum system of a neutron in a mean-field Woods-Saxon potential in the presence of cosmic string. The corresponding Schrödinger equation with this potential has been solved by modification of the radial part to become comparable with the associated Jacobi differential equation. We find the energy spectra and wave functions for this system and explore some differences compared to the analog system in flat Minkowski space-time.

PACS: 21.60.Ev, 04.20.Gz, 11.25.-w

1. INTRODUCTION

The effects of the gravitational field within the atomic realm continues to be an interesting research topic, with wide range of, relativistic and nonrelativistic, energies and scales. Especially important, in this context, are potentially observable changes in the energy levels of the microscopic quantum systems, due to geometric curvature, and / or other topological features of the space-time at the location of the system. One such a feature is the presence of a cosmic string, manifested as a topological defect, at atomic level.

Cosmic strings are exotic topological defects, suggested as an explanation for phase transitions in the very early Universe and of the observed global distribution of mass in galaxies, with spontaneously braking of extreme smoothness of the early space-time as their main mechanism of physical infuence [1]. As of today, however there is no experimental evidence that support their actual existence in nature and their use in theoretical models are of pure speculative nature. If exist they may have a word in some explanations of ultrahigh energy neutrinos, cosmological gamma-ray burst as well as the anisotropy of the cosmic microwave background radiation too. Their geometry should be localy flat, and may be described as conical which means that a particle near them does not feel local gravity. However they should change the energy levels of quantum systems due to the non-trivial topology of space-time around them [1,2].

In a recent study, Geusa de A. Marques and Valdir B. Bezerra [3,4 and references therein] have shown that an atom in a gravitational field is influenced by its interaction with the local curvature, as well as with the topology of the space-time, and as a consequence there is a

shift in the energies at the atomic level. The aim of this paper is to extend their model to nuclei, within the framework of mean-field Woods-Saxon potential. We have used the approach of M. R. Pahlavani, J. Sadeghi and M. Ghezelbash [5,6] were the radial Schrödinger equation, for small r, is solved by comparison with the associated Jacobi differential equation, and closed formula for energy levels are found, for this potential.

2. FORMULATION OF THE PROBLEM

To find the metric of the space-time one needs to solve the Einstein field equation

$$R_{\mu\nu} - \frac{1}{2}g_{\mu\nu}R = 8\pi G T_{\mu\nu}, \tag{1}$$

where $R_{\mu\nu}$ is Ricci tensor, $g_{\mu\nu}$ is the metric tensor, R the Ricci scalar and $T_{\mu\nu}$ is the stress-energy tensor (as for the unit system we adopt $c = 1$). One can show (see, for details [1,2]) that the exterior metric of an infinitely long straight and static cosmic string in spherical coordinates, takes the form

$$ds^2 = -dt^2 + dr^2 + r^2 d\theta^2 + \alpha^2 r^2 \sin^2\theta d\phi^2, \tag{2}$$

where $0 < r < \infty$, $0 < \theta < \pi$, $0 < \varphi \le 2\pi$ and $\alpha = 1 - 8\pi G\mu$ belongs to the interval $(0,1]$; μ being the linear mass density of the cosmic string. Thus, the space-time produced by an idealized cosmic string is locally flat, however globally may be described by conical geometry, with a planar angle deficit determined by $\delta = 8\pi G\mu$.

So, we need to solve the Shrödinger equaion in the presence of cosmic string, given by

$$i\hbar \frac{\partial \Psi}{\partial t} = -\frac{\hbar^2}{2m}\nabla^2_{LB}\Psi + V\Psi. \tag{3}$$

where the ∇_{LB} is the Laplace-Beltrami operator on the Riemannian manifold with the corresponding metric [7] and, in this case reads

$$\nabla^2_{LB} = \frac{1}{r^2}\left[\frac{\partial}{\partial r}\left(r^2 \frac{\partial}{\partial r}\right) + \frac{1}{\tan\theta}\frac{\partial}{\partial \theta} + \frac{\partial^2}{\partial \theta^2} + \frac{1}{\alpha^2 \sin^2\theta}\frac{\partial^2}{\partial \phi^2}\right], \tag{4}$$

and *V* is the main-field Woods-Saxon potential

$$V(r) = -\frac{V_0}{1 + e^{\frac{r-R_0}{a}}}, \tag{5}$$

R_0 and a being geometrical characteristics of the nuclei, and V_0 is the depth of the potential well at $r = 0$ [8]. With this we establish the theoretical context of our problem and proceed to its solution, in the following section, in units $\hbar = 1, m = 1$.

3. SOLUTION OF THE SCHRÖDINGER EQUATION

After transition to time-independent Schrödinger equation for ψ, in stationary environment, and substition of the expression for the potential, $V(r)$ one may proceed to standard separation of variables with the ansatz $\psi(r,\theta,\varphi) = R(r)\Theta(\theta)\Phi(\varphi)$. To simplify the expressions further we introduce new variables for the Woods-Saxon potential $r - R_0 \to r$ and $1/a \to 2\omega$.

The azimuthal part being the simplest to solve, $\Phi(\varphi) = C\exp(im\varphi)$. C is a constant and m assumes the values $m = 0, \pm 1, \pm 2, \ldots$ while for the other two parts we get

$$\left[\frac{1}{r^2}\frac{d}{dr}\left(r^2\frac{d}{dr}\right) + 2\left(E + \frac{V_0}{1+e^{2\omega r}}\right) - \frac{\lambda}{r^2} \right]R(r) = 0, \tag{6}$$

$$\left[\frac{1}{\tan\theta}\frac{\partial}{\partial\theta} + \frac{\partial^2}{\partial\theta^2} - \frac{m^2}{\alpha^2\sin^2\theta} + \lambda \right]\Theta(\theta) = 0, \tag{7}$$

λ being the separation constant.

By making the substitution $x = \cos\theta$ in the last equation one may obtain a type of Legendre differential equation with dependence on a parameter α whose solutions can be written via the generalized associated Legendre functions $\Theta(\theta) = P_{l_{(\alpha)}}^{m_{(\alpha)}}(\cos\theta)$, (see references [3,4] for details) with $m_{(\alpha)} \equiv m/\alpha$, $l_{(\alpha)} \equiv l - (1 - 1/\alpha)m$, $l = 0,1,2,\ldots$ and for the separation constant, $\lambda = l_{(\alpha)}(l_{(\alpha)} + 1)$. Now we make an approximation, valid for $r \to 0$,

$$r = \frac{1}{2\omega}\left(e^{2\omega r} - 1\right) \tag{8}$$

and solve the radial part of Schrödinger equation, by making the substitution $R(r) = u(r)/r$ and introducing a new variable $x = \tanh(\omega r)$ to obtain

$$\left(1-x^2\right)\frac{d^2u(x)}{dx^2} - 2x\frac{du(x)}{dx} + \left[\frac{\varepsilon^2}{(1-x^2)} + \frac{v^2}{(1+x)} - \frac{l_{(\alpha)}\left(l_{(\alpha)}+1\right)(1-x)}{x^2(1+x)}\right]u(x) = 0, \tag{9}$$

where with $\varepsilon^2 = \left|2mE/\omega^2\right|$, $v^2 = V_0/\omega^2$ we follow the notation from [3]. This equation can be modified to become comparable with Jacobi differential equation with real parameters $\gamma, \beta > -1$, in the interval $x \in (-1,1)$

$$\left(1-x^2\right)\frac{d^2}{dx^2}P_{nl}^{(\gamma,\beta)}(x) + \left(\beta - \gamma - (\gamma + \beta + 2)x\right)\frac{d}{dx}P_{nl}^{(\gamma,\beta)}(x) +$$
$$+ \left[n(\gamma + \beta + n + 1) - \frac{l(\gamma + \beta + l + (\gamma - \beta)x)}{1-x^2}\right]P_{nl}^{(\gamma,\beta)}(x) = 0 \tag{10}$$

where n, l are non-negative integers and $0 \leq l \leq n < \infty$.

Let us substitute $u(x)$ to be product of two, tentatively unknown functions $v(x)$ and $w(x)$ to obtain

$$(1-x^2)\frac{d^2}{dx^2}v(x)+\left[2(1-x^2)\frac{w'(x)}{w(x)}-2x\right]\frac{dv(x)}{dx}+$$

$$+\left[(1-x^2)\frac{w''(x)}{w(x)}-2x\frac{w'(x)}{w(x)}+\frac{\varepsilon^2}{(1-x^2)}+\frac{v^2}{(1+x)}-\frac{l_{(\alpha)}(l_{(\alpha)}+1)}{x^2}\frac{(1-x)}{(1+x)}\right]v(x)=0 \tag{11}$$

By comparing the last two equations, one may easily find $w(x)=C(1+x)^{\beta/2}(1-x)^{\gamma/2}$, C being some constant. Similarly, one may find that from this comparision follows

$$\left(\frac{\gamma^2}{4}-\frac{\gamma}{2}\right)+\left(\frac{\beta^2}{4}-\frac{\beta}{2}\right)-\frac{\gamma\beta}{2}+\varepsilon^2+v^2-l_{(\alpha)}(l_{(\alpha)}+1)=n(\gamma+\beta+n+1)-l(\gamma+\beta+l)$$

$$2\left(\frac{\gamma^2}{4}-\frac{\gamma}{2}\right)-2\left(\frac{\beta^2}{4}-\frac{\beta}{2}\right)+\gamma-\beta-v^2=-l(\gamma-\beta)$$

$$\left(\frac{\gamma^2}{4}-\frac{\gamma}{2}\right)+\left(\frac{\beta^2}{4}-\frac{\beta}{2}\right)+\frac{\gamma\beta}{2}+\gamma+\beta=-n(\gamma+\beta+n+1)$$

$$l_{(\alpha)}(l_{(\alpha)}+1)=0$$

From these four equations one may, with usual algebraic manipulations, find expression for ε^2 and for energy, as following

$$E_{nl_{(\alpha)}}=-\frac{\hbar^2\omega^2}{2m}(\gamma+l)^2, \tag{12}$$

provided the quantization condition for α, from $l_{(\alpha)}(l_{(\alpha)}+1)=0$ is fulfilled; hence the index $l_{(\alpha)}$. Putting together all parts of the wave function, we arrive at

$$\Psi_{nlm\alpha}(r,\theta,\phi)=$$

$$=\frac{C}{r}(1+\tanh\omega r)^{\beta/2}(1-\tanh\omega r)^{\gamma/2}e^{im\phi}\,P_{l_{(\alpha)}}^{m_{(\alpha)}}(\cos\theta)P_l^{(\gamma,\beta)}(\tanh\omega r). \tag{13}$$

4. CONCLUSIONS

The non-trivial space-time background, in general shifts the energy levels of quantum systems and in some simple potentials with high symmetry, can restrict even their existence with making additional conditions for the theoretical framework to be fulfilled, such as above $l_{(\alpha)}(l_{(\alpha)}+1)=0$. This conclusion, supported in this paper, for mean-field Woods-Saxon potential without a Coulomb barrier, agree in full with the results presented in available references for other simple potentials.

REFERENCES

[1] *A. Vilenkin and E.P.S Shellard*, *Cosmic Strings and Other Topological Defects Cambridge* University Press, Cambridge, England, 1994

[2] M. R. Anderson, *The Mathematical Theory of Cosmic Strings,* Institute of physics publishing Bristol and Philadelphia, 2003

[3] G. de A. Marques and V. B. Bezerra, Some effects on quantium systems due to the gravitational field of a topological defect. Brazilian Jornal of Physics **35** no.4B, December 2005

[4] G. de A. Marques and V. B. Bezerra, arXiv:quant-ph/0107034v1

[5] M.R. Pahlavani, J. Sadeghi and M. Ghezelbash, Non-relativistic bound states for modified Woods-Saxon potential BSG Proceedings, 15. The International Conference "Differential Geometry - Dynamical Systems" DGDS-2007, October 5-7, 2007, Bucharest-Romania, pp. 148-153.

[6] M.R. Pahlavani, J. Sadeghi and M. Ghezelbash, Solutions of the central Woods-Saxon potential in $l \neq 0$ case using mathematical modification method, Applied sciences **11**, pp. 106-113, 2009

[7] B. Thaller, Advanced Visual Quantum Mechanics, Springer, 2005 **35**, no. 4B, December, 2005

[8] S. Flügge, Pratical Quantum Mechanics, Springer-Verlag, 1971.

STUDIES ON ZEOLITE CONTRIBUTION TO THE SUN PROTECTION PROPERTIES OF PLANT OIL LOTION RICH IN VITAMIN E

S. Rendevski[1], N. Mahmudi[2], Krsto Blazev[3], R. Popeski-Dimovski[4] and F. Ajredini[2]

*[1]Faculty of Electrical Engineering, University "Goce Delcev",
Krste Misirkov, b.b., 2000 Stip, Republic of Macedonia*

*[2] Faculty of Natural Sciences and Mathematics, State University of Tetovo,
bul. Ilinden, b.b., 1200 Tetovo, Republic of Macedonia*

*[3]Faculty of Natural and Technical Sciences, University "Goce Delcev",
Krste Misirkov, b.b., 2000 Stip, Republic of Macedonia*

*[4]Faculty of Natural Sciences and Mathematics, University "Ss. Cyril and Methodius",
Gazi Baba, b.b., 1000 Skopje, Republic of Macedonia*

Abstract. Sunscreen lotions rich in vitamin E provide benefit in preventing and treating sunburns. The sun protection capacity of vitamin E`s lotion formulations decrease with time of light exposure. The zeolite microparticles with previously absorbed vitamin E and added after to sun protection oil lotion could be used as reservoir for replacing UV photodegraded vitamin E. In the research, the vitamin E absorption capacities of zeolite microparticles of concentration of 0.2 % w/v in plant oil mixture (Olea Europea Oil, Sunflower oil) have been studied by UV-Vis spectrophotometry. The sedimentation and laser diffraction measurements gave broad distribution on size of the zeolite microparticles (1 µm to 15 µm) without interparticle interactions in the solution. The results showed ten-fold decrease in UV absorbance at wavelength of 292 nm in the first 30 minutes of vitamin E absorption to zeolite microparticles and a flat of release in the sunscreen lotion.

PACS: 82.75.-z, 78.40.-q, 47.57.ef, 87.14.Pq

1. INTRODUCTION

The sun emits ultraviolet (UV) radiation in the wavelength range of 200 – 400 nm. The most of the harmful UV-C (200–280 nm) and the most of UV-B (280–320 nm) radiation is absorbed in the stratospheric ozone layer. The UV-A (320 – 400 nm) radiation is not affected by the stratospheric ozone layer. In the last few decades it has been found that the stratospheric ozone layer is depleted and the amount of harmful short wave UV radiation reaching the earth's surface is increasing [1]. Besides, people are exposed to UV radiation by outdoor activities and by the use of artificial sun tanning equipment that increases the risks of harmful UV effects, such as photoaging, sunburn, immune suppression and skin cancer induction [2]. When the UV-A radiation penetrates into the skin it provokes several damages such as immediate and delayed

tanning reactions, loss of collagen, decrease of the quantity of blood vessels, skin photosensitization, and alteration of the connective tissue in the dermis. The main absorbers of UV-A radiation in the skin are hemoglobin and melanin. The UV-B region is responsible for the skin tanning and direct damage to the skin, which results mainly in sunburn [2]. Most significantly, UV-B radiation results in direct damage of DNA by formation of free radicals in skin cells.

Sunscreen formulations use has been promoted as a way to prevent the harmful consequences of skin exposure to UV. Sunscreen formulations mainly protect against sunburn (expressed through the sun protection factor, SPF). However, in recent decades several pathways are founded to protect immune suppression, free radicals reduction and other biological consequences of UV radiation through incorporating proper ingredients and skin delivery mechanism [3]. The protective effects of sunscreen formulations depend on the way it is applied. Reapplication to the skin increases the protective effect, especially during swimming or sweating. Also, SPF and the thickness define the protection [3]. Most sunscreens may contain: a) organic chemical substance (chemical blockers) with UV light absorbing capability (such as oxybenzone, octyl-methoxy-cinnamate, avobenzone, alpha-tocopherol); b) opaque nanoparticles (physical blockers) that reflects light (such as titanium dioxide, zinc oxide); c) herbal spices (aloe, green tee); d) and combination of them [4]. Today, a various sunscreen formulations are available at the market: lotions, creams, emulsions, dispersions, gels, milks, sprays, tonics and others.

Photodegradation of sun protection molecules under exposure to outdoor UV radiation generates submolecules (of which some are free radicals) that are harmful for the skin. Reduction of photo degradation of active sun protective molecules (such as alpha-tocopherol) is possible through several techniques: a) substances that absorb UV radiation at specific wavelength; b) combining different sun protective molecules in same sunscreen formulation in order to achieve synergistic effect; c) complexing, encapsulating or entrapping of sun protective molecules that protect the molecules from UV radiation during the process of their release from the carrier materials such as gels, hydrogels, polymer dispersions and nano or micro porous particles (such as zeolites). The following properties of the ideal sunscreen formulation should be manifested [4]: light absorption in the range 280 – 320 nm; stability to heat, light degradation and perspiration; non-irritant and nontoxic characteristics; slow skin absorption; solubility and incorporation capability in carrier vehicles.

Alpha-tocopherol (vitamin E) is very effective against UV-B free radical damage [5]. It has a synergistic effect when combined in sunscreens with ascorbic acid (vitamin C). Vitamin E absorbs strongly in the UV-B region of 280-320 nm. Therefore it can act as a photoprotective sunscreen in skin cell membranes. Alpha-tocopherol and its acetate derivative have been shown to act as UV sunscreen photoprotectants by a scavenging mechanism of free radicals reduction [5]. Skin cells are photosensitive to damage due to generation of radical oxygen molecules. These include singlet oxygen $(^1O_2)^*$, free radicals such as superoxide anion radical O_2^{*-}, perhydroxyl radical HO_2^*, protonated form of O_2^*, and hydroxyl radical $^*OH$, that destroy the structural integrity of cellular lipid membranes. Vitamin E acts in two ways: as a physical

quencher of oxygen free radicals and as a chemical scavenger of photogenerated radicals. One molecule of a-tocopherol is able in average to deactivate up to 100 molecules of $^1O_2$ before itself being photodegraded. In addition, it has been shown that a-tocopherol could itself be converted in its radical form, a-chromanoxyl radical, by absorbing UV-B radiation. Vitamin E acts well together with other antioxidant (Vitamin C) because, in the absence of other antioxidant, it is depleted rapidly [6]. Recently, this conflict between the radical scavenging role of a-tocopherol as skin cells protector and the endogenous influence of its photodegraded radical form needs to be further investigated and resolved.

Another sunscreen formulation ingredient, as a part of this research, was octyl-methoxy-cinnamate (OMC). OMC is widely used as UV-B sunscreen protection substance. OMC photoisomerization processes take place under UV exposure [5]. When exposed to sunlight, this UV-B filter substance changes from octyl-p-methoxy-trans-cinnamate (E-OMC) to octyl-p-methoxy-cis-cinnamate (Z-OMC) with change in only 1 nm shift of the maximum UV absorption wavelength of n-hexane solution. The studies on OMC photostability show that no other degradation products, such as free radical submolecules, were detected when OMC was exposed to sunlight.

Entrapping of Vitamin E and OMC in some nano or microporous carrier particles could preserve defined amount of the sun protection molecules from photodegradation. After deterioration of the amount of the sun protective molecules under UV radiation exposure, a required quantity of in carrier preserved molecules could be released on defined pathways (for example, diffusion, pressure, heating) and thus replacing the deteriorated molecules to desired concentration for effective sun protection. One carrier material that can serve in that way is natural zeolite in its clinoptilolite mineral form.
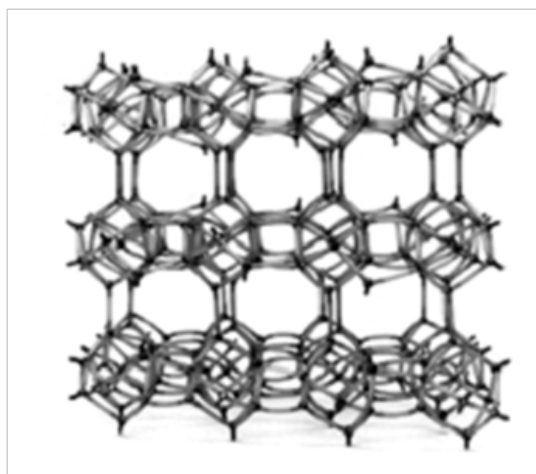
Fig 1.: Zeolite framework structure.

The aim of this research is to investigate the loading capacity of vitamin E and OMC as sun protection molecules to zeolite's microparticles. Natural zeolite can slowly or cannot adsorb molecules at all depending on the size of the openings (pores), thus functioning as molecular sieves. The electrical charge and polarity of the adsorbed molecules defines the adsorption ability of zeolites [6]. Clinoptilolite is a member of the natural zeolites. Clinoptilolite has

distinctive framework topology and Si/Al ratio less than 4. Its approximate chemical composition may be expressed as follows: $(K_2, Na_2, Ca)_3[(Al_6Si_{30}) O_{72}].24 \cdot H_2O$.

Three independent components are present in the clinoptilolite structure: the aluminosilicate framework, zeolite water and exchangeable cations. This clinoptilolite mineral contains three channels embraced by tetrahedral rings (Fig.1). The quantity of zeolite water depends on the distribution and type of cations, because cations in the channels and cavities are surrounded by both water molecules and oxygen atoms. Cations are bound to the zeolite structure more strongly by water oxygen than by oxygen atoms in the zeolite framework [6]. Water molecules present in the zeolite occupies the internal voids. Access of outer molecules to the zeolites voids and cavities occurs through rings composed of Al/Si and O atoms. The size of the pore (window) for zeolites with smaller rings that contain six Al/Si sites or less is 0.2 nm, and for larger rings the size is 0.8 - 0.85 nm. The internal structure of zeolites consists of interconnected cages or channels through the whole volume, which can have dimensionalities of one to three. The total pore volume usually is in the range of 0.10 to 0. 35 $cm^{3/}/g$.

2. EXPERIMENTS

Natural zeolite in its clinoptilolite mineral form was purchased from Bulgaria. Before use the zeolite powder was subjected for 6 hours at temperature of 100 ^0C in an oven under pressure of $1 \cdot 10^4$ Pa in order to evaporate the zeolite water. The laser diffraction measurement (Laser Fraunhofer, Germany) gave broad distribution on zeolite particles size in the range from 1 µm to 15 µm. The average pore size of 0.85 nm of the zeolite particles was determined by water diffusion method and relative total pore volume of 30 % has been calculated. The density of the particles of 2.30 g/cm^3 was determined by the gravimetrical method. In order to investigate possible interactions, conglomeration or aggregation of zeolite particles Sunprotection oil (SPO) in solution, sedimentation experiments were conducted on the tensiometer model DACT 31, DataPhysics, Germany. UV-Vis spectrophotometry experiments were conducted on Ultrospec 5300 pro UV/Visible Spectrophotometer, GE, USA. The sedimentation experiments, UV-Vis spectroscopy studies and preparation of the investigated solutions were conducted at room temperature. Sunprotection oil used in the research was a commercial grade product consisted of the following ingredients: parafinum liquidum, olea europea oil, sunflower oil, ethylmethoxy-cynnamate, alpha-tocopherol, Perfume.

3. RESULT AND DISCUSSION

Sedimentation experiments were conducted with a cone holder immersed in a glass cup full of 20 cm^2 of 0.2 % w/v zeolite in 0.2 v/v SPO in n-hexane at 20 ^0C and the tension force on the cone attached to the measurement unit of the tensiometer was measured in period of 2500 s. As the sedimentation of zeolite particles occurs, the cone holder becomes more filled and tension force of the cone increased with time. The sedimentation rate was determined and the results are shown on fig.2. The results show linear decrease of the sedimentation rate that is an

indication for no interparticle interaction in n-hexane, conglomeration or other aggregation processes of zeolite particles in SPO.

The investigation of the adsorption capacity of zeolite particles to SPO and thus to Vitamin E (alpha-tocopherol) and OMC as sunscreen active molecules were conducted on solution of 0.2 % v/v SPO in n-hexane with 0.2 % w/v zeolite powder (clinoptilolite form). UV-Vis spectrophotometer model Varian 2000 has been used with quartz glass cells. UV-Vis scans in the wavelength range 280 – 900 nm with resolution of 1 nm have been made on the investigated solution. As a reference substance, n-hexane has been used. Before subjecting the investigated solution to UV-Vis spectrophotometry, the solution of 0.2 % v/v SPO in n-hexane with 0.2 % w/v zeolite powder was slowly steered for 2 hours.
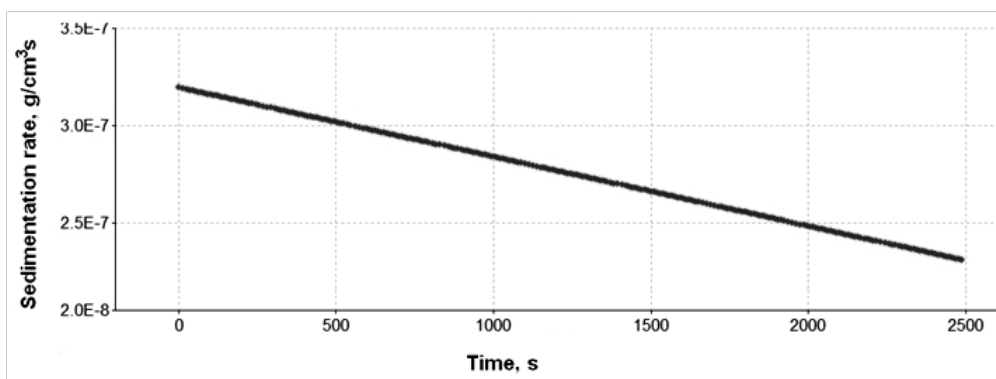

Fig.2: Sedimentation rate of 0.2 % w/v zeolite in 0.2 % SPO in n-hexane
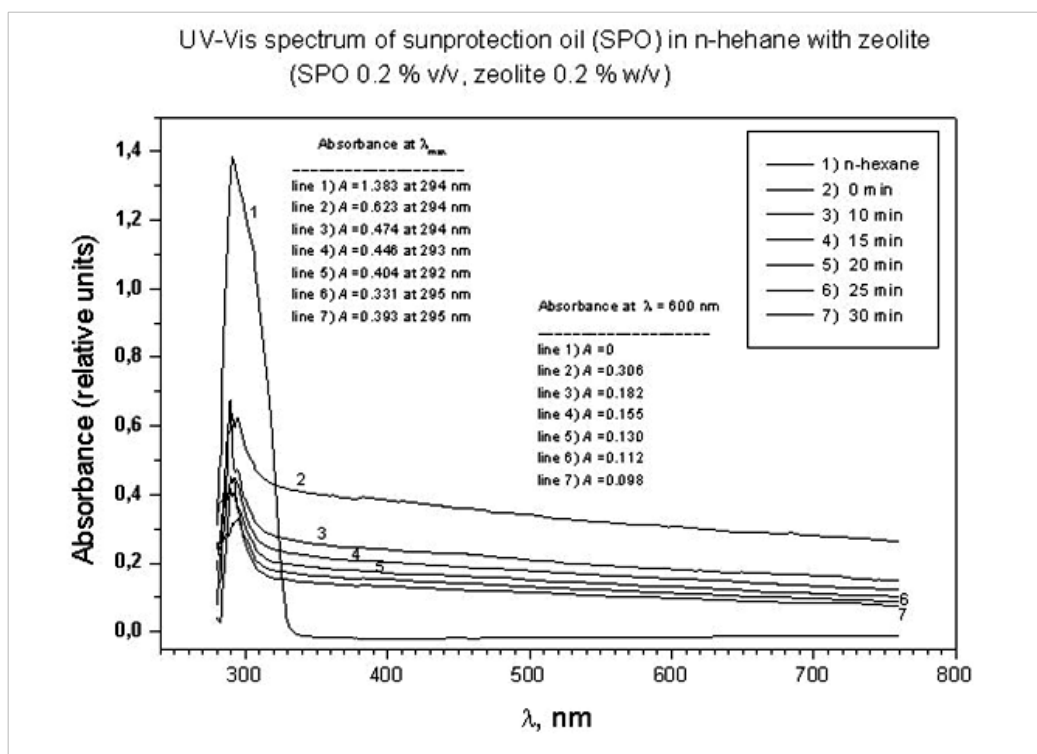

Fig.3: UV-Vis spectra of SPO in hexane with zeolite powder.

. UV-Vis scans have been made on every 5 minutes up to 30 minutes after placing the solution in the spectrophotometer. Decrease of the absorbance *A* of the SPO at the wavelength of maximum absorption ($\approx$ 292 nm) has been detected over time (fig.3). That was an indication that zeolite particles are adsorbing active molecules from the SPO (Vitamin E and OMC) that have maximum absorption in the same wavelength region [7].

The maximum SPO loading capacity of the zeolite powder has been determined after providing some preconditions. Namely, solution of 0.2 % v/v SPO in n-hexane with 0.2 % w/v zeolite powder (clinoptilolite form) wase constantly steered during three days. After 24 hours, 48 hours and 72 hours from the beginning, solution samples were put into the spectrophotometer and V-Vis spectra were obtained (fig.4). It is noticeable from fig. 4 that after two days of adsorption there is no difference between the UV-Vis spectra for the second and the third day.
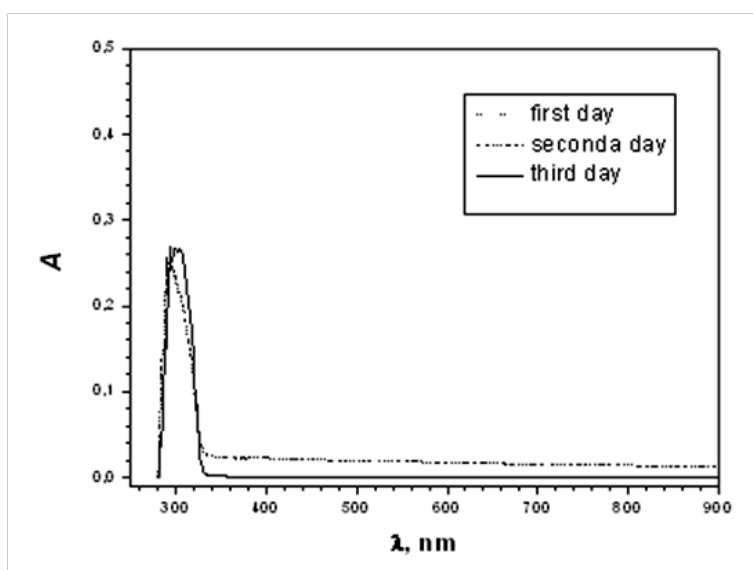

Fig 4.: UV-Vis spectra of SPO with zeolite powder after one, two and three days of steering.

The maximum absorbance at 292 nm is around 0.25 which is three times smaller than at the beginning (line 2, fig.3). This is evidence that zeolite powder can adsorb Vitamin E and OMC as sunprotection molecules and thus can serve as a reservoir for replacing photodegraded molecules during outdoor light exposure.

4. CONCLUSIONS

The research on the time dependence of the UV-Vis spectra of 0.2 % v/v SPO in n-hexane with 0.2 % w/v zeolite powder after preparation of the investigated solution showed that clinoptilolite, a natural form of zeolite, has a capacity for adsorption of Vitamin E and octyl-methoxy-cinnamate as active sunprotection molecules. Sedimentation studies showed that there is no interparticle interaction and aggregation of zeolite particles in non-polar solution that could lead to particles sticking and thus lowering the adsorption capacity.

REFERENCES

[1] Madronich, S., McKenzie, R.L., Björn, L.O., Caldwell, M.M. *J. Photochem. Photobiol*. B, **46**,5–19 (1998)

[2] Gil, E.M., Kim, T.H. *J. Photodermatol. Photoimmunol. Photomed*., **16**, 101–110 (2000)

[3] Wulf, H.C., Stender, I.M., Lock-Anderson, J. *J. Photodermatol. Photoimmunol. Photomed.* **13**, 129–132 (1997)

[4] Jain, S.K. and Jain, N.K. *International Journal of Cosmetic Science*, **32**, 89–98 (2010)

[5] Fryer, M., *Photochemistry and Photobiology*, **58**(2), 304-312 (1993)

[6] Payra, P. and Prabir, K.D. Handbook of Zeolite Science and Technology, Marcel Dekker, New York (2003)

[7] Damiani, E., Rosati, L., Castagna, R., Carloni, P., Greci, L. *J Photochem Photobiol B*. **82**(3), 204-213 (2006).

GRAIN REFINEMENT THROUGH SEVERE PLASTIC DEFORMATION (SPD) PROCESSING

N.Izairi[1] and A. Vevecka – Priftaj[2]

[1]*Department of Physics, Faculty of Natural Sciences and Mathematics, State University of Tetovo, Ilindenska nn, 1200 Tetovo, Republic of Macedonia*

[2] *Department of Physics, Polytechnic University of Tirana, , Sheshi "Nënë Tereza", N.4, Tirana, Albania*

Abstract. There is considerable current interest in processing metallic samples through procedures involving the imposition of severe plastic deformation (SPD). These procedures lead to very significant grain refinement to the submicrometer or even the nanometer level, resulting in advanced physical properties. Among various SPD processes, Equal Channel Angular Pressing, High pressure Torsion and Accumulated Roll Bonding have been widely used for many metals and alloys. In the present work, we present an overview of the most used methods of SPD for grain refinement and the production of bulk nanostructured materials with enhancement in their mechanical and functional properties. In order to examine the potential for using ECAP to refine the grain size and improve the mechanical properties, two commercial 5754 Al alloy and AA 3004 , were selected for study. Processing by ECAP gives a reduction in the grain size and an increase in the microhardness.

1. INTRODUCTION

Although the mechanical and physical properties of all crystalline materials are determined by several factors, the average grain size of the material generally plays a very significant and often a dominant role. Thus, the strength of all polycrystalline materials is related to the grain size, d, through the Hall-Petch equation which states that the yield stress σ_y, is given by

$$\sigma_y = \sigma_0 + k\, d^{-1/2} \tag{1}$$

where σ_0 is termed the friction stress and k is a constant of yielding. It follows from Eq. (1) that the strength increases with a reduction in the grain size and this has led to an ever-increasing interest in fabricating materials with extremely small grain sizes.

Nanostructured materials, in which the structural features (e.g., grains and/or domains separated by low-angle grain boundaries) are smaller than 100 nm in at least one dimension, have attracted worldwide research interest for more than a decade because of their unique properties. For example, the combination of high strength with high ductility has been reported

for some nanostructured metals and alloys: this is a rare, if not impossible, combination of mechanical properties for coarse-grained metals and alloys [1,2]. Among the many techniques available for producing nanostructured materials, severe plastic deformation (SPD) is the most popular and most rapidly developing one. SPD processing refers to various experimental procedures of metal forming that may be used to impose very high strains on materials leading to exceptional grain refinement. The unique feature of SPD processing is that high strain is impossed at relatively low temperatures (usually less than 0.4 T_m) without any significant change in the overall dimensions of the workpiece. Another feature is that the shape is retained due to the use of special tool geometries, which prevent free flow of the material and thereby produce a significant hydrostatic pressure. The presence of this hydrostatic pressure is essential for achieving high strains and introducing high densities of lattice defects that are necessary for exceptional grain refinement. SPD-produced nanomaterials are fully dense and their large geometric dimensions make them attractive for efficient practical applications. Fabrication of bulk nanostructured materials using severe plastic deformation is becoming one of the most actively developing areas in the field of nanomaterials, and SPD materials are viewed as structural and functional materials of the next generation of metals and alloys. Today, SPD techniques are emerging from the domain of laboratory-sale research into commercial production of various ultrafine-grained (UFG) materials [3].

The aim of this paper is to present an overview of the most used methods of severe plastic deformation for the production of bulk nanostructured materials with very significant enhancement in their mechanical and functional properties. Also, in order to examine the potential for using ECAP to refine the grain size and improve the mechanical properties, two commercial Al alloys, Al-5754 and AA 3004 were selected for study.

2. DIFFERENT SPD TECHNIQUES

Grain refinement is easily achieved by SPD through the introduction of large plastic deformations which induce the generation of severe crystal lattice rotations and simultaneously an extremely high number of dislocations rearranging into new low and high-angle grain boundaries [4-7] and deformation twins and twinned boundaries. This phenomenon known as the process of "crystal fragmentation" has created a world-wide interest and many investigations are now underway to determine the properties of materials processed by SPD [8-12]. There are several different types of SPD processes, but the three most common ones are equal-channel-angular Pressing (ECAP), high-pressure torsion (HPT) and accumulative roll-bonding (ARB). These three procedures are fundamentally different, but they each produce exceptional grain refinement to at least the submicrometer level.

2.1. Accumulative Roll-Bonding (ARB)

A technique which increases the available strain is **accumulative roll bonding(ARB)** (Fig. 1), in which the material is rolled, stacked and re-rolled, thus maintaining the sample thickness. Therefore, the achieved strain is unlimited in this process because repetition times are

endless in principle and have achieved ultra fine grains with less than 1μm. This technique has been applied to aluminium alloys [13] and steels [14] with total strains of up to 8, resulting in sub-micron grain sizes. Critical factors in successful accumulated roll bonding are surface preparation and cleaning, the deformation temperature, and the amount of strain. Depending upon the crystal structure, the microstructures have GS within the range of ~ 70-500 nm.
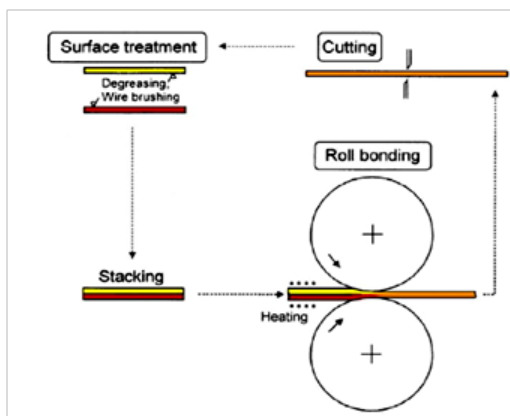

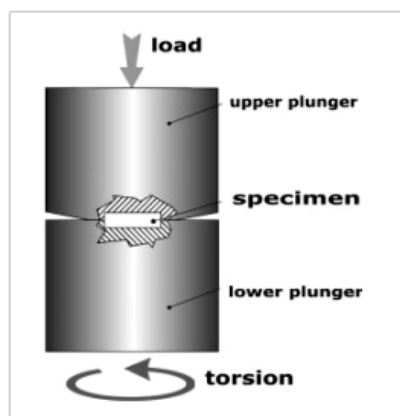**Fig. 1:** Schematic showing the accumulative roll bonding process.

Fig. 2: Schematic of HPT set-up

2.2. High Pressure Torsion (HPT)

The HPT method is shown schematically in Fig.2. Disc sample is torsionally deformed under high pressure of several GPa, many times between plungers, on which an outer pressure is applied. High friction forces between the rough dies and the ingot ensure deformation by *shear* during rotation of the plunger. Provided that the number of rotations is high enough, an almost homogenous nanostructure can be achieved. The main advantages of the HPT technique are that it gives high quality UFG materials with grain sizes < 100 nm and with this method can be processed brittle materials as intermetallics and semiconductors. But the main disadvantage is that the specimen dimensions are fairly small, with maximum discs diameter of 10-20 mm and up to 1mm in thickness; for this reason this method has limited industrial use [10].

2.3. Equal Channel Angular Pressing (ECAP)

Although several different SPD processing procedures are now available, the most promising technique appears to be equal-channel angular pressing (ECAP) where a bulk sample is pressed through a die constrained within a channel which is bent through an abrupt angle (Fig.3) [10]. Advantages of processing by ECAP include the retention of a constant cross-sectional area through the imposition of high strains and the ability to process samples without the introduction of either contamination or residual porosity. The strain imposed on the sample in each passage through the die is dependent primarily upon the angle, Φ, between the two parts of the channel (90∘ in Fig. 3) and also to a minor extent upon the angle of curvature, Ψ, representing the outer arc of curvature where the two channels intersect (0∘ in Fig. 3). The

amount of equivalent strain depends upon the two angles, φ and Ψ, and given through a relation, developed analytically, that depends on the geometry of the process. The ECAP experiments conducted to date, have generally used dies having φ =90∘ and Ψ =0∘. This corresponds to an equivalent strain of 1.1 in a single pass [10].

Furthermore, since the cross-sectional area remains constant, the samples may be rotated between consecutive passes through the ECAP die in order to activate different slip systems [5]. At the present time, processing by ECAP is conducted using either route A where the sample is not rotated between consecutive passes, route B_A where it is rotated by 90° in alternate directions between each pass, route B_C where it is rotated by 90° in the same direction between passes or route C where it is rotated by 180° between passes (Fig.5). The evidence available to date shows that, when using a die where the channel is bent through an abrupt internal angle of 90°, route B_C is the optimum processing route for achieving a homogeneous microstructure containing a large fraction of boundaries having high angles of misorientation [6].
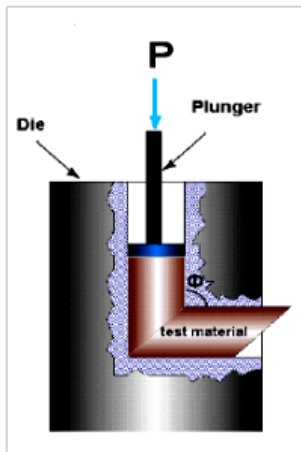

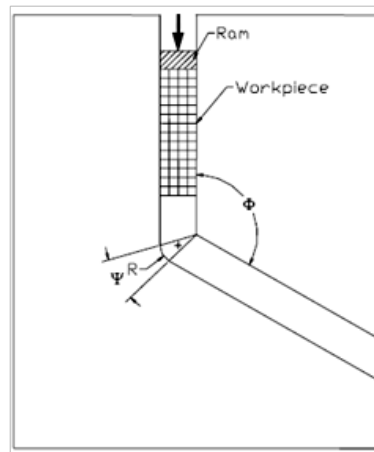**Fig. 3:** Schematic view of   ECAP die.

Fig. 4: A section through the ECAP die.

The application of this procedure is currently under investigation for many materials ranging from Al, Cu, Mg and Ni alloys to eutectic and eutectoid alloys and intermetallics.
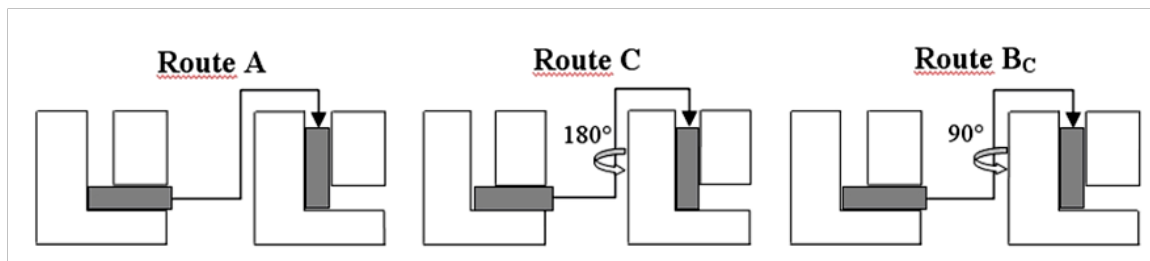

Fig. 5: Scheme of the processing routes in ECAP.

3. IMPROVEMENT OF MECHANICAL PROPERTIES OF COMMERCIAL AL ALLOYS PROCESSED BY ECAP

3.1 Experimental procedure

The experiments were conducted on two light-weight commercial aluminum Al- 5754 alloy having the following composition in wt%: 2.4-2.6% Mg, 0.1-0.6% Mn, 0.4% Cr, 0.4% Fe, 0.4% Si, 0.2% Zn with the balance as Al, and on Al -3004 alloy with a composition, in wt.%, of 1.1% Mg, 1,26 % Mn, 0.6% Fe, 0.4% Cu, and 0.4% Si. Observations by optical microscopy revealed a grain size of ~70 μm in the as received condition, for the Al-5754 alloy. The samples in the forms of cylinders with lengths of ~ 10 cm, were subjected to ECAP up to a total of 7 passes, equivalent to an imposed strain of ~ 7 for the Al-5754 alloy and up to 4 passes for AA 3004 . The pressings were performed at room temperature, using the route B_C.

Small pieces were cut from the as-pressed cylinders. Each of these pieces was polished and then used to measure the Vickers microhardness Hv, using a load of 100 g, applied for 15 s.

3.2 Experimental results and discussion

AA 5754: Microstructural examinations of samples pressed through 2 to 6 passes revealed an array of reasonably equiaxed grains having average sizes of < 1 μm. An example of the as pressed microstructure is shown in Fig.5, after 4 passes. Measurements indicated average grain sizes of ~ 0.3-0.4 μm, in the as-pressed condition, demonstrating that ECAP is an effective procedure for attaining an ultrafine grain size.
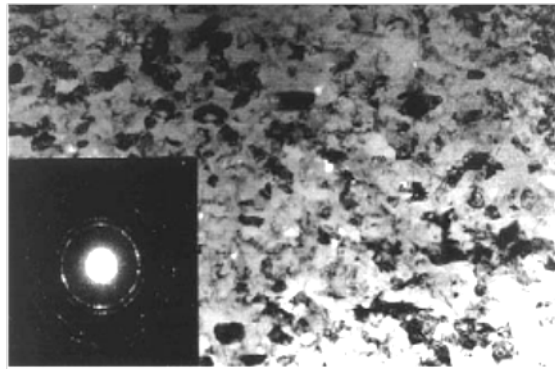
Fig. 6: Microstructure observed by transmission electron microscopy after ECAP through 4 passes.

Fig.7 shows the variation of the microhardness with the number of passes, where measurements were taken on 2 orthogonal planes and the first point (zero passes) refers to the unpressed alloy (Al-5754) .

Two conclusions may be reached from this plot. First, The hardness is essentially independent of the plane of sectioning. Second, the value of Hv increases abruptly after a single pass, but thereafter increases slowly with additional passes. Similar results are attained also for the AA 3004.
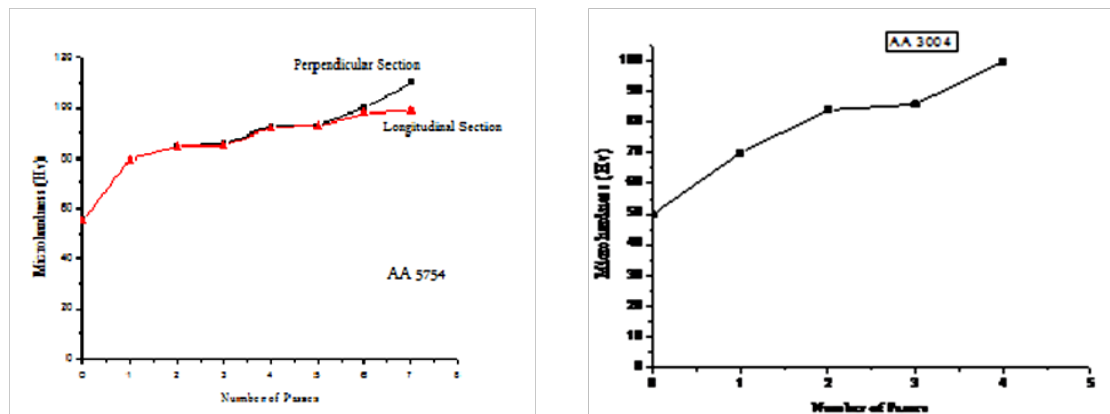
Fig. 7: Microhardness Hv versus number of passes in ECAP

4. CONCLUSIONS

This investigation demonstrates that ECAP was an effective tool for achieving a very substantial reduction in the grain size of the commercial 5754 Al alloy. In these experiments the initial GS of ~ 70 μm in the as received alloy, was reduced to ~ 0.3 - 0.4 μm by ECAP through up to 7 passes. The reduction in grain size gave an increase in the microhardness of the alloy. There was an immediate increase in the microhardness at a strain ~ 1 with minor additional increases with subsequent straining. Similar results were observed for the AA 3004.

REFERENCES

[1] Gleiter H. Acta Mater 2000; 48:1–30

[2] V.M. Segal. Mater. Sci. Eng. A, **197** (1995), p. 157

[3] R. .Z. Valiev, R.K. Islamgaliev and I.V. Alexandrov. Prog. Mater. Sci., **45** (2000), p. 103.

[4] Z. Horita, T. Fujinami, M. Nemoto and T.G. Langdon. Metall. Mater. Trans., **31A** p. 691 (2000)

[5] K. Ohishi, Z. Horita, M. Furukawa, M. Nemoto and T.G. Langdon. Metall. Mater. Trans., **29A**(1998), p. 2011.

[6] M. Furukawa, Y. Iwahashi, Z. Horita, M. Nemoto and T.G. Langdon. Mater. Sci. Eng. A, **257,** (1998), p. 328

[7] M. Furukawa, Z. Horita, M. Nemoto and T.G. Langdon. J. Mater. Sci., **36** (2001), p. 2835

[8] M. Cabibbo, Mater. Charact., 61, p.613 (2010)

[9] C.Xu, Z.Horita, T.G. Langdon, Acta Materialia 55, 203-212, (2007)

[10] R.Z. Valiev, T.G. Langdon, Progress in Materials Science 51, 881-981 (2006)

[11] M.J. Zehetbauer, H. P. Stüwe, A. Vorhauer, E. Schafler, J. Kohout, Adv.Eng.Mater. 5 (2003) , 330.

[12] R. Grössinger, R. Sato, D. Holzer, M. Dahlgren, Adv.Eng.Mater. 5 (2003) 285

[13] H.W.Hoeppel, J.May and M.Goeken, Adv.Eng.Mater. 6, p. 781-784, (2003).

[14] N.Tsuji, Y.Saito, H. Utsunomiya and S. Tanigawa, Scripta Materialia, Vol. 40, No. 7, pp. 795–800, 1999

GAMMA IRRADIATION INDUCED CHANGES IN THE BIOADHESION PROPERTIES OF CALCIUM ALGINATE GELS

R. Popeski-Dimovski[1], S. Rendevski[2] and N. Mahmudi[3]

[1]*Faculty of Natural Sciences and Mathematics, University "Ss. Cyril and Methodius", Gazi Baba, b.b., 1000 Skopje, Republic of Macedonia*

[2] *Faculty of Electrical Engineering, University "Goce Delcev", Krste Misirkov, b.b., 2000 Stip, Republic of Macedonia*

[2] *Faculty of Natural Sciences and Mathematics, State University of Tetovo, bul. Ilinden, b.b., 1200 Tetovo, Republic of Macedonia*

Abstract: The controlled release of substances and their administration to a specific substrate (tissue, epitel, etc.) often is facilitated with polymer gels that increase the bioadhesion force. One way for modification of the bioadhesion properties of polymer gels is through gamma irradiation. In this work, calcium alginate hydrogels were gamma irradiated with different absorbed doses (nonirradiated, 2.74 kGy, 5.47 kGy and 8.21 kGy or equivalent of 0h, 48h, 96h, and 144h of irradiation) for inducing changes of its bioadhesion properties. Mechanical compressibility tests (Zwick Z010 universal testing machine) and bioadhesion pull tests (DCAT tensiometer) were conducted on the irradiated hydrogels. We worked with three different types of sodium alginates from which hydrogels were prepared. $CaCO_3$ was used as a source of Ca^{2+} ions for crosslinking and GDL as an Ca^{2+} ions activation agent. The results showed that high absorbed doses of gamma irradiation reduced the structural integrity of the hydrogels (becoming softer) with small increase of the bioadhesion force.

PACS: 61.80.Ed, 82.35.Gh, 87.15.La, 87.85.J

1. INTRODUCTION

Alginates are natural occurring polysaccharides found in substantial amounts in brown seaweeds. They are unbranched binary co-polymers of (1–4)-linked residues of b-D-mannuronic acid (M) and a-L-guluronic acids (G). Alginic acid and its water-soluble sodium salt form have a great ability to give highly viscous solutions even at moderate concentrations. Aqueous solution of sodium alginate forms stable gels in the presence of multivalent cations such as Ca^{2+} and Mg^{2+}. Gel formation occurs due to the ionic interaction between guluronic acid residues from two or more alginate chains and cations, yielding a three-dimensional network of alginate molecules well described by the ''egg-box'' model [1]. Functional and physical properties, mechanical strength, porosity, gel uniformity, biocompatibility, and influence on encapsulated cells and other incorporated substances in the alginate gels vary widely depending on ratio of

mannuronic to guluronic acids, the frequency and size of guluronic acid blocks and the molecular weight of the polymer [2].

Currently Ca2+ is preferred to crosslink alginate for biomedical applications because of the mild reaction conditions compared for example to the cellular toxicity of both Ba2+ and Sr2+ [3,4]. Two methods of gelation have been extensively described and used to create alginate hydrogels: diffusion gelling and in-situ gelling. Diffusion gelling is an ideal approach that is widely used for rapidly encapsulating cells in microspheres of alginate used for controlled released methods where polymer gels swell in a medium in order to release a given substance. In this method calcium ions diffuse through the liquid alginate boundary, cross-linking alginate strands as the ions move through the volume of alginate. However, cross-links are not uniformly distributed throughout the gel [5,6].

On the other hand, in recent years there has been a very big interest in the preparation of homogeneous alginate gels in different forms by using in-situ gelling methods. In this method $CaCO_3$ is mixed with alginate to create a homogeneous mixture. D-Glucono-d-lactone (GDL) is added to acidify the solution and release calcium ions, making them available for cross-linking. The resultant hydrogel has an uniform distribution of cross-links [7].

Bioadhesion is the special case of adhesion in which the substrate is of biological origin (for example, skin or a mucous membrane). Bioadhesion is crucially important for pharmaceutical applications to design and develop biomaterials with optimal mucoadhesive properties. In the past few decades, several theories have been developed to describe the adhesion phenomena. Such theories include the electronic theory, [8] the adsorption theory, [9] the wetting theory, [10] and the diffusion theory [11].

2.MATERIALS AND METHODS

Sodium alginate samples were obtained from FCM Biopolymers Company, Norway and used as received. The initial molecular weights of NaAlgs (number-averaged M_n and weight-averaged M_w), guluronic to mannuronic ratio G/M are given in Table 1. Calcium carbonate and D-glucono-δ-lactone (GDL) were obtained from Aldrich. The polymer samples were placed in tightly closed containers, and irradiated for given time (48h, 96h, 144h or equivalent dose of, 2.74 kGy, 5.47 kGy and 8.21 kGy) in a Gammacell 220 type 60 Co-gamma irradiator at room temperature in air.

Table 1.

Alginate type	$\overline{M}_n$, g/mol	$\overline{M}_w$, g/mol	G/M
LF120M	340 x 10^3	670 x 10^3	70/30
LF200M	310 x 10^3	690 x 10^3	50/50
LF240D	275 x 10^3	500 x 10^3	45/55

2.1 Preparation of Alginate Gels

A $CaCO_3$-GDL system was used to activate controlled gellation. Calcium carbonate ($CaCO_3$) was used as a source of calcium ions to initiate gellation and GDL was used as a weak

acid for the activation of calcium ions from the carbonate. To achieve a neutral pH value, the molar ratio of $CaCO_3$ to GDL was maintained at 0.5. A molar ratio of calcium ion to GDL of 0.36 was used in order to secure preparation of an uniform gels from 1.5% sodium alginate solution as follows: 0.105g of sodium alginate was dissolved in 7 ml of deionized water and 0.0158 g $CaCO_3$ was put into the sodium alginate solution and the mixture was vortexed for 60 seconds. 0.056 g of GDL was dissolved in 0.02 mL of deionized water and added into alginate solution immediately and vortexed for 45 seconds and then put to rest. After 24 hours the gels are formed. Through the same method calcium alginate activated solutions were prepared from irradiated sodium alginates. In figure 1.1 and 1.2 we see a bulk prepared alginate gel and a 5 mm thick slice prepared for compressibility and bioadhesion tests [12]. Because of the fact that the compressibility and bioadhesion test are with destructive nature we noticed some small differences in values with slices from different bulk samples but the results are reproducible in a given range.

Fig. 1.1.   Fig. 1.2   Fig. 1.3.   Fig. 1.4.

2.2 Experimental setup for structural integrity tests

For compressibility tests we used Zwick Z010 with universal one axial mode of work. We use a 1kN cell and movement speed of 5 mm/min.
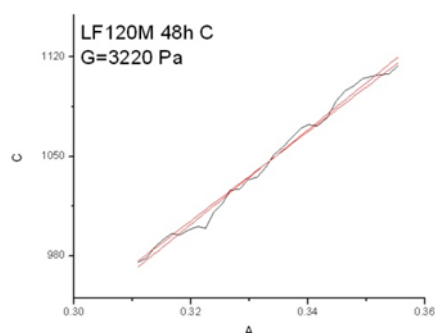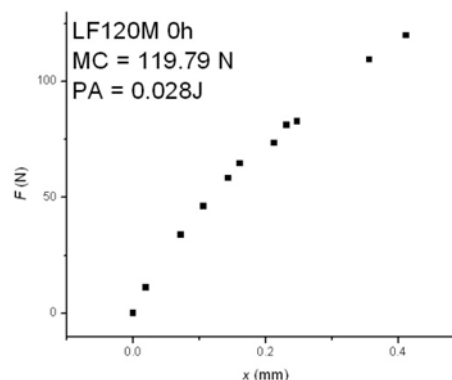

Fig. 1.5.   Fig. 1.6.

The instrument is show in figure 1.3.The results further shown are an average of four measurements for every type of sample. On figure 1.5 we give a graphical example of the compressibility tests and on figure 1.6 we give a graphical example of the bioadhesion tests.

2.3 Experimental setup for bioadhesion

For the bioadhesion measurements we used DCAT 11 from DataPhysics, Germany. This instrument has a movable lover part and a fixed upper end that is connected to the measurement sensor. We use two-composite instant glue to attach the gel on the lower side with the movable part. To the sensor we attach a flat surface holder where we place poly(ethyleneterephthalate) foil as the contact surface that mimics mucosa layer. The whole system is presented on figure 1.4. Contact between the gel and the surface is detected as a load change of 8 mg on the sensor. Then the gel is pushed up to exert a force equivalent to 5g on the gel. We measure two parameters of bioadhsesion. Force at detachment (FD) and work of adhesion (WA).

3. RESULTS AND DISCUSSIONS

We do bioadhseion and compressibility tests for all types of alginates for nonirradiated and irradiated samples. In table 3.1, 3.2,and 3.3 we give the results for the elastic modulus of the alginate gels from the compressibility tests made for LF120M, LF200M and LF240D alginate. In table 3.4, 3.5, and 3.6 we give the results from the biadhesion pull tests for alginate gels made from LF120M, LF200M, LF240D alginate.

Table 3.1: Mechanical tests for alginate LF120M

Dose (kGy)	0	2.74	5.47	8.21
G (N/m^2)	3491	2647	2735	2312

Table 3.2: Mechanical tests for alginate LF200M

Dose (kGy)	0	2.74	5.47	8.21
G (N/m^2)	3223	2810	2971	2333

Table 3.3: Mechanical tests for alginate LF240D

Dose	0	2.5 kGy
G (N/m^2)	2320	2069

Table 3.4: Bioadhesion tests for alginate LF120M

Dose (kGy)	Force of detachment (N)	Work of adhesion (J)
0	119,79	0,028
2.74	73,28	0,036
5.47	71,80	0,045
8.21	115,84	0,049

Table 3.5: Bioadhesion tests for alginate LF200M

Dose (kGy)	Force of detachment (N)	Work of adhesion (J)
0	108,74	0,031
2.74	99,34	0,039
5.47	100,27	0,031
8.21	109,52	0,049

Table 3.6: Bioadhesion tests for alginate LF240D

Dose (kGy)	Force of detachment (N)	Work of adhesion (J)
0	110,95	0,103
2.74	83,72	0,068
5.47	106,56	0,098
8.21	87,14	0,078

The results presented in the above tables 3.1, 3.2 and 3.3 show that by the increase of the absorbed dose of gamma irradiation the elastic modulus decrease. That indicated mechanical weakness of the gels influenced by the irradiation scission effect of the polymer chains in the gel network. The results of the bioadhesion tests (tables 3.4, 3.5 and 3.6) show changes of the force of detachment and the work of adhesion, mainly at 2.74 kGy and 5.47 kGy. This findings show that gamma irradiation of the alginate gels can yield more soft gels with decreased bioadhesion in comparison to the nonirradiated gels. In other words, applying gamma irradiation at desired doses to alginate gels can produce changes in mechanical and bioadhesion properties that can be of interests for some specific application of the gels.

4. CONCUSION

With this work we show that gamma irradiation of the calcium alginate gels has an influence on their   bioadhesion and mechanical properties, especially at some medium doses. We conclude that gamma irradiation on calcium alginate gels at specific doses can produce gels with changed properties – strong bioadhesive gels can become less bioadhesive and more elastic. That can be of interest for applications where bioadhesion need to be less pronounced. Furthermore, we see that alginate that has lower rigidity or has a lower G/M ratio has a higher work of adhesion, because of its week gel structure funded on less specific ionic interactions between the Ca^{2+} ions and the ionic groups in the alginate polymer.

REFERENCES

[1] Grant, G.T., Morris, E.R., Rees, D.A ., Smith, P.J.C., Thom, D., 1973. Biological interactions between polysaccharides and divalent cations: the egg-box model. FEBS Lett. 32, 195–198.

[2] Smidsrod, O., 1974. Molecular basis for some physical properties of alginates in gel state. J. Chem. Soc. Faraday Trans. 57, 263–274.

[3] Klock, G., Frank, H., Houben, R., Zekorn, T., Horcher, A ., Siebers, U., Wohrle, M., Federlin, K., Zimmermann, U., 1994. Production of purified alginates suitable for use in immunoisolated transplantation. Appl. Microbiol. Biotechnol. 40, 638–6 43.

[4] K. I. Draget, G. SkjakBraek, O. Smidsrod, Alginate ba-sed new materials, Int. J Biol Macromol., 21 (1997) 47.

[5] Stojan J. Rendevski, Influence of microgel particles of sodium alginate on gel structure of calcium alginate gels used for controlled release of active substances, Doctoral dissertation, Skopje, 2004.

[6] RENDEVSKI, S., POPESKI-DIMOVSKI, R. "A new method for measuring swelling kinetics of polymer gels, AIP Conference Proceedings, 899, 775 (2007).

[7] C. K. Kuo, P. X. Ma, Ionically crosslinked alginate hydrogels as scaffolds for tissue engineering: Part 1. Structure, gelation rate and mechanical properties, Biomaterials, 22 (2001) 511.

[8] B. V. Derjaguin, Y. P. Toporov, V. M. Mueler, I N. Aleinikova, On the relationship between the elec-trostatic and the molecular component of the adhesion of elastic particles to a solid surface, J Colloid Interface Sci., 58 (1977) 528.7.

[9] A. J. Kinlcoh, Review, The science of adhesion, J.Mater Sci., 15 (1980) 2141.

[10] D. H. Kaelbe, J. Moacanin, A surface energy analysis of bioadhesion, Polymer, 18 (1977) 475.

[11] S. S. Voyutskii, Autohesion and Adhesion of High Polymers, Interscience, New York (1963)

[12] Riste P.Dimovski, γ radiation induced changes in the bioadhesion properties of Ca-alginate gels, Master thesis, Skopje, 2009

ENUMERATION OF CODES OVER THE RING $F_q + uF_q$

E. Saltürk[1] and İ. Şiap[2]

*1-2Yildiz Technical University, Davutpasa Campus, Mathematics Department,
34210, İstanbul, Turkey*

Abstract. We count the codes over $F_q + uF_q$ by their generator matrices where $u^2 = 0$ and q is a prime power. We prove a theorem that gives a direct formula for counting the distinct (not necessarily inequivalent) linear codes over this ring. As a result of this theorem, we define Generalized Gaussian Numbers and state some of their properties. Finally, we present some number sequences which are new to our best knowledge.

PACS: 02.10.Hh, 02.10.De

1. INTRODUCTION

The number of the subcodes of a linear code is one of the most important problems of the combinatorial coding theory. This problem was completely solved for the codes over finite fields and presented by Gaussian coefficients [8]. Formula which gives the number of subgroups of type μ of a given finite p – group of type one were given by Delsarte [3], Djubjuk [4] and Yeh [16] in 1948. Calugareanu [2] found a formula which gives the total number of subgroups of an abelian finite group whose p – ranks do not exceed two.

The number of linear quaternary codes has been obtained recently [13]. Further, some interesting number sequences which follow from so called Type I Generalized Gaussian Numbers are also presented [13]. Here, we study the number of linear codes over the ring $F_q + uF_q$ ($u^2 = 0$): This ring has been of great interest to many researchers [1, 7, 10, 11, 15] and also found many applications. Our method for counting the linear codes is based on the construction of the generator matrices of the codes over $F_q + uF_q$. We choose ordered linearly independent elements for the generator matrices. Moreover, we present some new integer sequences which follow as an application of the number of linear codes over $F_q + uF_q$. This family of numbers is called Generalized Gaussian Numbers such as called in [14] due to resemble to the original Gaussian Numbers. Finally, we present some formulas and some new sequences.

Let F_q be a finite field with q elements where q is a prime power. A linear code C of length n over F_q is a subspace of F_q^n.

A linear code over F_q is equivalent to a F_q – code with generator matrix: $(I_k \ A)$.

Definition 1. [8] For a positive integer $q \neq 1$ and all nonnegative integers k, the q – ary Gaussian coefficient $|G_q(n,k)|$ ($n \in \mathbb{N}$) are defined by

$$\begin{bmatrix} n \\ 0 \end{bmatrix}_q = 1 \quad \text{and} \quad \begin{bmatrix} n \\ 0 \end{bmatrix}_q = \frac{(q^n - 1)(q^{n-1} - 1)\dots(q^{n-k+1} - 1)}{(q^k - 1)(q^{k-1} - 1)\dots(q - 1)}, \quad k = 1, 2, \dots$$

Theorem 2. [8] The number of distinct (although not necessarily inequivalent) $[n, k]$ – codes over F_q is the q – ary Gaussian coefficient $\left| G_q(n, k) \right|$.

For the proof of this theorem and some more details the reader is friendly directed to [8]. Let $R_q = F_q + uF_q$ where q is a prime power and $u^2 = 0$ denote a finite ring of q^2 elements.

Definition 1. An R submodule C of R^n is called an R – linear code, the elements of C are called codewords.

Theorem 3. [10] A linear code C over R_q is permutation equivalent to a code with generator matrix of the form

$$\begin{pmatrix} I_{k_1} & A_{11} & A_{12} \\ 0 & uI_{k_2} & uA_{22} \end{pmatrix} \tag{1}$$

where A_{ij}'s denote matrices whose entries are from R_q and I_{k_1}, I_{k_2} are identity matrices of sizes k_1, k_2 respectively. The number of elements of C is equal to $q^{2k_1 + k_2}$. A linear code C generated by the matrix (1) is called a (k_1, k_2) – type code.

2. CODES OVER $F_q + uF_q$

In this main section, we present a direct formula which gives the number of all distinct codes over R_q which is the main goal of this paper. The ring $F_q + uF_q = F_q[u]/(u^2)$ where $u^2 = 0$ has q^2 elements in total and has both units and non-units. The non-units are multiple of u and units are not. There are $(q-1)q$ units and $q-1$ non-units. If an element of $R_q \setminus \{0\}$ is a unit we say that its order is q^2 (generates the all ring as an ideal) otherwise q.

An element of the ring R_q^n is said to be free if at least one of its entries is a unit otherwise it is called non-free. Hence, free elements of R_q^n are of order q^2 and non-free elements are of order q. Zero vector is of order 1 and it is neither unit nor non-unit.

Now, we state and prove the main theorem:

Theorem 4. The number of distinct (not necessarily inequivalent) $[n, (k_1, k_2)]$ – codes over R_q is

$$N_{k_1,k_2}^{R_q} = \frac{\displaystyle\prod_{t=1}^{2}\prod_{i=0}^{k_t-1}\left(\left(q^{3-t}\right)^n - \left(q^{2-t}\right)^n q^{\sum_{j=0}^{t-1} k_j} q^i \right)}{\displaystyle\prod_{s=1}^{2}\prod_{r=0}^{k_s-1}\left(\prod_{p=1}^{s}\left(q^{3-s}\right)^{k_p} \prod_{j=s+1}^{2}\left(q^{3-j}\right)^{k_j} - \left(\prod_{p=1}^{s}\left(q^{2-s}\right)^{k_p}\right)\left(q^{1-s}\right)^{k_{s+1}} \prod_{t=s+2}^{2}\left(q^{3-t}\right)^{k_t} q^r \right)} \tag{2}$$

Proof. In order to find linear codes of length n and type (k_1, k_2) over R_q, we construct their generator matrices. First, we choose k_1 linearly independent elements of order q^2 and k_2

linearly independent elements of order q from R_q^n and then we construct a generating set whose elements are linearly independent of type (k_1, k_2).

We choose the first element of order q^2 in $q^{2n} - q^n$ different ways since q^n gives the elements whose order is not q^2. The second element is chosen in $q^{2n} - q^n.q$ different ways. By continuing in the same way, we choose k_1 linearly independent elements of order q^2 in

$$\left(q^{2n} - q^n\right)\left(q^{2n} - q^n.q\right)...\left(q^{2n} - q^n q^{k_1-1}\right) \tag{3}$$

different ways. We first choose k_2 linearly independent elements of order q. We do the first choice in $q^n - q^{k_1}$ different ways since q^{k_1} gives the number of elements whose order is less than q. Continuing in the same way, we obtain k_2 linearly independent elements of order q as

$$\left(q^n - q^{k_1}\right)\left(q^n - q^{k_1+1}\right)...\left(q^n - q^{k_1+k_2-1}\right) \tag{4}$$

By multiplying (3) and (4), the first part of the proof follows:

$$\left(q^{2n} - q^n\right)\left(q^{2n} - q^n.q\right)...\left(q^{2n} - q^n q^{k_1-1}\right)\left(q^n - q^{k_1}\right)\left(q^n - q^{k_1+1}\right)...\left(q^n - q^{k_1+k_2-1}\right) \tag{5}$$

Now, we construct a linearly independent generating set in a similar way we did in the first part of the proof. Here, the number of elements in which we do the choice is $q^{2k_1+k_2}$. Hence, similarly, we write the number of k_1 linearly independent elements of order q^2 and k_2 linearly independent elements of order q as

$$\left(q^{2k_1+k_2} - q^{k_1+k_2}\right)\left(q^{2k_1+k_2} - q^{k_1+k_2+1}\right)...\left(q^{2k_1+k_2} - q^{k_1+k_2+k_1-1}\right) \times$$
$$\left(q^{k_1+k_2} - q^{k_1}\right)\left(q^{k_1+k_2} - q^{k_1+1}\right)...\left(q^{k_1+k_2} - q^{k_1+k_2-1}\right). \tag{6}$$

We take (5) as the numerator and (6) as the denominator, and then the result gives the number.

Corollary 5. The number of distinct (although not necessarily inequivalent) $[n,(k_1,k_2)]$– codes over $R_2 = F_2 + uF_2$ is

$$N_{k_1,k_2}^{R_2} = \begin{bmatrix} n \\ k_1, k_2 \end{bmatrix} = \frac{\prod_{i=0}^{k_1-1}\left(4^n - 2^{n+i}\right)\prod_{j=0}^{k_2-1}\left(2^n - 2^{k_1+j}\right)}{\prod_{t=0}^{k_1-1}\left(4^{k_1}2^{k_2} - 2^{k_1+k_2+t}\right)\prod_{l=0}^{k_2-1}\left(2^{k_1}2^{k_2} - 2^{k_1+l}\right)}. \tag{7}$$

Corollary 6. The number of distinct (although not necessarily inequivalent) $[n,(k_1,k_2)]$– codes over $R_4 = F_4 + uF_4$ is

$$N_{k_1,k_2}^{R_4}(n) = \begin{bmatrix} n \\ k_1, k_2 \end{bmatrix}_{R_4} = \frac{\prod_{i=0}^{k_1-1}\left(16^n - 4^{n+i}\right)\prod_{j=0}^{k_2-1}\left(4^n - 4^{k_1+j}\right)}{\prod_{t=0}^{k_1-1}\left(16^{k_1}4^{k_2} - 4^{k_1+k_2+t}\right)\prod_{l=0}^{k_2-1}\left(4^{k_1}4^{k_2} - 4^{k_1+l}\right)}. \tag{8}$$

Note: If $k_1 = 0$ and q is a prime, then we obtain Gaussian coefficient $\begin{bmatrix} n \\ k_2 \end{bmatrix}_R$.

Example 7. We calculate the number of distinct $[2,(1,1)]$ – codes over $R_4^2 = F_4 + uF_4$.

From (8),

$$N_{1,1}^{R_4}(2) = \frac{(16^2 - 4^2)(4^2 - 4)}{(16.4 - 4.4)(4.4 - 4)} = 5 \tag{9}$$

distinct $[2,(1,1)]$ – codes over R_4.

Indeed, these codes are given by the following generator matrices:

$$\begin{bmatrix} 1 & 0 \\ 0 & u \end{bmatrix}, \begin{bmatrix} 1 & 1 \\ 0 & u \end{bmatrix}, \begin{bmatrix} 1 & w \\ 0 & u \end{bmatrix}, \begin{bmatrix} 1 & \hat{w} \\ 0 & u \end{bmatrix}, \begin{bmatrix} u & 0 \\ 0 & 1 \end{bmatrix}$$

where w and $\hat{w}$ are the elements of R_4.

3. APPLICATIONS

3.1. Properties of $N_{k_1,k_2}^{R_q}$

Similar to Gaussian coefficient, some properties for Generalized Gaussian Numbers (similar results are given for Generalized Gaussian Numbers in Theorem 6 of [14]) are presented in this section where $q = 4$.

Theorem 8. Let n be a positive integer. $R_4 = F_4 + uF_4$, $(k, k_1, k_2 \leq n)$. The numbers $N_{k_1,k_2}^{R_4}(n)$ satisfy the properties given in [14]:

1. $k_1 + k_2 \leq n$:

    i. $$\begin{bmatrix} n \\ k_1, k_2 \end{bmatrix}_{R_4} = \begin{bmatrix} n \\ n - (k_1 + k_2), k_2 \end{bmatrix}_{R_4},$$

    ii. Define $\begin{bmatrix} n \\ 0,0 \end{bmatrix}_{R_4} = 1$ then

    $$\begin{bmatrix} n \\ k_1, 0 \end{bmatrix}_{R_4} = \begin{bmatrix} n \\ n - k_1, 0 \end{bmatrix}_{R_4} \qquad \begin{bmatrix} n \\ 0, k_2 \end{bmatrix}_{R_4} = \begin{bmatrix} n \\ 0, n - k_2 \end{bmatrix}_{R_4}.$$

2. $k_1 + k_2 = n$, then $\begin{bmatrix} n \\ k_1, k_2 \end{bmatrix}_{R_4} = \begin{bmatrix} n \\ k_2, k_1 \end{bmatrix}_{R_4}.$

3. $\begin{bmatrix} n \\ 0, n \end{bmatrix}_{R_4} = \begin{bmatrix} n \\ n, 0 \end{bmatrix}_{R_4}.$

4. $k \leq n$, $k = 1, 2, \ldots, n$, then $\begin{bmatrix} n+1 \\ n - (k-1), k \end{bmatrix}_{R_4} = 2^k \begin{bmatrix} n \\ n - k, k \end{bmatrix}_{R_4} + \begin{bmatrix} n \\ n - (k-1), k-1 \end{bmatrix}_{R_4}.$

Proof. The proof follows by applying the definitions.

3.2. Some New and Existing Sequences

Here, we list the number of some linear codes over $R4$ which give us some number sequences. Some of these sequences are new which do not exist in the literature and some of them are existing sequences [12].

Table 1: The number of codes of given type and length

(k_1,k_2)	n	Number	(k_1,k_2)	n	Number	(k_1,k_2)	n	Number
(0,1)	1	1	(1,0)	1	1	(2,1)	3	21
	2	5		2	20		4	28560
	3	21		3	336		5	31164672
	4	85		4	5440		6	32411258880
	5	341		5	87296		7	
	6	1365		6	1397760		8	
	7	5461		7	22368256			
	8	21845		8	358158480			
(k_1,k_2)	n	Number	(k_1,k_2)	n	Number	(k_1,k_2)	n	Number
(1,1)	2	5	(1,2)	3	21	(2,2)	4	357
	3	420		4	7140		5	973896
	4	28560		5	1947792		6	8507955456
	5	1855040		6	59579520		7	
	6	119159040						

Table 2: Some new and existing sequences

$a_n^{0,1}$	Existing sequence (A002450)	$a_n^{1,2}$	New sequence
$a_n^{0,2}$	Existing sequence (A006105)	$a_n^{1,3}$	New sequence
$a_n^{0,3}$	Existing sequence (A006106)	$a_n^{2,0}$	New sequence
$a_n^{1,0}$	Existing sequence (A166984)	$a_n^{2,1}$	New sequence
$a_n^{1,1}$	New sequence	$a_n^{2,2}$	New sequence

These sequences are compared to Sloane's list [12]. Some of them exist and some are new. The sequences $\mathbf{a_n^{0,2}}$ (A006105) and $\mathbf{a_n^{0,3}}$ (A006106) given in Table 2 give the Gaussian coefficient $\left| G_{R_4}(n,2) \right|$ and $\left| G_{R_4}(n,3) \right|$, respectively.

4. CONCLUSION

In this paper, we have developed and proved a direct formula for the number of linear codes over the ring $F_q + uF_q$. We also obtained some new interesting number sequences. Further research on this topic would be studying the number of linear codes over different finite rings. Also, studying the properties of generalized Gaussian numbers is an interesting topic to be explored further.

REFERENCES

[1] T. Abualrub and I. Siap, pp. 520-529, Constacyclic codes over F2+uF2, Journal of The Franklin Institute, **346**, (2009)

[2] G. Calugareanu, pp. 157-167, The total number of subgroups of a finite Abelian group, Scientiae Mathematicae Japonicae **60**, No.1 (2004)

[3] S. Delsarte, pp. 600-609, Fonctions de Möbius sur les groupes abeliens finis, Annals of Math. **49**, (1948)

[4] P.E. Djubjuk, pp. 351-378, On the number of subgroups of a finite abelian group, Izv. Akad. Nauk SSSR Ser. Mat. **12**, (1948)

[5] T. Honold and I. Landjev, Linear codes over finite chain rings, The Electronic Journal of Combinatorics **7**, (2000)

[6] A. R. Hammons, P. V. Kumar, A. R. Calderbank, N. J. A. Sloane, P. Sole, The $\bar{z}$4-Linearity of Kerdock, Preparata, Goethals, and Related Codes, IEEE Transactions on Information Theory, **40**, (1994).

[7] S. Ling, P. Sole, pp. 983-997, Type II Codes Over F4 +uF4, European Journal of Combinatorics, 22, (2001)

[8] F.J. MacWilliams, N.J.A Sloane, The Theory Of Error Correcting Codes, North-Holland Pub. Co., (1977)

[9] B.R. McDonald, Finite Rings with Identity, Pure and Applied Mathematics, Marcel Dekker, (1974).

[10] M. Ozen and I. Siap, pp. 17-29, Linear codes over Fq[u]=(us) with respect to the Rosenbloom-Tsfasman metric, Designs Codes and Cryptography, 38, (2006)

[11] J.F. Qian, L.N. Zhang, S.X. Zhu, pp. 820-823, (1+u)-Constacyclic and cyclic codes over F2+uF2, Applied Mathematics Letters, 19, (2006)

[12] N. J. Sloane A, On-Line Encyclopaedia of Integer Sequences, Published electronically at http://www.research.att.com/njas/sequences.

[13] E. Salturk, I. Siap, pp. 250-259, Generalized Gaussian Numbers Related to Linear Codes over Galois Rings, European Journal of Pure and Applied Mathematics, 5, (2012)

[14] I. Siap, Linear Codes over F2+uF2 and Their Complete Weight Enumerators, OSU Dijen Conference, Codes and Designs, Ohio State Unv. Math. Res. Inst. Publ. 10, Walter de Gruyter, (2002)

[15] Y. Yeh, pp. 323 – 327, On prime power abelian groups. Bull. AMS, 54, (1948)